공학박사 학위논문

Reverse Osmosis Membrane with Nanocarbon Materials

나노카본 소재를 활용한 역삼투막

2020 년 2 월

서울대학교 대학원

기계항공공학부

李 昆 洲

Reverse Osmosis Membrane with Nanocarbon Materials

나노카본 소재를 활용한 역삼투막

지도교수 김 용 협

이 논문을 공학박사 학위논문으로 제출함

2020 년 1 월

서울대학교 대학원

기계항공공학부

이 곤 주

이곤주의 공학박사 학위논문을 인준함

2020 년 2 월

위 원 장 : 이 태 우

부위원장 : 김 용 협

위 원 : 이 홍 희

위 원 : 강 태 준

위 원 : 김 태 우

Abstract

Reverse Osmosis Membrane with Nanocarbon Materials

Kunzhou Li

Department of Mechanical and Aerospace Engineering

The Graduate School

Seoul National University

Freshwater is not only a necessary resource for human survival but also a pillar of the global economy. Reliable and sustainable supply of freshwater resources is essential for agriculture, industry, energy production and people's life. However, with population growth, economic development and climate change, the crisis of insufficient clean water resources has become a global problem. Improving the efficiency and effectiveness of water purification technology, to produce clean water and protect the environment in a sustainable manner, is the biggest and most serious challenge of this century.

In recent years, reverse osmosis (RO) has become a critical water treatment technology, which promises to greatly increase the supply of clean water through purification of nontraditional water sources. Although water flux and solute rejection by reverse osmosis membranes have continually improved over the past few decades,

reverse osmosis techniques are still relatively energy intensive, non-selective and prone to fouling. Therefore, more development and upgrades are needed in terms of increasing water permeability to save energy, improving membrane structure and stability to be more resistant to fouling. Modern reverse osmosis (RO) membranes have composite structures, where a thin polymeric film is formed over a relatively thick, porous support membrane. This support membrane not only provides suitable mechanical stability for the RO film under high applied pressure, but more importantly, has a crucial influence on the performance of the in situ synthesized thin polymeric film. In the thesis, the influences of support layer on improve the selectivity and water flux of polyamide (PA) selective layer by improving and optimizing the structure and surface chemistry of the support layer was investigated.

(1) It is well known that the support membrane's surface chemistry and pore size and porosity can influence the thickness, roughness, and cross-linked structure of the selective layer which formed by interfacial polymerization, thereby affecting the overall performance of the reverse osmosis membrane, including water flux, rejection and antifouling ability. A support layer with a large surface porosity can help to increase water flux but the salt rejection will decrease; a support layer with good hydrophilicity may result in a decrease in water flux.

In this work, by grafting a layer of graphene oxide on the surface of the support layer with large pores, the diffusion of MPD molecules in the aqueous phase in the

support layer pores into the organic phase solution are controlled during the interfacial polymerization process by physically blocking & improving the hydrophilicity of the surface of the support layer. Thereby, a smoother PA layer and a RO membrane with a higher water flux can be formed.

Moreover, a variety of sizes of graphene oxide are applied to the surface of the support layer, and we found that the size of the graphene directly affects the water flux of the support layer. The smaller the graphene oxide sheets, the larger the water flux of the support layer due to the smaller size graphene has more edge length at the same mass. The selection of the microfiltration membrane support layer with an appropriate pore size for the small size of graphene oxide will result in optimal salt rejection and water flux.

(2) Vertically aligned carbon nanotube (VACNT) wall membrane with its ultrafast water permeability shows a great promise as a novel support layer for membranes because of its ultrahigh porosity and hydrophobicity. We utilize the wall membrane as a support layer in forming a reverse osmosis (RO) membrane. For the purpose, a polyamide (PA) selective layer is grown by interfacial polymerization directly onto the top surface of the VACNT support layer. This RO membrane delivers a flux of 128.6 liter $m^{-2}h^{-1}$ (LMH) and 98.3% salt rejection at 15.5bar, opening an avenue for a leap over the water permeability at the rejection level that has been pegged at 5 LMH bar^{-1}over the past ten years. Formation of a thin PA layer by a modified

preparation method and ultrahigh porosity of VACNT support membrane are the main factors for the high-performance RO membrane.

Keywords: graphene oxide, microfiltration support layer, interlayer, vertically aligned carbon nanotube, desalination, reverse osmosis membrane, polyamide, interfacial polymerization, CNT supporting layer

Student Number: 2011-22879

Table of Contents

List of Tables

Chapter 1.

Chapter 2.

Chapter 3.

List of Figures

Chapter 1.

Chapter 2.

Chapter 3.

Chapter 4.

rejection diagram. The result of our works shows the best performance at at the same salt rejection.

Chapter 1.

Introduction

1.1. Motivation & Research background

Fresh water is the most important natural resource for human survival, such as food production, industrial productivity, energy production and the global economy. The earth's water storage capacity is about 1.4 billion cubic kilometers. Although the number is huge, saltwater (ocean) accounts for 97%, and freshwater accounts for only 3%. 68.7% of fresh water is glaciers on the north and south poles and permafrost on the mountains, 30.1% is groundwater, and less than 1% is rivers and lakes. Only 100,000 cubic kilometers of surface water and part of groundwater can be directly produced and used by people which accounting for about 0.3% of the total water.[1]

Global freshwater resources are not only in short supply, but the regional distribution is extremely uneven. According to regional distribution, freshwater resources in nine countries including Brazil, Russia, Canada, China, the United States, Indonesia, India, Colombia and Congo account for 60% of the world's freshwater resources. Figure 1-2. shows a global water resources distribution. About 1.5 billion people in 80 countries and regions, which account for about 40% of the world's total population, are under-resourced, and about 300 million people in 26 countries are extremely short of water. What's worse is that since the late 1970s, rapid warming in most parts of the world has exacerbated evaporation and may have altered the atmospheric circulation pattern. Both have contributed to the recent trend

of land drying. This has led to drought becoming a new climate “normal” [2] and the drought lasts longer. With the continuous expansion of the economy and population, the demand for fresh water is increasing. The shortage of fresh water has become an important issue affecting the economic and social development of many countries[3-5].

Figure 1-3. shows a Water Stress modelling for 2040 which predicts longer periods of hot dry weather in some areas[6]. Along with temperature changes, climate models predict some areas will have increased or reduced precipitation. Changes in rainfall create challenges with drought and flooding and higher temperatures increase water consumption and the demand for energy.

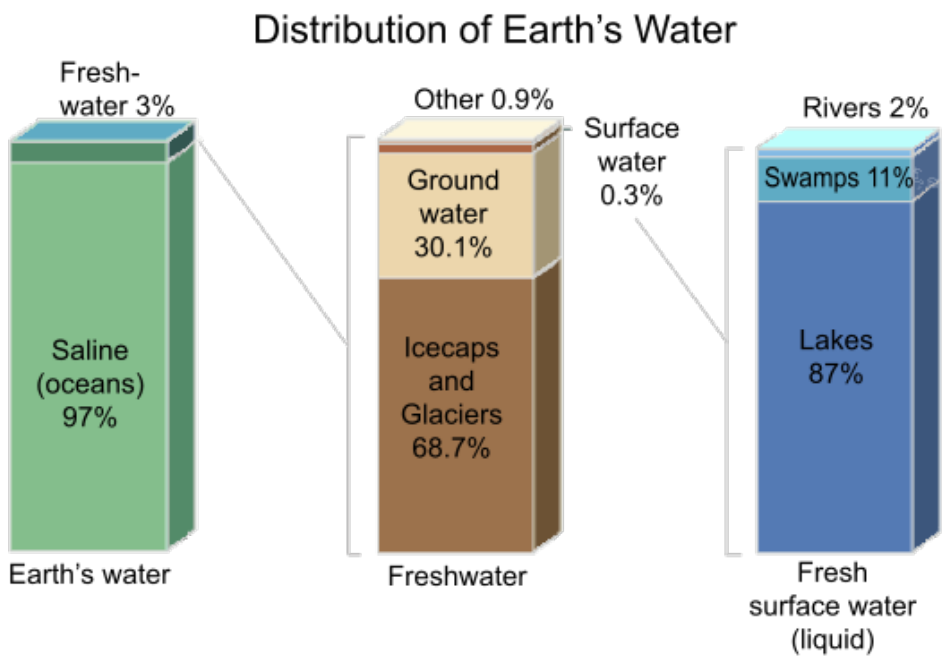

Figure 1-1. Distribution of Earth's Water

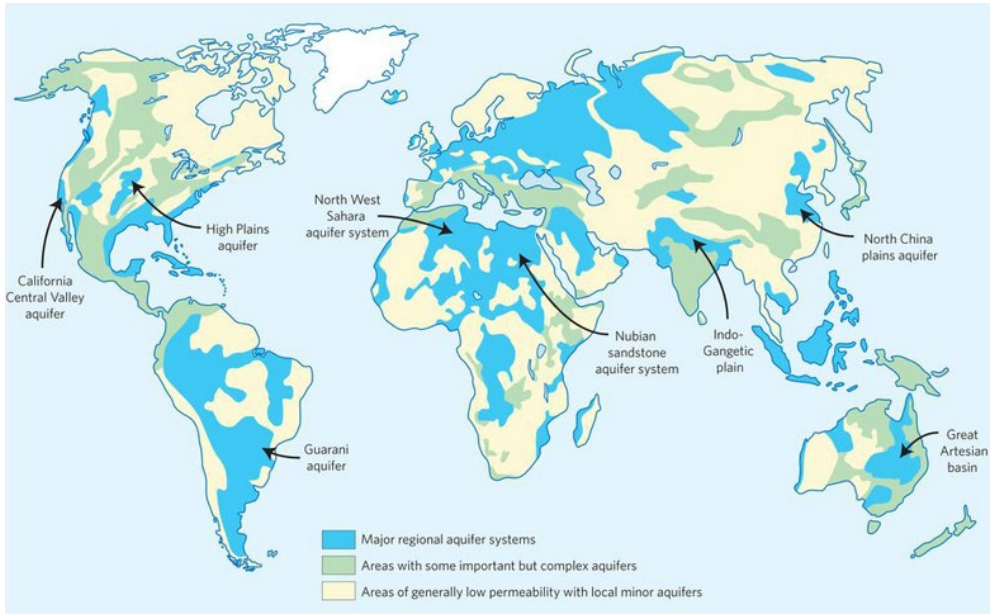

Figure 1-2. Global water resources distribution

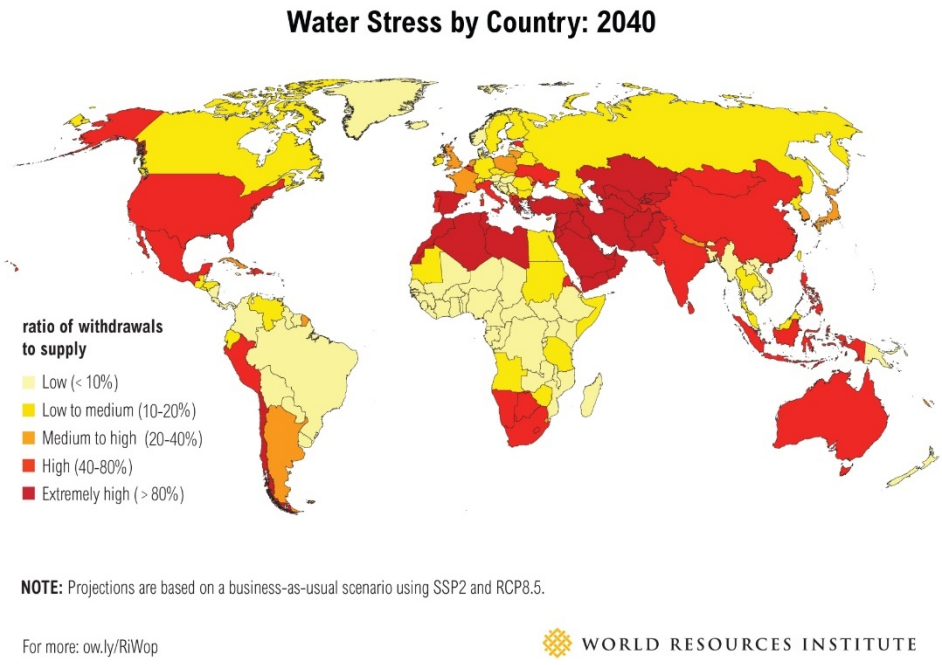

Figure 1-3. Water Stress modelling for 2040

In order to solve the gradual severe water crisis and meet the world's growing demand for clean water, not only the existing freshwater resources need to be protected, but new freshwater sources must be developed. Seawater desalination and wastewater treatment and recycling will be the main methods. In recent years, the proportion of membrane water treatment technology that has gradually emerged in the field of seawater desalination and sewage treatment is increasing, and membrane technology has become more and more concerned. The membrane technology is considered as the major trend in future water treatment options.

Membrane water treatment technology is superior to other techniques for water treatment such as chemical treatment, distillation, biodegradation or media filtration, because the water treatment with membrane technology does not require chemical additives, heat input, or regeneration of the used medium in principles. Membrane technology enables efficient, selective and reliable separations using gas separation, pervaporation, and industrial and environmental separation. Electrochemical membrane processes have increased dramatically over the past few decades, and pressure-driven membrane separation processes remain the most widely used membrane technology for water treatment applications. Typically, pressure driven membranes are classified according to the characteristic pore size and its intended applications[7].

As shown in Table 1-1 and Figure 1-4, the membrane is mainly classified into microfiltration, ultrafiltration, nanofiltration and reverse osmosis membrane

according to the pore diameter of the surface. The microfiltration membranes (MF) with a pore size of 10 to 0.1 micron can remove suspended solids, protozoa and bacteria in water; the ultrafiltration membranes (UF) with a pore size of 100 to 10 nanometers can remove macromolecules such as viruses, colloids and proteins; the nanofiltration membranes (NF) with a pore size of 10 to 1 nm can remove hardness, heavy metals and dissolved organic matter; the reverse osmosis membrane (RO) with the highest pore size of less than 1 nm is used for desalination, potable water production and ultrapure water production. In the water treatment membrane market, the reverse osmosis membrane has the highest occupancy rate. While commercial membranes perform well in many applications so far, the drive to produce new freshwater resources and to protect existing freshwater resources still have need of membranes with improved productivity, selectivity, stability and fouling resistance available at lower cost and with fewer manufacturing defects.

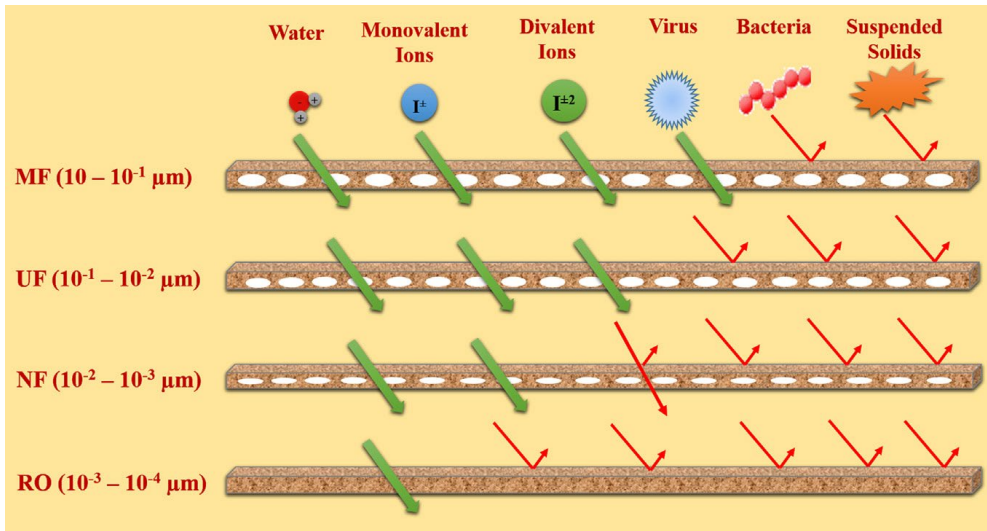

Figure 1-4. Membrane types and its removal ability

Filter Type	Pore Size	Operating Pressure (Bar)	Types of Materials Removed
Microfilter (MF)	10um-0.1um	0 - 2	Suspended Solids Bacteria, Large Viruses, Clay
Ultrafilter (UF)	100nm-10nm	1 - 7	Viruses, Organics, Proteins, Colloids, Starches, Silica, Dye
Nanofilter (NF)	10nm-1nm	3 - 20	Divalent Ions, Pesticides, Herbicides, Color-Causing, Organic Matter, Hardness Minerals, Toxic Metals, Chemicals of Concern
Reverse Osmosis (RO)	1nm-0.1nm	15.5 - 69	Monovalent Ions, Salts

Table 1-1. Membrane types and its characteristics

1.2. Thesis objective

Reverse Osmosis Technology

The normal osmosis process refers to a phenomenon in which a solvent naturally moves from a region of low solute concentration (high water potential) through a semipermeable membrane to a region of high solute concentration (low water potential). The driving force for the movement of solvent is a reduction in the free energy of the system as the difference in solvent concentration across the membrane decreases, resulting in osmotic pressure as the solvent enters the more concentrated solution. However, if a force is applied to the high-tension solution (high concentration solution), the pure solvent in the high concentration solution from a place where the osmotic pressure is high will flow to a place where the osmotic pressure is low as shown in Figure 1-5. This process is called reverse osmosis.[8]

Reverse osmosis differs from general filtration in that the mechanism of fluid flow is by osmosis across a membrane. The predominant removal mechanism in other membrane filtration is straining, or size exclusion, where the pores are larger than 1 nanometer. Therefore, regardless of parameters such as the solution's pressure and concentration, the process can theoretically achieve perfect efficiency. The reverse osmosis membrane is a non-porous membrane or a dense membrane and is generally considered to have a pore size of less than 1 nanometer. The primary removal mechanism comes from differences in solubility or diffusivity, and the process depends on pressure, solute concentration, and other conditions.[9]

The reverse osmosis membrane which developed in the 1970s combines its ability to handle various water sources, making it a powerful candidate for solving current and future water shortage problems. The reverse osmosis is currently the most effective technology for wastewater recovery (three-stage treatment) and one of the best techniques for brackish water and seawater desalination. The former is clearly an ideal solution for densely populated areas because it solves two problems simultaneously, namely wastewater treatment and increased freshwater supply.

The proportion of reverse osmosis technology in existing water treatment projects has reached 44% (Figure 1-6)[10, 11], and in seawater desalination plants, reverse osmosis technology has accounted for nearly 80%. For the operation cost of seawater desalination plants using reverse osmosis technology, the costs of membrane scale, energy consumption of high-pressure pump and membrane clarity and replacement cost account for more than 60% of the total cost due to the two factors of low membrane flux and membrane fouling (Figure 1-7)[12]. Therefore, it is undeniable to make RO desalination more economical by improving performance and efficiency. Despite this, multi-functional membrane materials seeking to provide higher permeability, high selectivity and high anti-fouling properties as well as operational robustness are still in progress. These studies are expected to benefit the water treatment industry with RO membrane by reducing energy costs, simplifying the pretreatment process, providing lower membrane maintenance costs, increasing plant capacity. In short, it is expected to significantly reduce capital investment and

operating costs both in the desalination industry and in wastewater treatment.

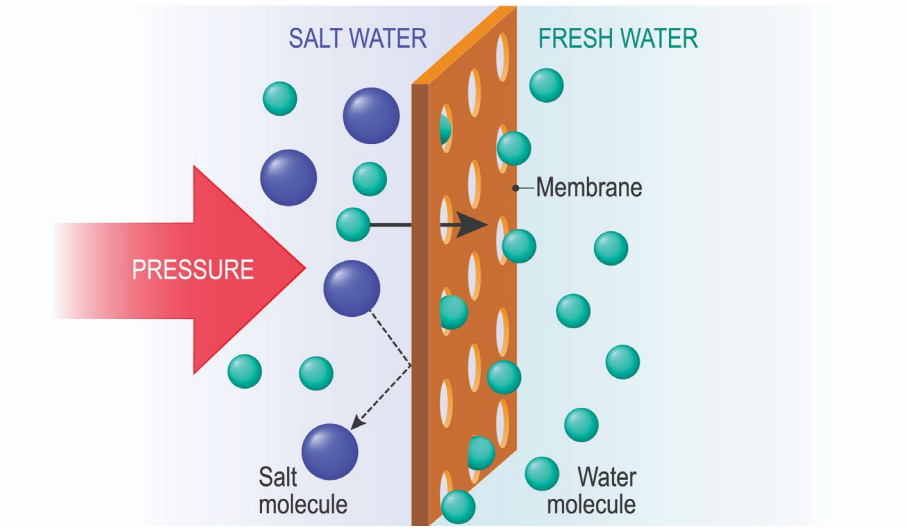

Figure 1-5. Process of reverse osmosis process

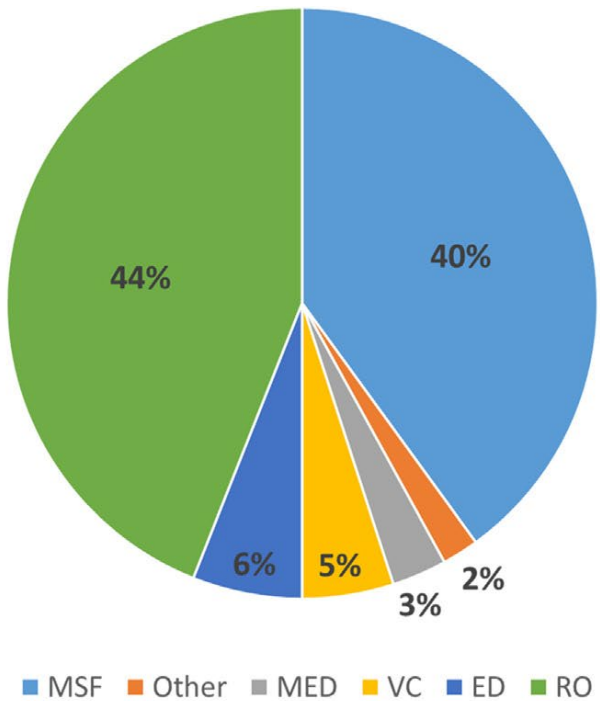

Figure 1-6. Distribution of global desalination production capacity by process technology. MSF is multi-stage flash thermal desalination, MED is multiple effect distillation, VC is vacuum compression, ED is electrodialysis, RO is reverse osmosis

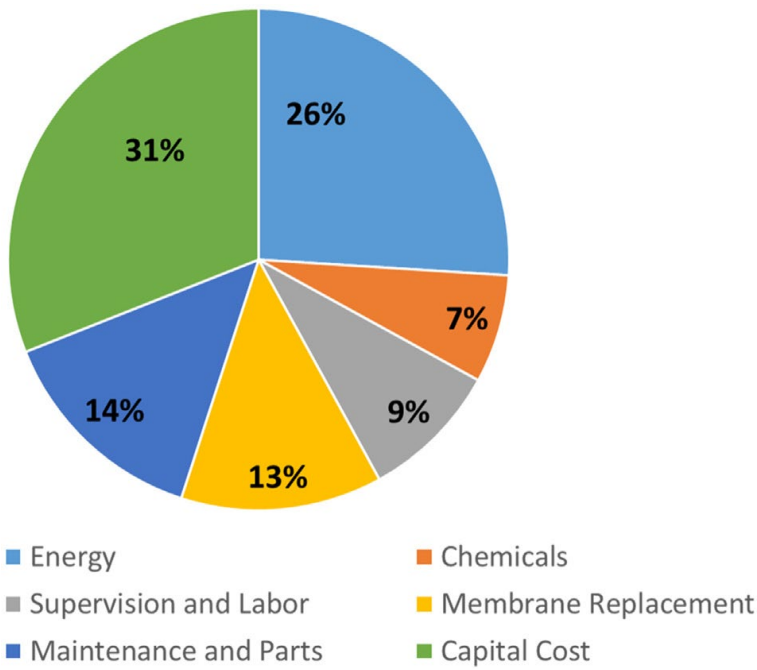

Figure 1-7. Typical seawater desalination plant cost consumption.

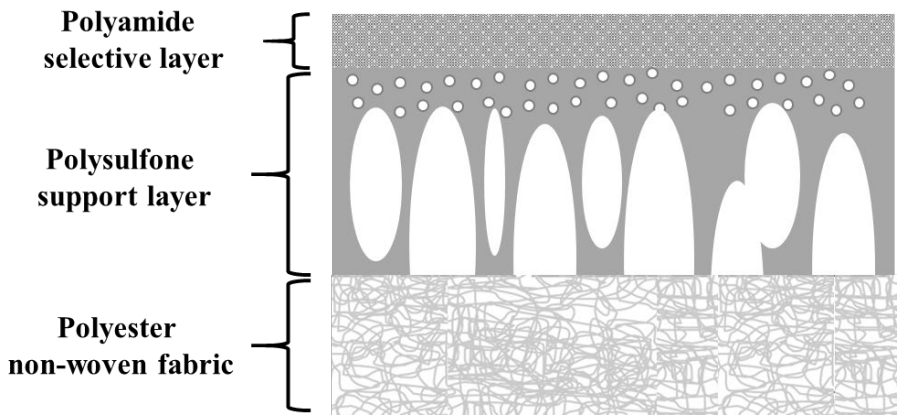

Figure 1-8. The structure of a traditional thin film composite reverse osmosis membrane

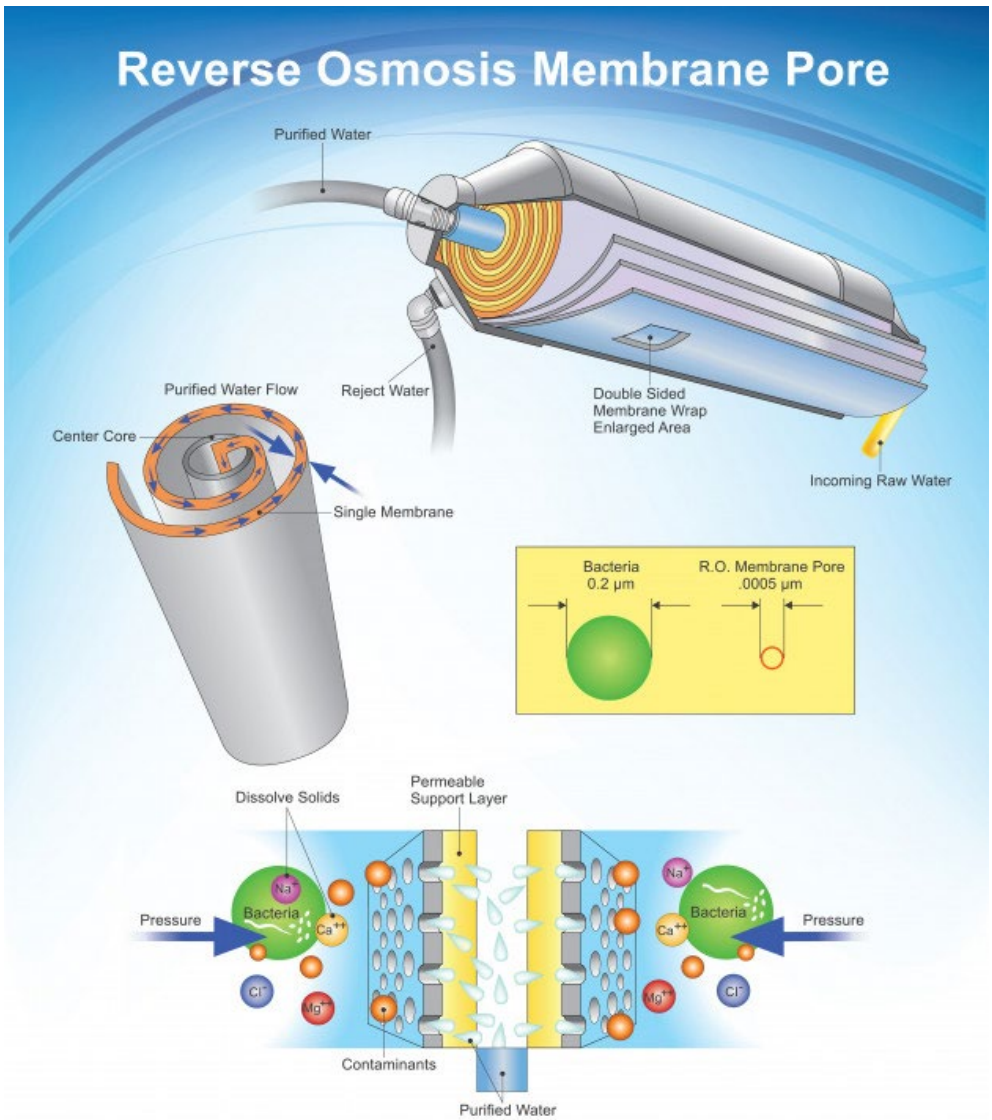

Figure 1-9. A commercial spiral reverse osmosis membrane

A typical thin film composite reverse osmosis membrane (TFC RO) consists of an ultrathin polyamide (PA) selective layer synthesized by interfacial polymerization (IP), a porous polysulfone (PSf), polyethersulfone (PES) or polyetherimide (PEI) support layer formed by phase inversion, and a polyester non-woven fabric layer as a mechanical backing (Figure 1-8). Figure 1-9 shows the construction of a general commercial reverse osmosis spiral membrane and its working principle.

The efficiency and cost of the RO process are closely related to water flux, desalination and fouling. The salt rejection and stability of the TFC membrane mainly depend on the properties of the PA. Since the invention of the TFC membrane, a large amount of research work has focused on the optimization of the PA layer by adjusting the monomer concentration, the reaction temperature, the reaction time, or by adding additives and nanoparticles or post-treatment conditions. In contrast, the contribution of the support layer to the separation performance of the entire TFC film has received less attention.

At present, some studies have shown that the support layer with larger surface pores can help to increase the water flux, but the salt rejection would decrease; the support layer with good hydrophilicity may cause the water flux to decrease.[13-15] However, the support layer of the PA layer has a limited surface porosity, which means that only those areas with open pores allow the transport of fluids, while the non-permeable areas limit the transport. These additional limitations increase the path length of the fluid transport (effective path) and allow the molecules at the pore

openings transport in the support to proceed at a higher rate ("funnel" effect).[16] The impact of this is that the water transport resistance through the TFC membrane becomes much larger than the intrinsic resistance of the polyamide film. Ramon et al. predicts that a support with smaller pores and higher surface porosity would form a more permeable TFC membrane. Therefore, improving the pore size distribution, increasing the pore size or increasing the surface pore number density can shorten the path of transporting water and alleviate the "funnel" effect[17]. Karan. et al. and Jiang. et al. [18, 19]isolated polyamide layers are combined with different supports and the composite films exhibit very different permeability, which strongly supports the assumption of the restrictive effect produced by the support.

Recently, many studies have shown that adding graphene oxide or carbon nanotubes as an additive to the support layer or the PA active layer or adding to support layer and active layer simultaneously can improve the performance of the RO membrane, but for the support layer and the synthesis of the PA layer on the surface thereof, the method still needs further study.

This research is focused on using carbon nanomaterials to improve or replace the traditional polymer support layers. The overall performance of the reverse osmosis membrane was improved from the improvement of the support layer of the reverse osmosis membrane, and furthermore, the importance of the synergistic effect between the selective layer and the support layer in the reverse osmosis membrane structure is discussed.

1.3. Overview on nanocarbon materials

1.3.1. Graphene

The graphene which discovered in 2004 is a planar film material composed of tightly packed carbon atoms with sp2 orbital hybrid hexagonal honeycomb crystal lattice and has only one carbon atom thickness two-dimensional. Graphene is currently the thinnest but hardest nanomaterial in the world, with an intrinsic tensile strength of 130 GPa and a Young's modulus (stiffness) of 1 TPa (150000000 psi)[20]. Secondly, graphene has a specific surface area (SSA) of up to 2630 square meters per gram[21] and a thermal conductivity of up to 5300 W/m·K, which is higher than that of carbon nanotubes and diamonds[22]. At normal temperature, its electron mobility exceeds 15000 $cm^2/V \cdot s$, which is higher than that of carbon nanotubes or silicon crystals[23], and its resistivity is only about 10^{-6} Ω·cm, which is lower than that of copper or silver, which is the material with lowest resistivity in the world.

There are many methods for manufacturing graphene, such as mechanical exfoliation, oxidation and reduction process, SiC epitaxial growth, and Chemical vapor deposition, etc. Among them, the oxidation and reduction process for separating graphene from graphite is the most widely used method for producing graphene which is relatively low in cost and mass-produced.

The oxidation and reduction process use a strong oxidant to intercalate oxidation in the interspace of the layered structure of graphite, so that there is a negatively charged oxidized functional group between the layers, which overcomes the van der

Waals force between the graphite layers. Then, the interlayer distance in the graphite crystalline is greatly increased by the intercalation of water molecules, and the graphene oxide could be peeled off from graphite. Graphene oxide could be further prepared by using a reducing agent to produce graphene as shown in figure 1-9.

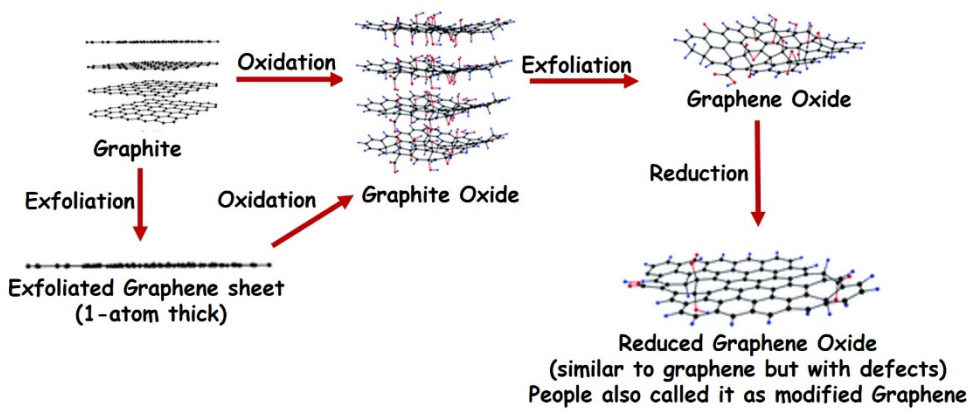

Figure 1-10. Schematic of graphene production by oxidation-reduction method

1.3.2. Carbon nanotube

The carbon nanotubes discovered in 1991 could be visualized as a graphene sheet that has been warped to a tube in which carbon atoms are arranged in sp2 hybridization at the corners of hexagons. Single-walled carbon nanotubes (SWCNTs) have tube shape consisting of a single shell of graphene as shown in figure 1-11. Multi-walled carbon nanotubes (MWCNTs) are composed of multiple layers of graphene sheets. A fixed distance, about 0.34 nm is maintained between the layers of these graphene sheets in multi-walled carbon nanotubes. The seamless tubes give rise to an outer diameter from about 1 to 30 nm but millimeter-sized lengths, which could yield a length-to-diameter ratio more than hundred thousand.

Carbon nanotubes have attracted great attention in a variety of latent applications as they possess exceptional mechanical properties, unique electrical properties, high chemical and thermal stability and a large specific surface area. Carbon nanotubes have the same hardness as diamonds but a good flexibility and stretch ability. The strength of carbon nanotubes is 100 times higher than that of the same volume of steel, and the weight is only 1/6 to 1/7 of steel. the radial Young's modulus of single-walled carbon nanotubes which were measured by using an atomic force microscope could be several to several tens of GPa.[24] so carbon nanotubes could be called "super fibers."

Presently three main methods employed for Carbon nanotubes (CNTs) synthesis are arc-discharge, laser ablation, and chemical vapor deposition (CVD). The CVD is

the most common routes of CNT synthesis which through vapor deposition of the desired carbon precursor on a suitable catalyst surface (figure 1-12). CVD is attractive because it allows tailored control on the CNT architecture with high purity and low defects while being easily scalable. Transition metal nanoparticles, especially iron, cobalt, nickel, and yttrium, either alone or grafted on suitable supporting materials, are favorably selected for the nucleation and growth of CNTs. The role of CNTs in applications lies in the variables, such as architecture, carbon precursor, carbon feeding gas, temperature, pressure, density, and chemical environment.

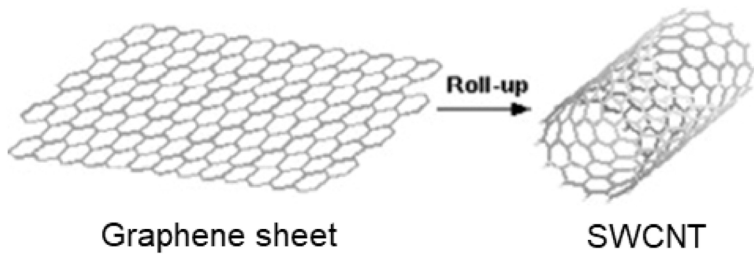

Figure 1-11. Formation of a carbon nanotube from a graphene sheet

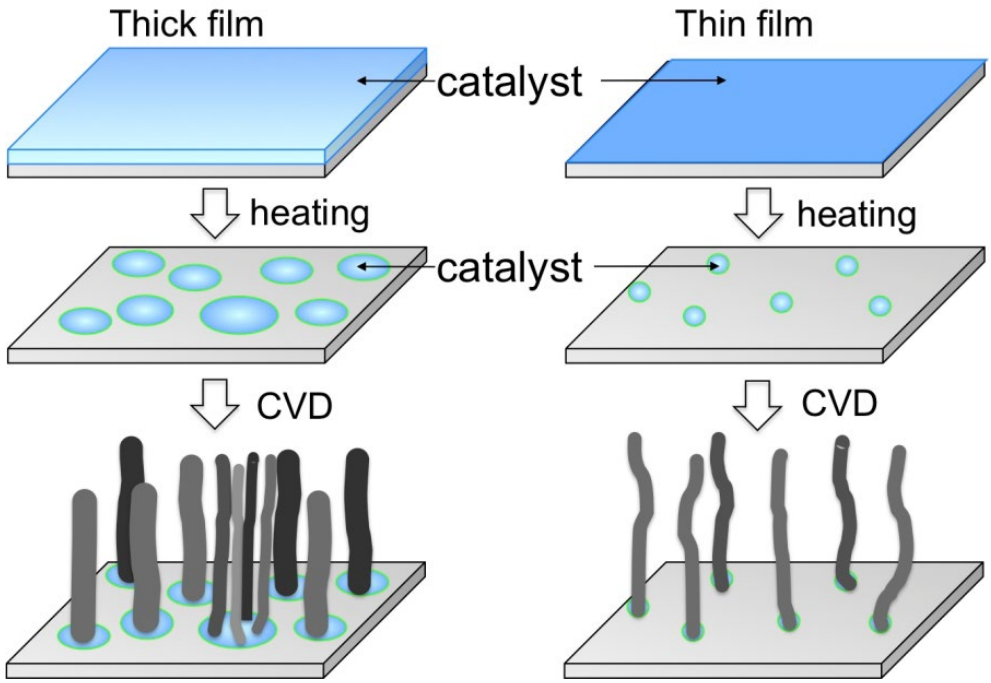

Figure 1-12. Schematic of Carbon nanotube forest production with different diameters by chemical vapor deposition (CVD)

1.4. Advantages of nanocarbon materials for reverse osmosis membrane

1.4.1 Graphene Oxide

The high performance of graphene oxide has become a consensus because of its high specific surface two-dimensional structure and a variety of surface-rich functional groups. Graphene has extremely large surface area, more than ~2,630m^2/g to be exact. And the atoms at the edges of a graphene sheet have special chemical reactivity. Graphene has the highest ratio of edge atoms of any allotrope. Defects within a sheet increase its chemical reactivity. This makes Graphene a perfect material to carry many hydrophilic functional groups to the utmost extent on surfaces and edges thereof, such as hydroxyl, carboxyl, carbonyl, and epoxy groups etc., which covalently bonded to carbon atoms in graphene(figure 1-13).

Secondly, Graphene is very light in weight due to its single atom thickness. When graphene oxide was added in support layer so most of the graphene would spontaneously assemble on the surface of the polymer membrane by driven by hydrophilic functional groups which is in contact with water during phase inversion processing. the attachment of graphene oxide to the surface of the polymer molecular chain can improve greatly hydrophilicity of the surface of the support layer.[25, 26]

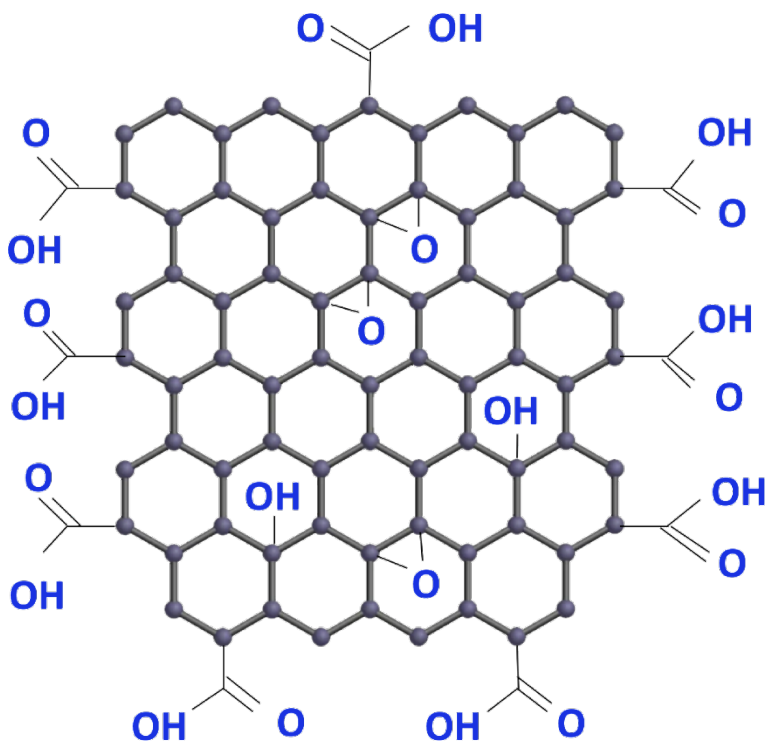

Figure 1-13. Graphene oxide molecular structure diagram

Combining the above two points, in order to improve the hydrophilicity of the support layer surface, the addition of the same weight of functionalized graphene composites is much better than simply mixing or adding oxidized metal nanoparticles or chemical additives. The hydrophilicity of the surface of the support layer where the functional groups carried by GO could control the travelling speed of MPD molecules coming out of the pores along the membrane surface, and eventually results in a smoother PA surface. In addition, the addition of GO could increase the porosity and pore size of the support layer, coordinating with the increased surface hydrophilicity, the water flux of the support layer would increase and further increases the water flux of entire RO membrane to a certain extent. Thirdly, Graphene has a very high mechanical strength. When graphene is added to the membrane polymer, the mechanical strength of the membrane can be improved. Then the pressure resistance of the pore and channels could be enhanced[27], as well as the tolerance to the cleaning of the membrane.

When graphene oxide was added in selective layer, that is, when graphene oxide is added to the aqueous phase in the interfacial polymerization process, graphene oxide sheet dispersed in the MPD aqueous phase could capture MPD molecules on its surface and controls the reaction orientation between MPD and TMC in the interfacial polymerization process, thus further improves the hydrophilicity and smoothness of the polyamide selective layer. the functional groups on the surface of graphene oxide could be linked with the remaining functional groups of TMC

molecules, and as a result, the PA molecule generated by interfacial polymerization process would enclose the GO sheets. In the case of active chlorine corrosion, GO could protect the integrity of PA molecules due to the chemical inertness of GO, thus reduces salt rejection loss.[28, 29]

The importance of hydrophilicity to reverse osmosis membranes includes the following: The hydrophilicity, negative charge and surface smoothness, in detailly, the functional groups of graphene ensured a relatively higher negative zeta potential, which may also prevent the attachment of dirt and its accumulation on the surface of the membrane. the hydrophilicity would suppress the hydrophobic-hydrophobic interaction between bacteria and the membrane surface. A negatively charged membrane surface could generate electrostatic repulsions against negatively charged bacteria and extracellular polymeric substance (EPS). In addition, the hydrophilic functional groups could capture water molecules to form a moisture layer on the surface of the membrane. so that most of the lipophilic contaminants and bacteria are unable or less likely to adhere to the surface of the membrane.[30, 31] Therefore, the anti-fouling of the entire membrane and the recovery ability after backwashing could be improved and lifetime of the membrane could be extended.

1.4.2 Carbon nanotube

CNTs are fascinating in advanced membrane technologies for water treatment since they provide low energy solution. CNT-membranes provide near frictionless water flow through them with the retention of a broad spectrum of water pollutants. The smooth hydrophobic walls and inner pore diameter of CNTs allow ultra-efficient transport of water molecules.

Dispersed carbon nanotubes can be used as additives for water transfer channels or adsorption media in membranes technology.[32-37] Well-aligned CNT can serve as robust pores in membranes for water treatment and decontamination applications. The hollow structure or out wall surface of CNT provides frictionless transport of water molecules, and this makes them suitable for the development of high fluxing separation techniques (figure 1-14). Appropriate pore diameters or spacing (pore dimensions of the outer wall) can constitute energy barriers at the channel entries, rejecting salt ions and permitting water through the nanotube hollows or out-walls. It is also possible to modify CNT pores or out wall spacing to selectively sense and reject ions. Thus, CNT membrane can be used as a 'gate keeper' for size-controlled separation of multiple pollutants. Besides, it has antifouling, self-cleaning and reusable functions.[38, 39]

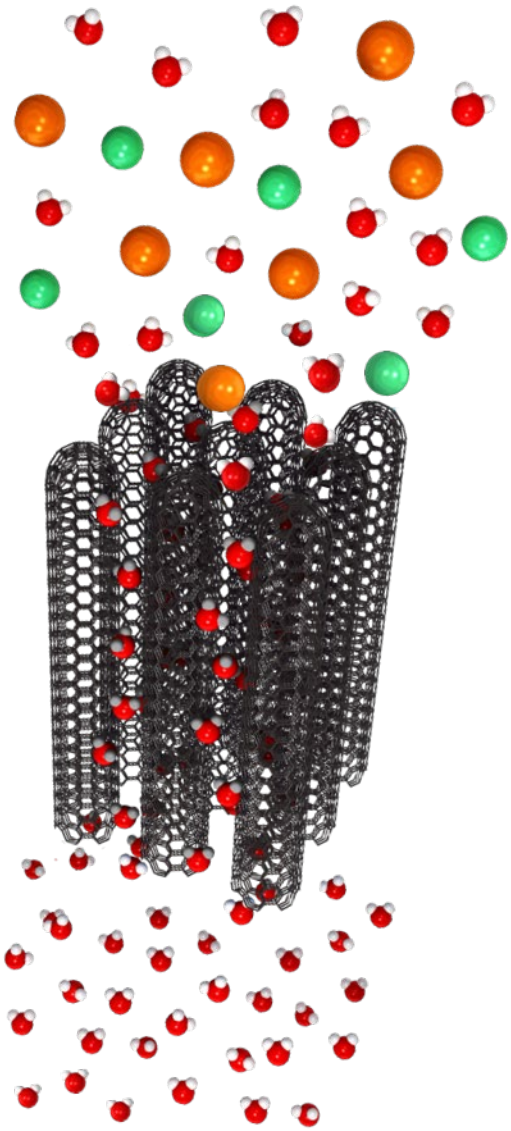

Figure 1-14. An illustration of Vertically aligned carbon nanotube (VACNT) membrane.

Chapter 2.

Reverse Osmosis Membrane with Graphene Oxide interlayer with microfiltration support membrane

2.1. Introduction

Fresh water scarcity is widely acknowledged as a serious problem, which is getting worse with population growth and economic development.[40] In the face of water shortage, seawater desalination and waste water treatment technologies have very broad application prospects. Reverse osmosis (RO) is the most widely used technology to make fresh water from salty water, called desalination process, as a cost-effective and highly efficient technology.[10, 41] Traditional reverse osmosis (RO) membranes, which is a thin film composite (TFC) consisting of a highly cross-linked polyamide (PA) layer on the surface of a porous supporting layer, still have a low water flux due to the thickness and roughness of the PA layer, and the resistance of the support layer. The porous support membrane layer is an ultrafiltration membrane made of a polymer such as a finger shape and asymmetric Polysulfone or Polyethersulfone with several tens of nanometers in diameter generally. The vast majority of commercial RO membranes have surface pore sizes between 20 and 40 nanometers. The larger pore size can reduce the effective path of water molecules entering the water channel after passing through the PA layer, thereby greatly increasing the water permeability. However, a larger pore size

increases the diffusion rate of MPD to the organic phase, and the higher MPD diffusivity is also higher MPD solubility. Therefore, the PA layer synthesized by interfacial polymerization on the surface of the support membrane will form less crosslinking and excessive defects, and even the interfacial polymerization cannot react due to less MPD solution by weak capillary force [13, 17]. Secondly, there is a lack of support across the PA layer above the large pore, which will cause damage to the PA layer under high water pressure during water treatment process. In summary, the large pore size will result in a higher water flux, salt passage, thickness, and roughness as shown in figure 2-1. Although a small pore size can synthesize a denser PA to obtain a higher salt rejection, the effective path of water molecules entering the water channel after passing through the PA layer will be greatly increased, and finally the water flux of the synthesized RO membrane is greatly reduced. Therefore, for the support layer of the RO membrane, the optimizing pore size and increasing pore density on the surface of support layer are the best solutions, which is also the biggest challenge.

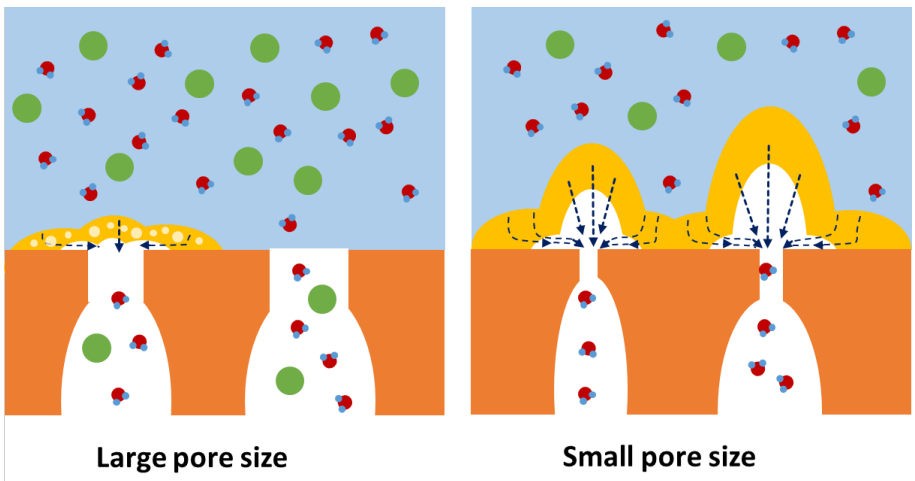

Figure 2-1. Problems of RO membranes using large pore size and small pore size of support layers

Graphene, A two-dimensional carbon nanomaterial with a single atomic thickness has received great attention in recent years. Graphene has a hydrophobic smooth surface and chemically modified edges as well as excellent mechanical strength. It has been utilized in many studies as an additive in water treatment membranes in more than a decade. The graphene oxide membrane formed by filtration or layer by layer self-assembly can be used as a nanofiltration membrane. The water flux of a GO membrane having a thickness of only a few layers or tens of layers of GO sheets does not decrease as the number of GO sheets increases[42]. In this work, we immobilized graphene oxide sheets as an assistant interlayer on the surface of the microfiltration membrane support layer with high flux and large pore size. The interlayer graphene oxide sheets can control the diffusion of the MPD molecules to the organic phase when the support layer is filled with an aqueous solution of MPD monomer. Then finally, a smooth and thin PA selective layer extends the surface of the graphene oxide interlayer confined interfacial polymerization. The performance of the final reverse osmosis membrane can be greatly improved due to the reduced resistance of the support layer and the confined interfacial polymerization of graphene oxide interlayer.

2.2 Experimental Section

2.2.1 Materials

Graphite was purchased from Qingdao Huatai Lubrication and Sealing Technology Co., td. Potassium permanganate powder, Sulfuric acid(98%), Hydrogen peroxide(30%), n-Hexane, Glutaraldehyde aqueous solution and Polyvinyl alcohol 1500(PVA, MW: 66000) were purchased from Daejung Chemicals & Metals Co., LTD. Polyethersulfone (PES) Microfiltration Membranes was purchased from Hangzhou Shengju Environmental Protection Technology Co., LTD. Polysulfone p-3500 was purchased from solvay Co., LTD. M-phenylenediamine (MPD, MW:108.14) and trimesoyl chloride (TMC, MW:265.48) were purchased from Sigma-Aldrich and used as received. Deionized (DI) water was prepared in a Purelab option-Q purification system.

2.2.2 Preparation of various sizes of Graphene oxide nanosheets

2.2.2.1 Large and medium size graphene oxide nanosheets

The large and medium size graphene oxide nanosheets were used 100 mesh and 12000 mesh graphite powder materials respectively. The average size of 100mesh and 12000mesh of graphite particle is 150um and 1.1um respectively. The GO nanosheets synthesis process is as follows: 1 gram of graphite powder and 6 grams of potassium permanganate powder were added into a glass reactor and stirred uniformly with a stirrer continuously, cooled and kept at a constant temperature lower than 10ºC. A total volume of 100 milliliters of 98% concentrated sulfuric acid was added slowly, and the mixture was stirred thoroughly for 30 minutes. The reactor was heated to 45ºC and kept at this temperature for 6 hours, then the reactor was cooled and kept at a constant temperature lower than 10ºC, and 100 grams of ice cubes made of deionized water were added into the reactor, and the stirring was continued until all ice melted and there was no more fluctuation of the temperature of the solution. The reaction was stirred continually, and 50 milliliters of hydrogen peroxide were slowly added until the solution turned yellow and no more gas was generated. The reactor was charged with 100 milliliters of butanol. The solution was continuously stirred, heated, and kept at a constant temperature of 40-50ºC, and stirred for 1 hours, and finally the device was cooled to room temperature and the stirring was stopped. The solution in the reactor layered. The upper layer was a

brown butanol solution containing the graphene oxide generated by reactions. The bottom layer was a clear and colorless liquid containing sulfuric acid and a small amount of hydrogen peroxide, within which there was a partially crystallized solid. The clear liquid and the solid in the lower layers were drained. The brown organic solution was separated and subjected to a filter pressing process via a pressure filter to obtain a final solid. The solid was added into an isopropanol or ethyl acetate solution to be rinsed and filtered repeatedly to eliminate the impurities like sulfuric acid and then subjected to a drying process to finally obtain the graphene oxide powder.

2.2.2.2 Small size graphene oxide nanosheets

To synthesis small size graphene oxide, 80 ml of a 2 mg/ml medium size GO aqueous solution was prepared. Next, 8 ml of 30% H_2O_2 aqueous solution was added and stirred for 4h at 100 °C for fragmentation of GO nanosheet. After the reaction, small size graphene oxide nanosheet (SGO) was acquired via filtration (PTFE membrane; Omnipore; JHWP 04700; pore size: 450 nm) and washed with DI water sequentially. After filtration and washing, the SGO was dried in a vacuum oven at 70 °C for 24h.

2.2.3 Preparation of graphene oxide interlayer on support layer

Yellow-brown dispersion of exfoliated graphene oxide was prepared by dissolving 20 mg of graphite oxide in 200 mL of deionized water by sonication with ultrasound sonicator for 3 hours. After sonication, the insoluble fraction was allowed to sediment and supernatant was collected. 1 wt% PVA solution used for Layer by Layer assembly was prepared by dissolving 1g of PVA powder in 100mL of 80 ºC deionized water under vigorous stirring for 1 hour. The polyethersulfone (PES) microfiltration membrane was washed with ethanol and deionized water respectively and dried in air. Then the PES membranes were pretreated in a 1 wt% PVA aqueous solution for 5min and drying at room temperature.

The overall process of LBL deposition of heterogeneous ultrathin layer of PVA/GO consists of a cyclic repetition of the following steps and as shown in Figure 2-2 : (1) the PES microfiltration membrane was gently placed to the surface of the 1 wt% PVA aqueous solution (upside towards the solution), the membrane floats on the surface of the solution for 2 min; (2) remove the membrane and rinse with DI water, thoroughly for 30 sec and gently dried in air at room temperature; (3) the membrane was gently placed on a 0.1 mg/mL GO aqueous dispersion solution surface, the membrane floats on the surface of the solution for 2 min with the same way as above; (4) remove the membrane and rinse with DI water for 30 sec and again gently dried in air at room temperature. This procedure gave a single deposition cycle,

and the cycle could then be repeated as necessary to obtain the desired number of PVA/GO bilayers. In order to prevent cross-contamination risk and strengthen the combination between organic particles and polymer matrices, membranes after bilayers coating were immersed into 2 vol % solution of glutaraldehyde for 1 min to allow for cross-linking.

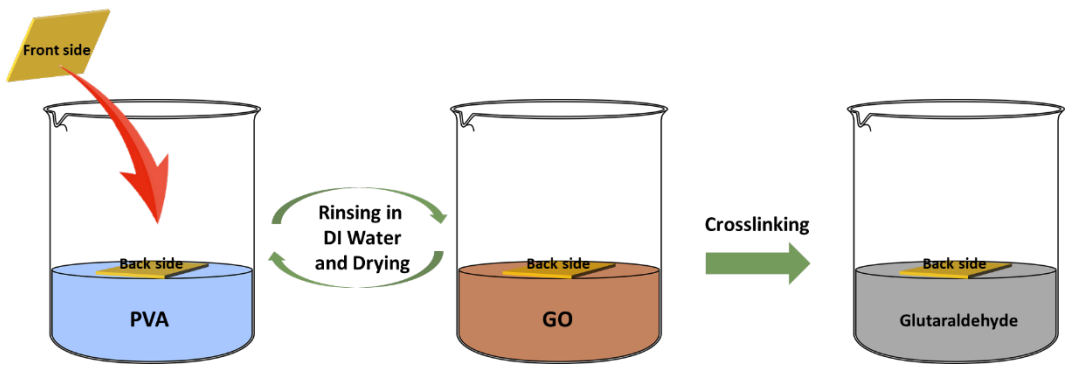

Figure 2-2. Process of Layer-by-layer deposition process of PVA/GO bilayers

2.2.4 Preparation of ultrafiltration support membrane

7 grams of Polysulfone polymer was dissolved in 43g 1-methyl-2-pyrrolidinone by stirring for 12 h at 60°C. After sonication for 1 h, the polymer solutions were kept for 12 h at 25°C without stirring until bubbles disappeared in the solution prior to casting. Then the polymer solution was drawn down on a glass pane using a micrometric film applicator (Elcometer 3570, Elcometer). The nascent support layers were then immersed in a water bath for 12 h at room temperature for entire liquid–liquid demixing.

2.2.5 Preparation of RO membrane:

RO membranes were prepared by forming a polyamide selective layer on top of the as-prepared GO coated MF support layer via interfacial polymerization.

Firstly, an aqueous solution of 3w% MPD was coated on support membrane surface for 2mins. Secondly, the solution was discarded, and then the residual droplets were removed by a rubber air blower from the membrane surface. Thirdly, a n-hexane solution of 0.15wt% TMC was poured on the membrane and reacted for 60 s, followed by rinsing the membrane surface using pure n-hexane. Finally, the membrane was treated at 70 °C for 5 min, and the fabricated RO membranes were rinsed carefully and stored in deionized water at room temperature prior to testing.

2.2.6 Characterization

Scanning electron microscopy (SEM) analysis was performed using a Hitachi S-4800 field-emission electron microscope at an acceleration voltage of 10-15KeV. AFM (Atomic Force Microscope) measurement was performed using a Park Systems NX-10 Atomic Force Microscope. The chemistry structure of GO nanosheets was characterized by X-ray photoelectron spectroscopy in an UHV multipurpose surface analysis system (SIGMA PROBE, Thermo, UK) operating at base pressures <10-9mbar. The photoelectron spectra were excited by an Al Ka (1486.6eV) anode operating at constant power of 100 W (15 KV and 10 mA).

2.2.7 Membrane Performance Tests

Pure Water Permeability of support membrane was tested using a dead-end system with an effective square area of approximately 7.8 cm2 at 1 bar operating pressure with DI water as the feed. The permeated water through the membrane during a given time period was measured. And the PWP calculate using Equation:

$J_w = Q/\Delta P*A$

Where Q and ΔP refer to the volumetric permeation rate of pure Water (Lh^{-1}) and the transmembrane pressure (bar), respectively. A is the effective area of the membrane (m^2).

RO Membrane performance was tested using same dead-end system and a 2000 mg/L NaCl aqueous solution as the feed. The operating pressure was 15.5 bar. Water flux (J) was determined from the aggregate sum of the gathered permeate (V) during a specified period of time (t), i.e., J ($Lm^{-2} h^{-1}$) = V/At, where A is the area of the top surface of outer-wall VACNTs. Salt concentrations of the permeate (C_p) and feed(C_f) were estimated with a conductivity meter (Seven Compact, conductivity S230), and salt rejection(R) was calculated by the the equation: $R (\%)= (1-C_p/C_f) * 100$.

For each set of result, at least three independent samples were tested for reliability. Each sample was tested for at least 12 hours to ensure the stability of water flux and salt rejection.

2.3. Results and discussion

2.3.1 Graphene oxide sheets

In order to obtain graphene of different sizes, we first used two different sizes of graphite powder raw materials of 100 mesh and 12000 mesh. The graphite particles of 100 mesh graphite powder are all below 150 um, and the graphite particles of 12000 mesh graphite powder are all about 1.1 um. Although graphite particles contain graphene sheets of different sizes at the same time, it is expected that relatively large-diameter graphene sheets can be obtained by large-diameter graphite particles, and relatively small-diameter graphene sheets can be obtained with small-diameter graphite particles. The two graphite powders were subjected to oxidation treatment via a modified Hummers' method, and the obtained graphene oxide powder was further prepared into a dispersed aqueous solution using a high-pressure homogenizer. These two kinds of graphene oxide nanosheets were labeled as LGO (Large size Graphene Oxide nanosheets) and MGO (Medium size Graphene Oxide nanosheets) respectively. In order to obtain a smaller diameter graphene sheet, we performed an oxidative-etching reaction on MGO, and the obtained graphene oxide nanosheets were labeled as SGO (Small size Graphene Oxide nanosheets). SGO can be easily prepared by heating a homogeneous aqueous mixture of GO and H2O2 at 100 °C for few hours under stirring. After removing residual H2O2 by centrifuging and washing the reaction mixture, the SGO can be easily dispersed in water to form a stable aqueous dispersion. the oxidative-etching reaction mainly initiate and

propagate within the oxygenic defect regions, leading to the preferential removal of oxygenated carbon atoms and generation of carbon vacancies that gradually extend into nanopores in the basal plane. Extending the reaction time would lead to a more aggressive etching of GO, enlarging the pore size, breaking the sheets, so that eventually the larger diameter graphene is broken to form more small diameter graphene sheets[43].

Figure 2-3 shows the results of AFM characterization. The AFM image and size distribution show the large size of GO with diameter of hundreds nm – 10um, medium size of GO with diameter of hundred nm – 2um and small size of GO with diameter of dozens nm – 1um. The edge image and height distribution indicate that all the GO nanosheet with the thickness of about 1 nm. A significant difference in the size distribution of the three types of GO nanosheets can be obtained by these AFM images.

To further confirm the chemical bonding and chemical structure of 3 types of graphene oxide nanosheets, XPS was performed. The C 1s signal in GO membrane clearly shows the presence of C-C, C-O-C, C=O, and O–C=O, which correspond to 284.6 eV, 286.7 eV, 287.9 eV and 289.1 eV (figure 2-4)[44].

From Table 2-1, The relative content of the oxygen-containing functional groups on the GO nanosheets surface can be judged by measuring the ratio of oxygen element of GO nanosheets since these functional groups all contain oxygen., which guarantees sufficient oxygen-containing functional groups for chemically cross-

linking reactions.

MGO has the most oxygen-containing functional groups because the smaller size has more edge length which can carry more functional groups with the same mass of GO nanosheets. Although SGO, which from the cracking of large-sized graphene oxide nanosheets by removing oxygen-containing carbon atoms using hydrogen peroxide and generating carbon vacancies, has the smallest size. The production process of SGO causes loss of oxygen-containing functional groups (especially carboxylic acid groups) in GO nanosheets, so SGO has the lowest oxygen content. According to the Lerf-Klinowski's GO model, carboxylic groups exist at the edges of GO mostly, and the reaction kinetics of the reaction on the GO nanosheets begin from edges and transfer to center, which means that the carboxylic acid groups on the edges are first decomposed by the oxygen radical attack by hydrogen peroxide[45].

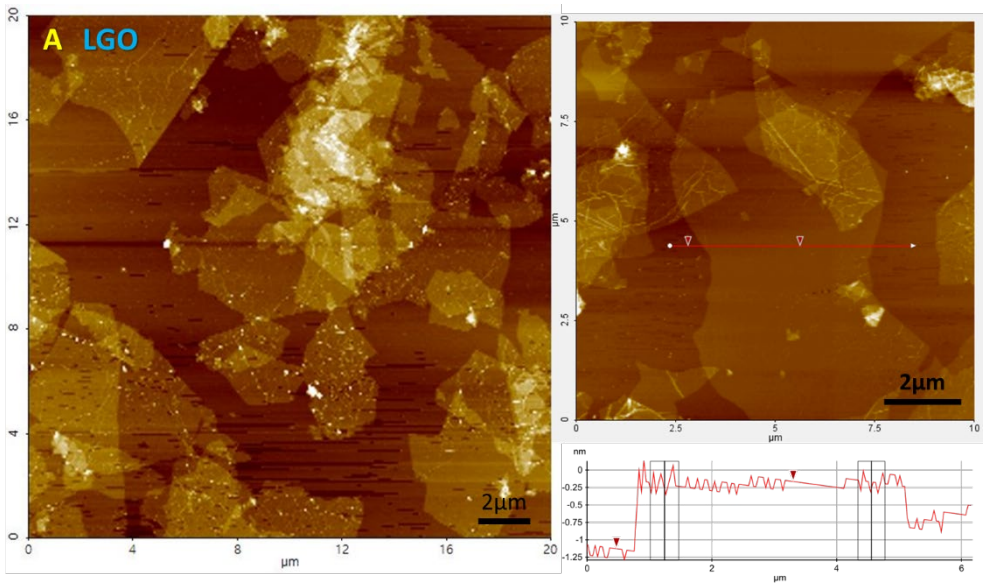
A LGO
2µm
µm
2µm
µm
nm

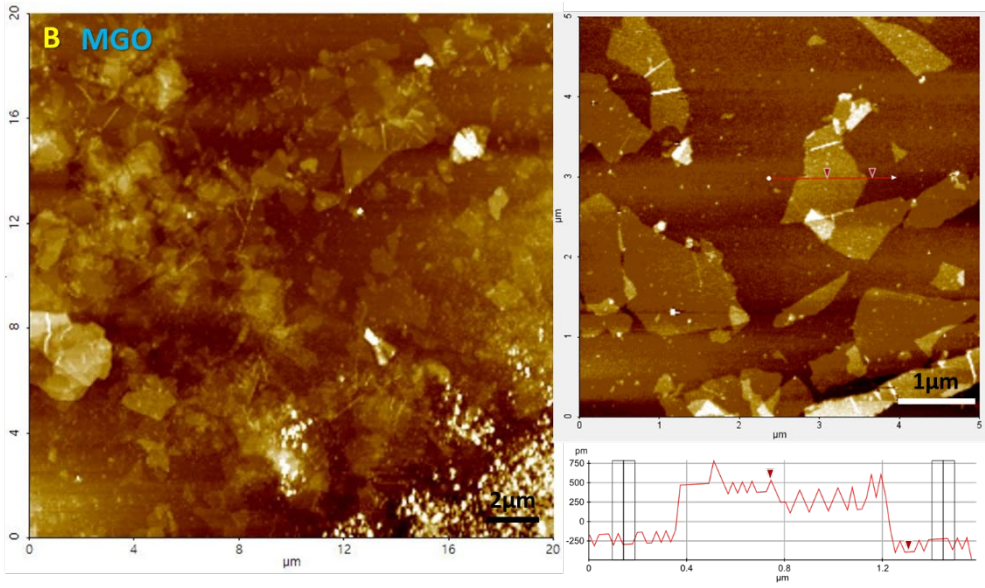
B MGO
2µm
µm
1µm
µm
pm

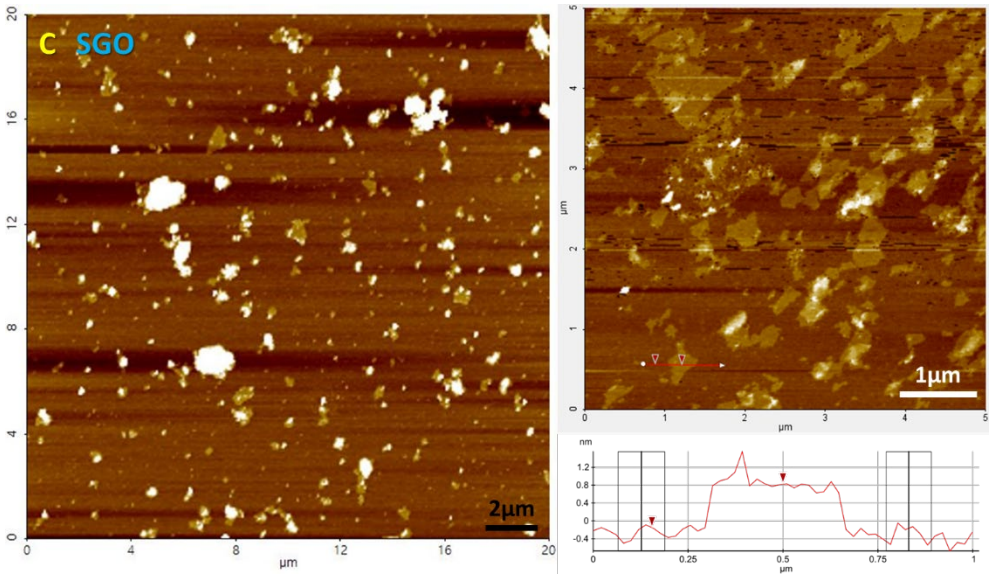

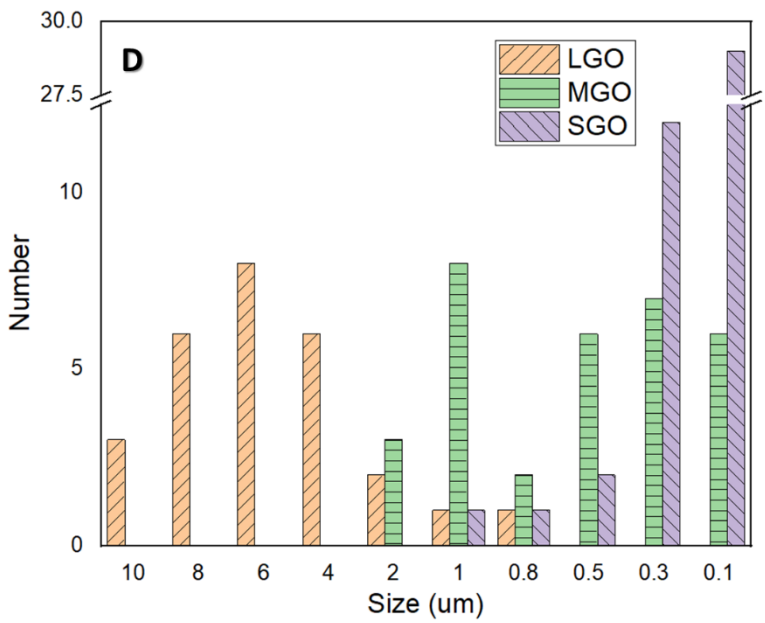

Figure 2-3. AFM images of (A)Large Size, (B) Medium Size, and (C) Small size Graphene Oxide nanosheet on mica plates. and (D) size distribution of GO nanosheet

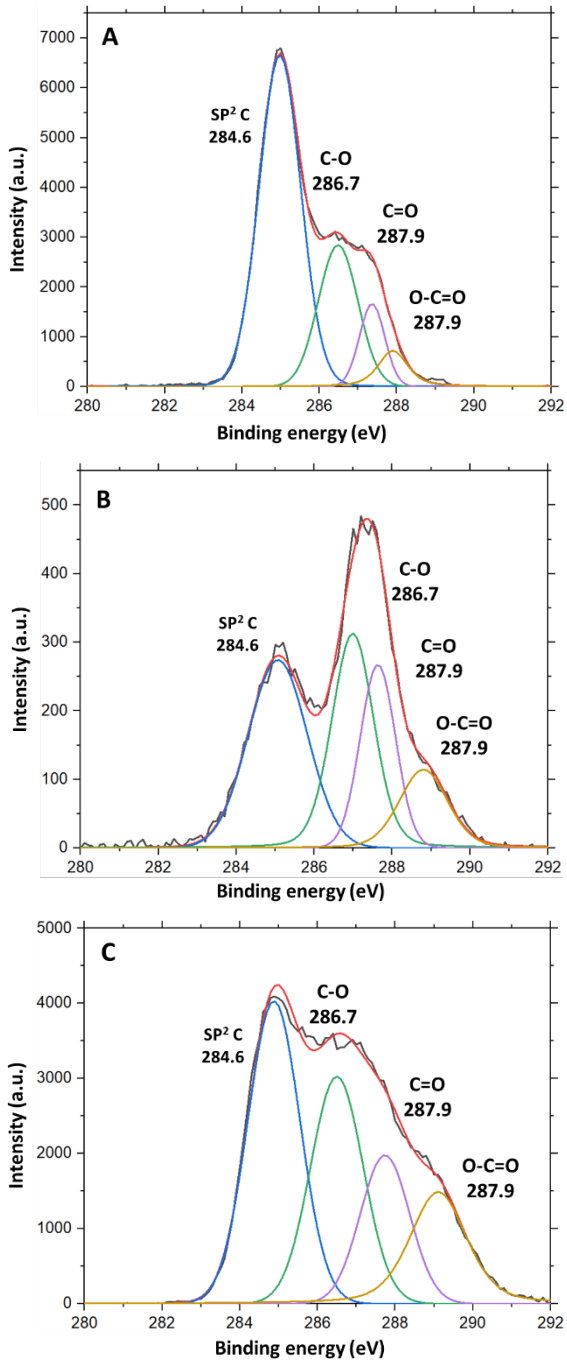

Figure 2-4. C 1s XPS spectra of (A) LGO, (B) MGO, and (C) SGO nanosheets

Table 2-1. Elemental composition of LGO, MGO and SGO

Element / Type	C (AT. %)	O (AT. %)
LGO	67.92	32.08
MGO	58.38	41.62
SGO	69.96	30.04

2.3.2 MF Membrane (0.22um) with GO interlayer

A 0.22um commercial microfiltration membrane with a surface pore size between 2 microns and hundreds of nanometers was uesd and the pores have a splitlevel structure (figure 2-5). The MF membranes was washed and dried before use, and the surface was pretreated with PVA coating. As show in figure 2-6, subsequent a traditional layer-by-layer deposition process of sequentially coating a surface with PVA and GO nanosheets by contacting a membrane with dilute solutions of the components is employed to prepare the membranes. PVA, an uncharged and water-soluble polymer, is used in the traditional electrostatic LBL technique. Nevertheless, carbon bound hydroxyl groups in each unit of PVA can associate with the oxidation functional groups of graphene oxide through covalent or hydrogen bonding, resulted in good adhesion. It is supposed that the hydrogen-bonding interactions between GO nanosheets and PVA can drive the reproducible layer-by layer composite deposition to fabricate ordered inorganic/organic periodic nanostructure, which would have analogies with the brick-and-mortar arrangement.[46, 47]

Figure 2-7, 2-8 and 2-9 shows the surface morphologies of the 0.22um MF support membrane with 1-4 cycles PVA/LGO, PVA/MGO, and PVA/SGO bilayers interlayer deposition by scanning electron microscopy (SEM) respectively. Hereinafter, 1-4 cycles PVA/LGO, PVA/MGO, and PVA/SGO bilayers interlayer will be simply referred to as n-xGO interlayer, where n is the number of bilayer deposition cycles and x is the type of GO nanosheet.

When the surface of the MF support membrane treated by the PVA is contacted with the graphene oxide dispersion solution, the pores are not attractive to the graphene oxide nanosheets because there are no PVA molecules on the pores. However, the PVA molecules on the flat surface around the pores can link and adsorb the GO nanosheets. When a larger size GO nanosheet is attached to the surface near the pore, the GO nanosheet could cover part or even the entire pore. After the first GO interlayer deposition, although there are many pores above the support layer of the microfiltration membrane covered by GO nanosheet, there are still many large pores that are left or not completely covered. The smaller the GO nanosheets, the more pores are retained or not completely covered. Our predictions can also be confirmed by figure 2-7 A, 2-8 A, 2-9 A. Through the second, third, and subsequent layer-by-layer deposition processes, as the number of GO interlayers increases, the pore size of the surface of the microfiltration membrane is gradually covered by GO nanosheets as show in figure 2-7 B-D, figure 2-8 B-D and figure 2-9 B-D. Since the surface-covered GO nanosheets layer is very thin, these GO nanosheets above the pores are slightly recessed toward the inside of the pores due to lack of supporting force, so even if the GO nanosheets completely covers the surface of the MF support membrane and the thickness of the GO layer is very thin, the shape and location of the pores on the surface of the MF support are still clearly identifiable.

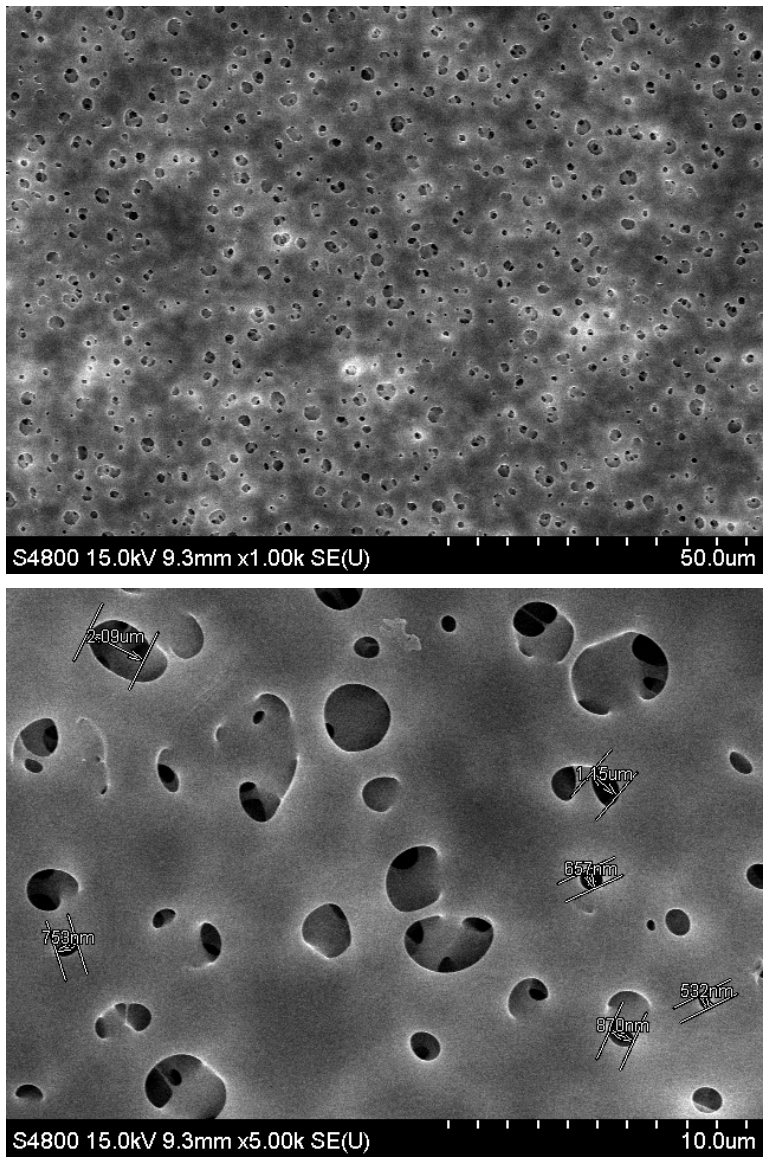

Figure 2-5. Low and high magnification Surface SEM images of commercial microfiltration membrane (0.22um)

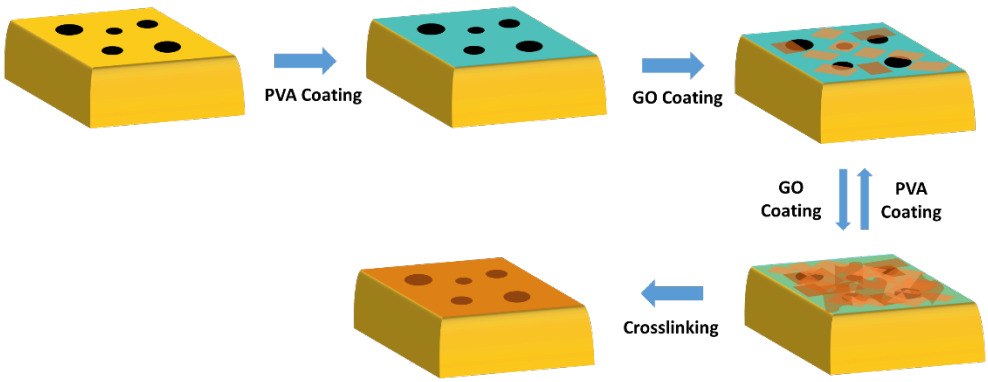

Figure 2-6. Schematic diagram of Layer by Layer deposition of PVA/GO bilayers

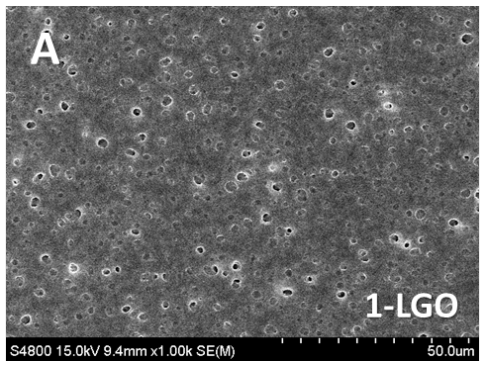
A
1-LGO
S4800 15.0kV 9.4mm x1.00k SE(M)
50.0um

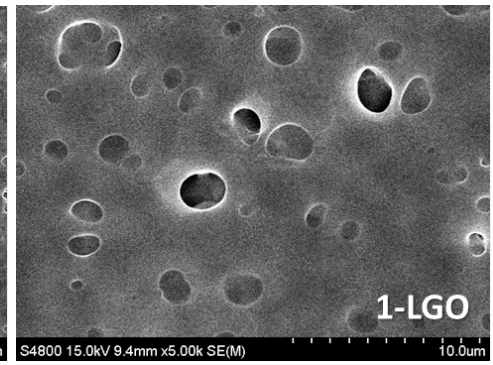
1-LGO
S4800 15.0kV 9.4mm x5.00k SE(M)
10.0um

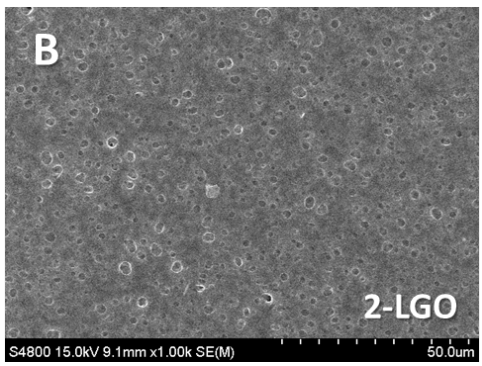
B
2-LGO
S4800 15.0kV 9.1mm x1.00k SE(M)
50.0um

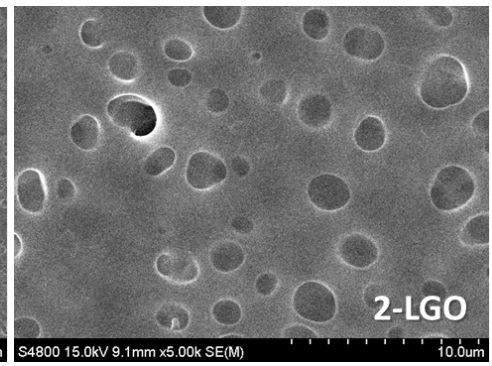
2-LGO
S4800 15.0kV 9.1mm x5.00k SE(M)
10.0um

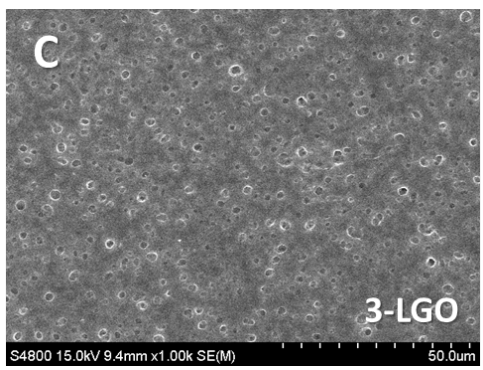
C
3-LGO
S4800 15.0kV 9.4mm x1.00k SE(M)
50.0um

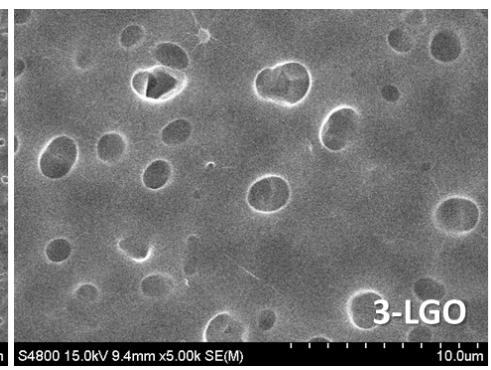
3-LGO
S4800 15.0kV 9.4mm x5.00k SE(M)
10.0um

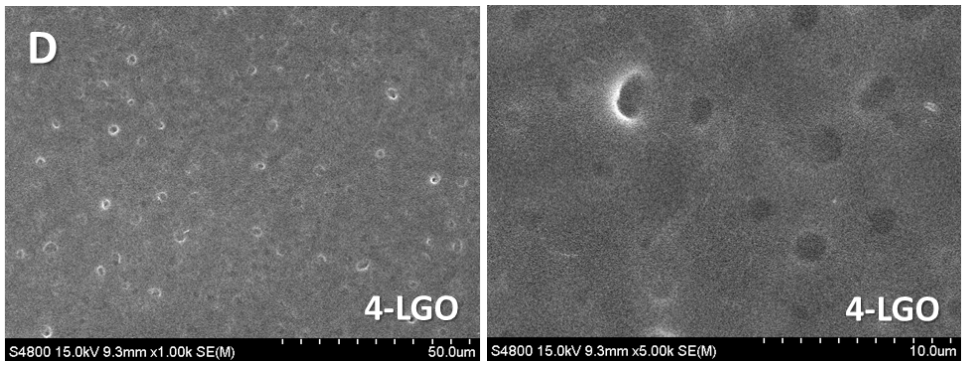

Figure 2-7. Low and high magnification Surface SEM images of (A) 1, (B) 2, (C) 3, and (D) 4 of PVA/LGO bilayers depositions on the surface of 0.22um MF membrane.

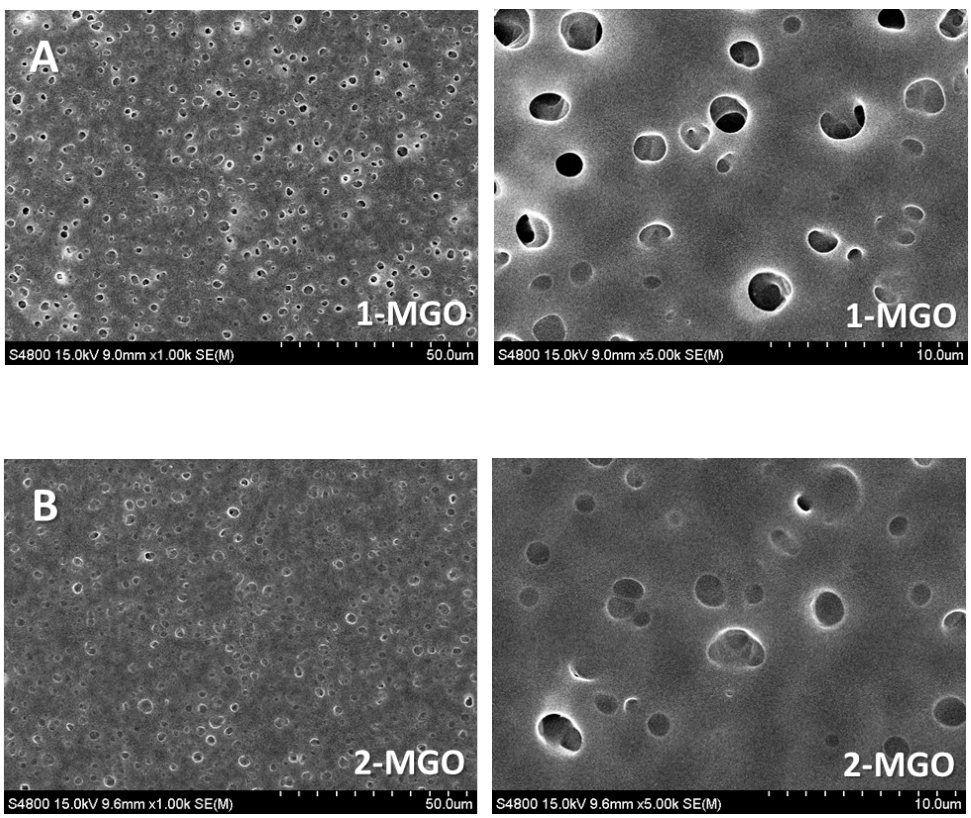

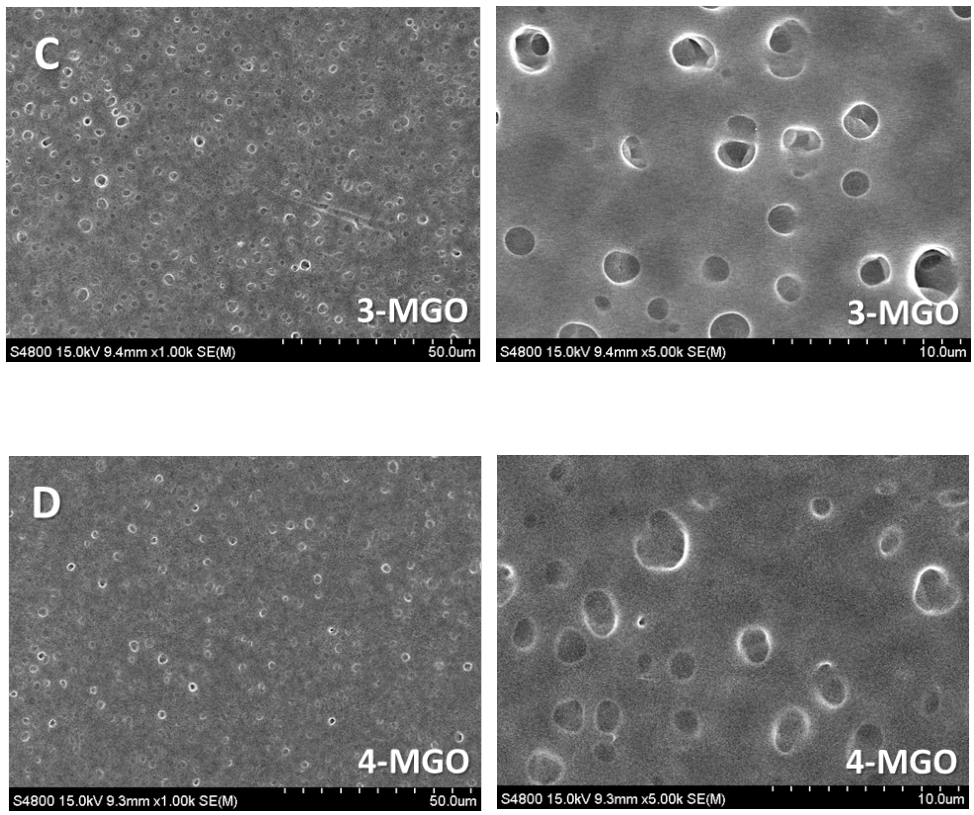

Figure 2-8. Low and high magnification Surface SEM images of (A) 1, (B) 2, (C) 3, and (D) 4 of PVA/MGO bilayers depositions on the surface of 0.22um MF membrane.

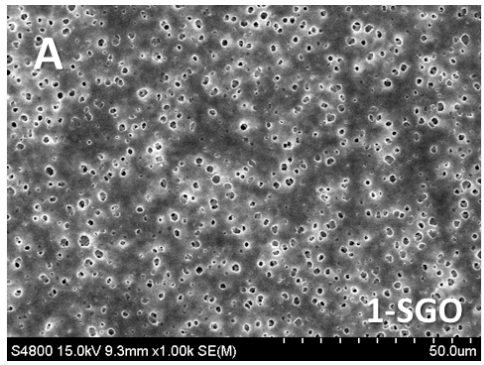
A
1-SGO
S4800 15.0kV 9.3mm x1.00k SE(M)
50.0um

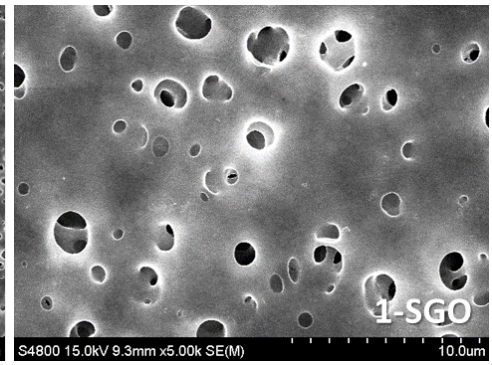
1-SGO
S4800 15.0kV 9.3mm x5.00k SE(M)
10.0um

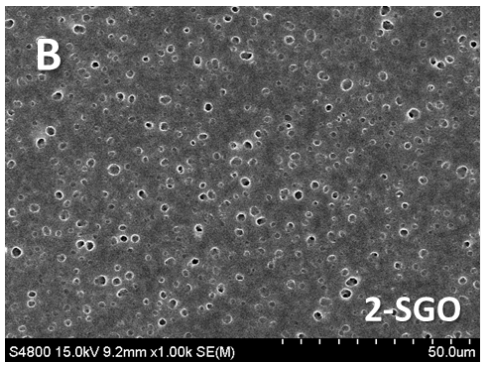
B
2-SGO
S4800 15.0kV 9.2mm x1.00k SE(M)
50.0um

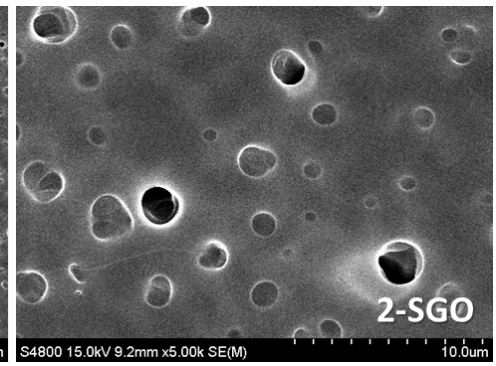
2-SGO
S4800 15.0kV 9.2mm x5.00k SE(M)
10.0um

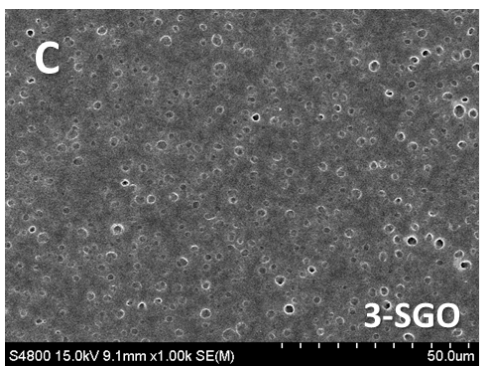
C
3-SGO
S4800 15.0kV 9.1mm x1.00k SE(M)
50.0um

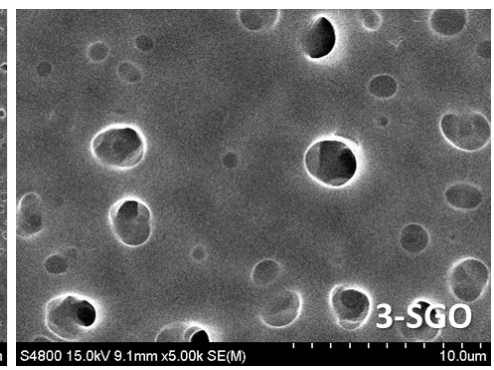
3-SGO
S4800 15.0kV 9.1mm x5.00k SE(M)
10.0um

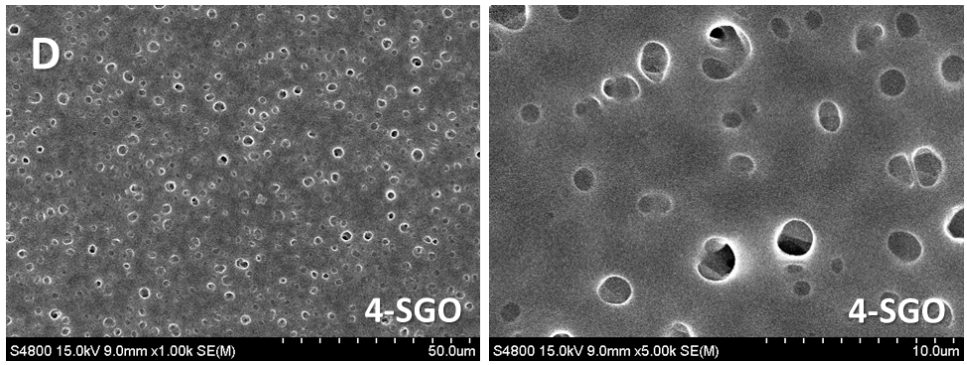

Figure 2-9. Low and high magnification Surface SEM images of (A) 1, (B) 2, (C) 3, and (D) 4 of PVA/SGO bilayers depositions on the surface of 0.22um MF membrane.

After 1- LGO interlayer deposition, most of the pores can be found on the surface of the MF support membrane are the completely uncovered and half covered by GO nanosheet as show in figure 2-10 A and figure 2-7 A. After 1- MGO interlayer deposition, in addition to the remained pores like 1-LGO interlayer deposition, since the size of the MGO nanosheets are similar to the size of the pores of MF support, many structures in which the edge portion of the GO nanosheet is entangled at the edge of the pore, and the middle portion is trapped in the pore were found (figure 2-10 B). In the case of 1-SGO interlayer deposition, since SGO nanosheet is small in size, many graphene seems to enter the inside of the staggered pores without covering the large pores on the outer surface of the MF support as shown in figure 2-10 C and figure 2-9 A. Therefore, after more than three cycles of LBL depositions, both LGO and MGO nanosheets can completely cover all the pores on the surface of the MF support membrane, but many defects can still be found in the membrane surface of SGO.

As the number of GO interlayers deposition increases, the pure water flux of the support membrane decreases significantly, which is mainly due to the large reduction in the pore size of the MF support surface and the resistance of GO nanosheets (Figure 2-11). After 1-4 LGO interlayers deposition, the water permeance of MF support decreased from 8000 to 1017, 490, 65, 31 LMH/bar respectively. and after 1-4 MGO interlayers deposition, the water permeance decreased to 1720, 302, 114, 52LMH/bar respectively. The water permeance of MF support with MGO has an

average of 60-70% higher water permeance than that of MF support with LGO, thanks to smaller GO sizes. First, the layer made of smaller GO nanosheets have a longer total perimeter length, so the number of channels that water molecules can exit is increased. Second, when water molecules reach the surface of GO nanosheets, the distance of water molecules from the edge of GO is also shorter. That means the effective path is also shortened.

The decrease in water permeance caused by the first and second GO interlayers LBL deposition is mainly due to the fact that the pores of the MF support membrane are covered by GO nanosheets, and water molecules cannot directly enter the pores of the surface of the MF support. After the LBL deposition of the last two GO interlayers, the decrease in water permeance is mainly due to that the water molecules can only enter the water transfer channel between the GO nanosheets through the edge or surface defects of GO nanosheets after the pores on the surface of the MF support are all covered. Although water molecules can move rapidly in the hydrophobic region where is no functional group on the surface of GO nanosheets, the resistance of water molecules is increased due to the presence of highly crosslinked portions of PVA and GO nanosheets through glutaraldehyde with covalently bonding. Therefore, when the number of GO layers is simply increased, the water permeance of the membrane does not decrease so fast. Crosslinking inside PVA/GO bilayers is also an important factor affecting the movement of water molecules. Even so, for three cycles LBL deposition of LGO and MGO bilayers, the

water permeance is still higher than the PSF ultrafiltration support layer with an average pore size of 20 nm used in general RO membranes (Figure 2-12). The surface of the PSF ultrafiltration support layer is shown in figure 2-13.

As the deposition increases from 1 to 4 of SGO interlayers, the water permeance of MF support does not decrease exponentially. Even after four depositions, the water permeance can still reach 2300 LMH/bar. This is not only due to the small size of the SGO, but also because it is too small to seal the large pores in the surface of MF support.

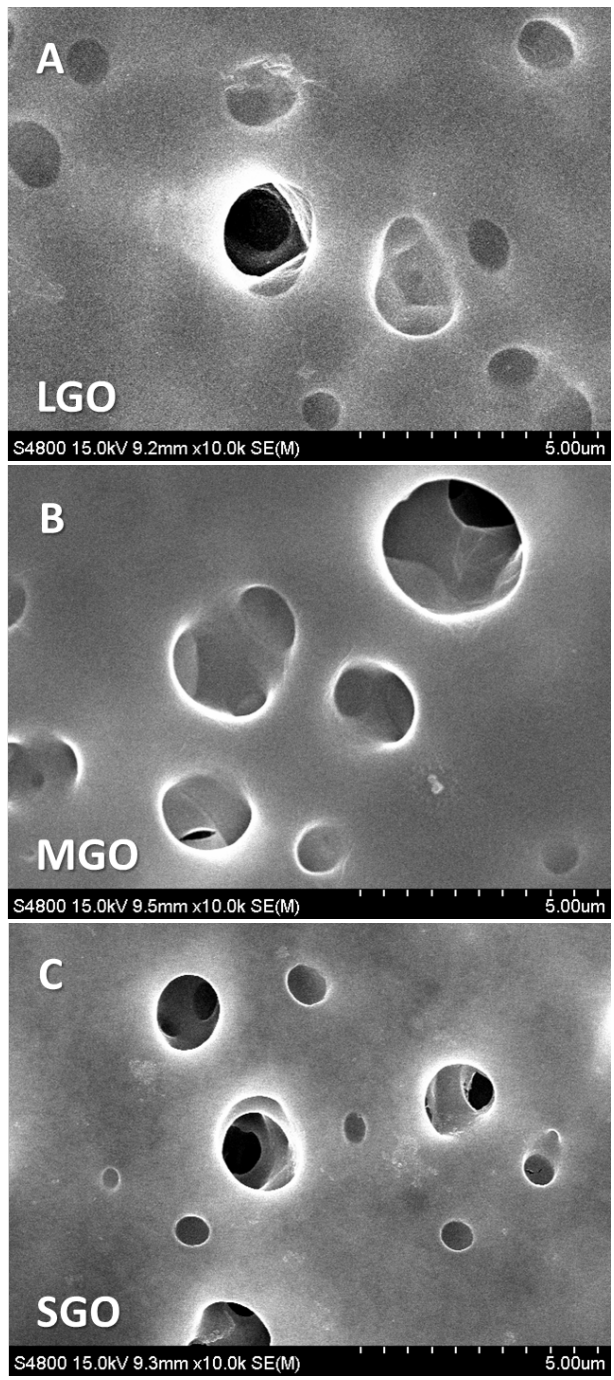

Figure 2-10. Surface SEM images of 1 (A)LGO, (B)MGO, (C)SGO interlayers on the surface of 0.22um MF membrane.

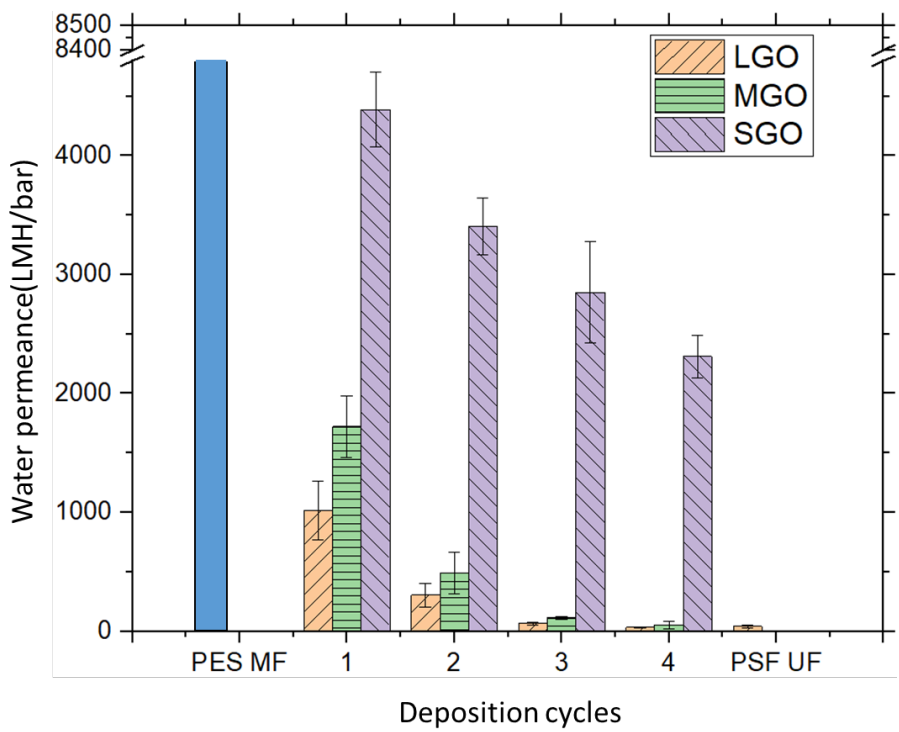

Figure 2-11. Water permeance of MF support membranes with 0-4 GO interlayers deposition and comparison with PSF UF support**.**

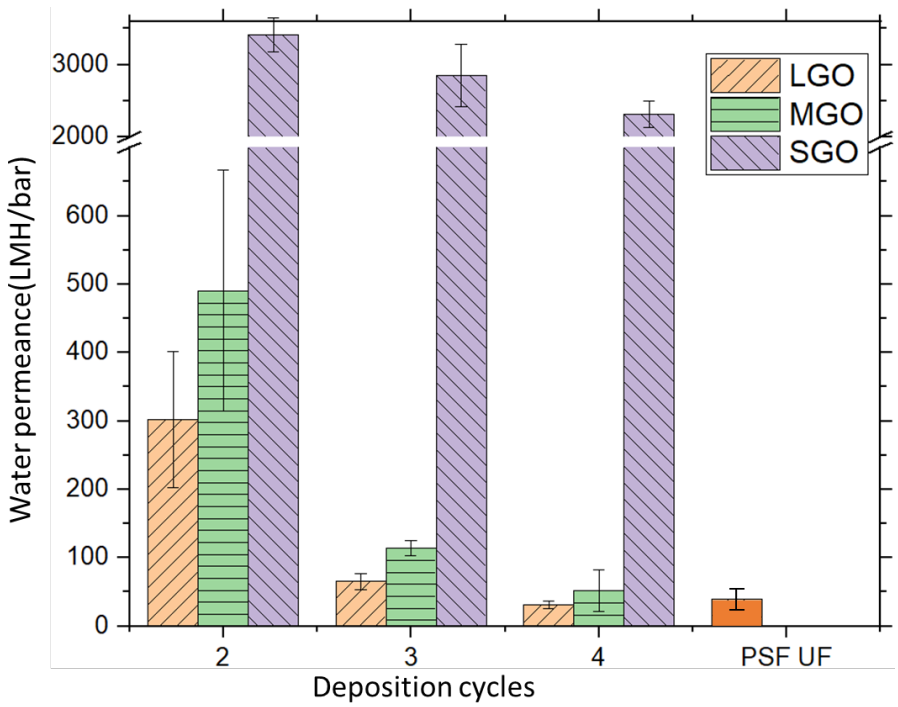

Figure 2-12. Water permeance of MF support membranes with 2-4 GO interlayers deposition and comparison with PSF UF support.

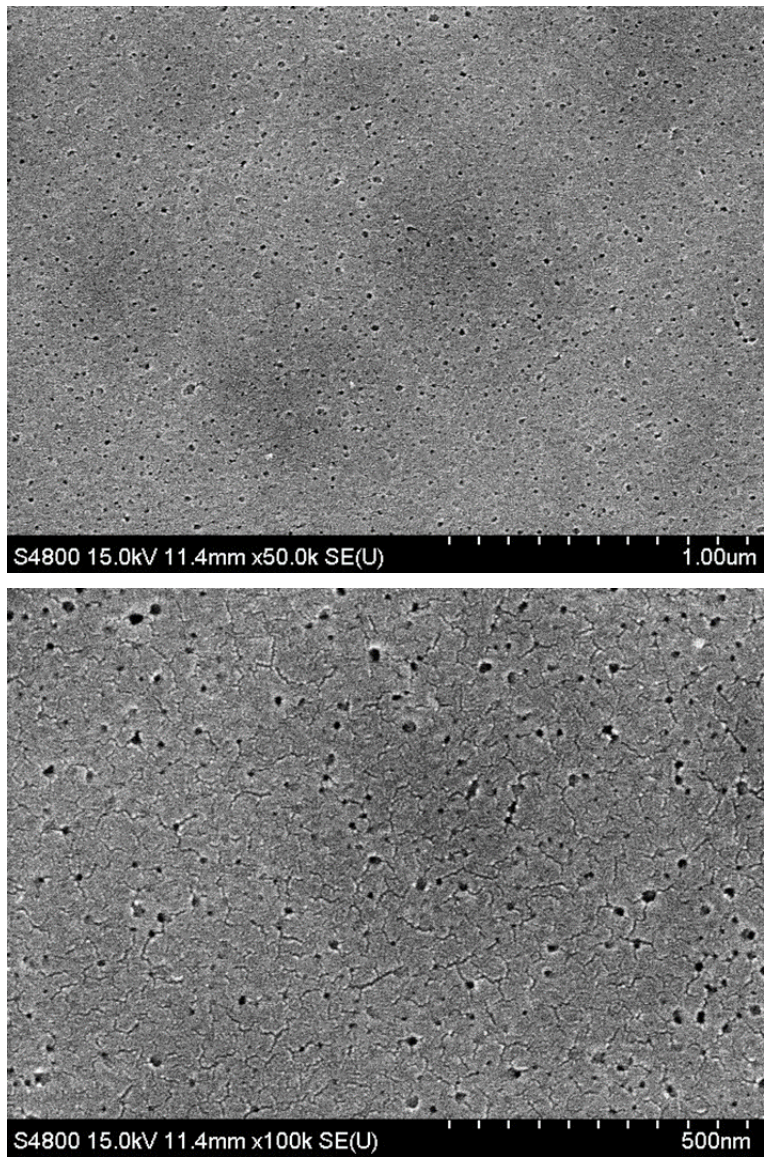

Figure 2-13. Surface SEM images of Polysulfone Ultrafiltration membrane support with 20nm pores

2.3.3 RO Membrane with 0.22um MF support

RO membranes were prepared using the as-prepared 12 types of support layers with different size Graphene oxide nanosheets and bilayers deposition interlayers. We evaluated the desalination performance of these prepared membranes with GO nanosheets interlayers via dead-end filtration. As shown in Figure. 2-14 and Figure. 2-15, with the increase the number GO interlayers deposition, water flux and NaCl rejection decreased and increased, respectively. The RO membrane with only MF support membrane which is without GO interlayer almost had no rejection for NaCl. By observing the surface of RO membrane with only MF support membrane, the PA layer is not formed above the large pores on the surface, and the PA layer appears to be formed above the smaller pores (Figure. 2-16), however, these smaller pores are still relatively large, and the excess influx of MPD solution from these pores to TMC solution and the quick polymerization of PA could not lead to the formation of dense PA layer.

The increase in the NaCl rejection of RO membrane with the increase of the number of GO interlayers is mainly due to two reasons. Firstly, the large pores of the microfiltration membrane are gradually covered, or the pore size is reduced with the increase of GO interlayers deposition, which controls the diffusion rate of the MPD molecules, thereby reducing or eliminating the formation of the low-density PA layer. Secondly, because of the negatively charges and small interlayered spacing between GO nanosheets, MPD molecules were trapped through electrostatic interaction and

molecular size effect. Since the oxygen-containing groups of GO could reacted with the amino group of MPD, the interlayered spacing between GO nanosheets was narrowed[48], thereby leading to the much smaller permeance of GO interlayer interlayers for MPD solution than pure water. As the increase of the numbers of GO interlayer deposition, the reduction in permeance became larger. Because the GO nanosheets provided defined interfaces and reduced the release of MPD molecules, the polymerization could be controlled effectively[49]. This confined interfacial polymerization prevented the protruding of MPD solution from substrates to TMC solution, which would lead to rough membrane surfaces and generally occurred in traditional interfacial polymerization. Moreover, the oxygen-containing groups, which usually caused negatively charges, mostly located at edges and defects of GO sheets. (Figure. 2-17)

the RO membrane with the 3-LGO or 3-MGO interlayers deposition showed acceptable flux of 6.6LMH and 11.8 LMH (Figure. 2-18), and high rejection rates of 95.8% and 97% respectively (Figure. 2-19). Even the LGO or MGO interlayers depositions increase to four, the water fluxes and rejections did not change. The RO membrane with the 3-MGO interlayers deposition has a higher water flux because higher water flux of the support membrane. The higher salt rejection rate is attributed to the more MPD sorption which caused by more oxygen-containing functional groups were carried by MGO than LGO.

The water flux and NaCl rejection of the RO membrane with SGO interlayers decreased and increased respectively with the increase the number of deposition cycles. However, after four deposition cycles, the NaCl rejection was still only 86.3%, although the water flux could reach 22 LMH (Figure. 2-18 and Figure. 2-19). This result is mainly due to the fact that SGO is too small to the pores with diameter much larger than 1 um on the surface of 0.22um MF support membrane relatively, and these pores cannot be effectively covered to reduce the pore size to an appropriate size to control the overflow and diffusion of the MPD from the support membrane.

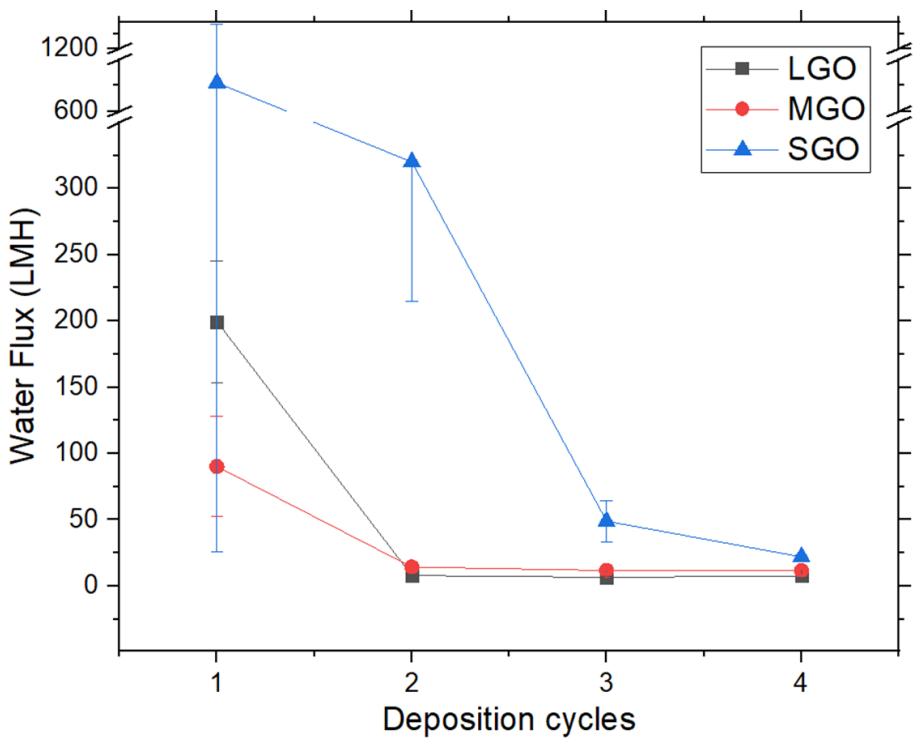

Figure 2-14. Water Flux of the RO membranes. Water flux as a function of number of GO interlayers depositions on 0.22um MF support membrane. The performance of all membranes was tested with 2000 mg/L NaCl aqueous solution and 15.5 bar operating pressure.

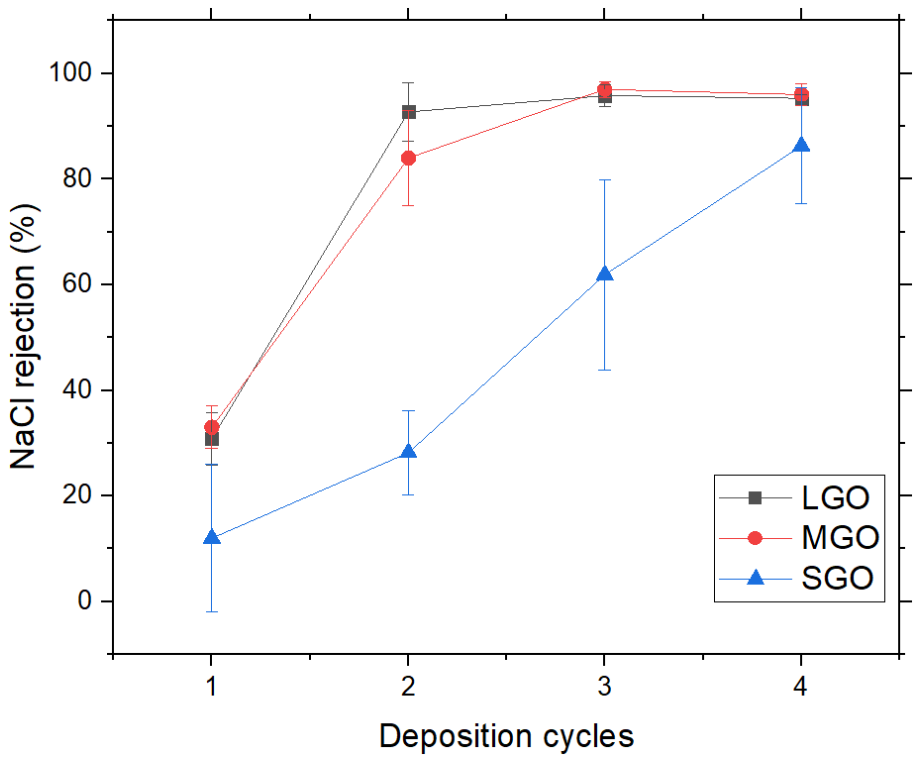

Figure 2-15. NaCl rejection of the RO membranes. Rejection as a function of number of GO interlayers depositions on 0.22um MF support membrane. The performance of all membranes was tested with 2000 mg/L NaCl aqueous solution and 15.5 bar operating pressure.

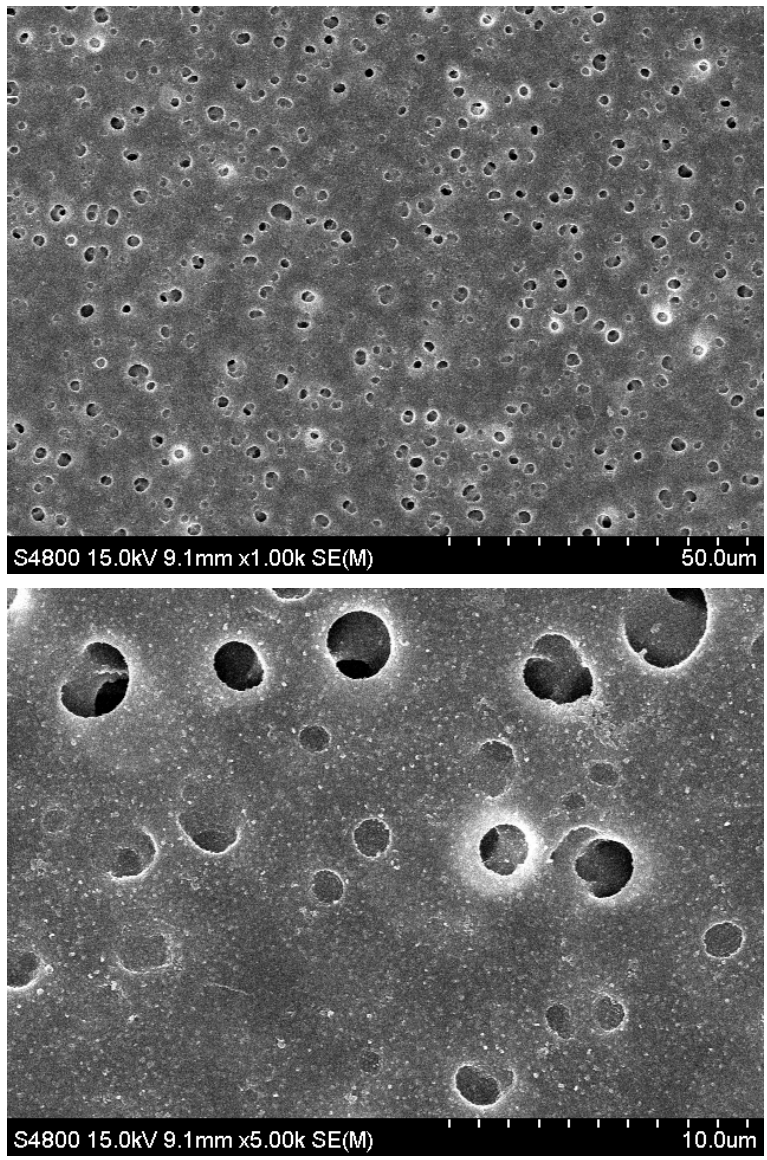

Figure 2-16. Surface SEM images of RO membrane with only MF support membrane

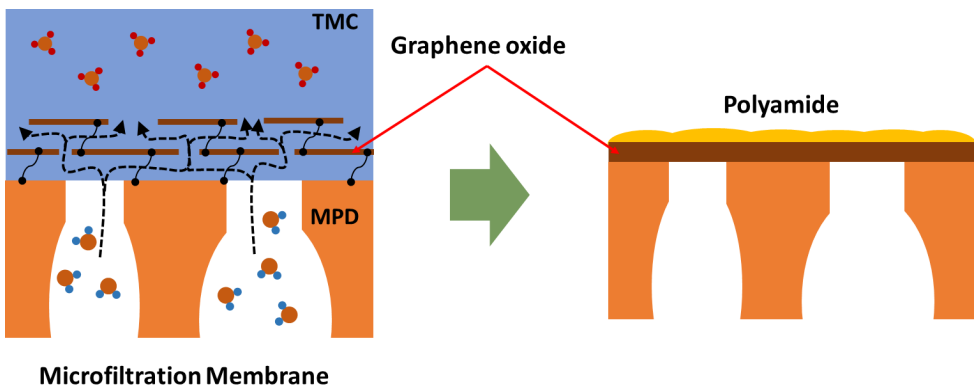

Figure 2-17. Schematic of the process of synthesizing a thin and smooth PA layer on the surface of a microfiltration membrane with PVA/GO bilayers.

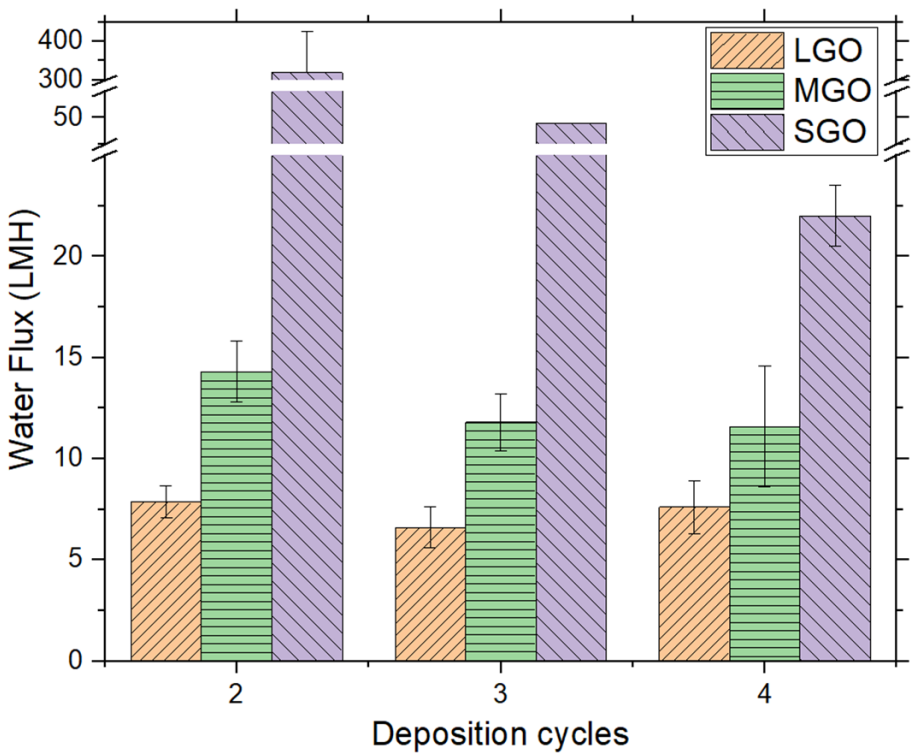

Figure 2-18. Water Flux of the RO membranes with 2, 3, 4 -GO interlayers deposited on 0.22um MF support membrane.

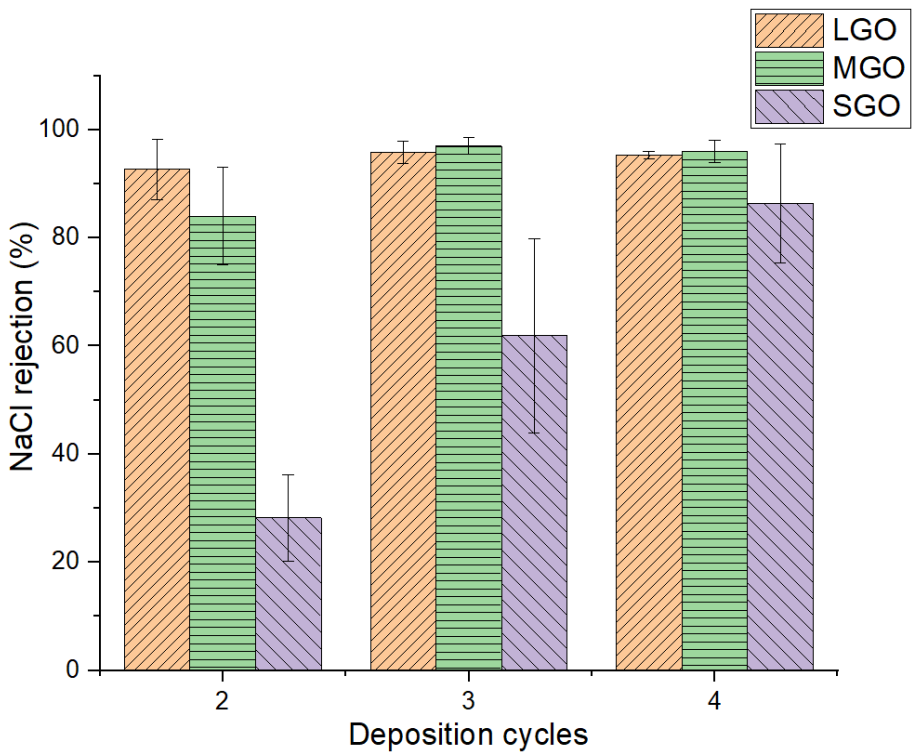

Figure 2-19. NaCl rejection of the RO membranes with 2, 3, 4 -GO interlayers deposited on 0.22um MF support membrane.

Morphologies of the PA layer formed on the 0.22um MF support membrane with GO interlayers deposition were observed by scanning electron microscopy (SEM). Figures 2-20A and Figures 2-21A show that there are many pores on the surface of the PA layer synthesized on the surface of 1-LGO or 1-MGO interlayer deposited MF support due to the PA layer could not be synthesized on the portion of the large pores that was not covered by LGO or MGO. It seems that the pore size of many pores of MF support seems to be reduced to the extent of the ultrafiltration membrane pore size, because in addition to the pores in which no synthetic PA layer can be observed, some ridge and valley structures annular protrusions are also observed. As shown in figure 2-20B and figure 2-21B, since there are no missing pores in the surface after 2-LGO or 2-MGO interlayer deposition on the MF support membrane, no hole defects have been observed after the PA layer was synthesized, and the ridge and valley structures ring protrusions have also been reduced a lot. The ridge and valley structures ring protrusions are not visible at all on the surface of the RO membrane after 3 or 4 -LGO interlayers deposition, but a relatively smooth surface. Since the deposited GO and the surface-synthesized PA layer are thin, the pores of the MF support layer are still clearly identified (figure 2-20 C, D and figure 2-21 C, D). And we found that the ridge and valley structures annular protrusions of the PA layer with MGO interlayers is much less than that with LGO interlayers, which should be caused by the richer oxygen-containing functional groups of MGO that can better control the diffusion of MPD.

Since the SGO is too small to cover the large pores on the surface of the 0.22um MF support layer, many pores that do not synthesize the PA layer can still be seen on the formed PA layer even after 1 or 2 SGO interlayer deposition, which is also the reason for its high water flux and low rejection. (figure 2-22 A, B figure 2-18, and figure 2-19). Since the inside of the large pores is much filled after 3 -SGO interlayer deposition, although the obvious pores are not visible on the synthesized PA layer, the rejection is still only 62%, indicating that there is still insufficient PA crosslinking in the upper part of the large pores. When the PA layer was synthesized on the support layer with 4 -SGO interlayers deposition, the salt rejection rate rose to 86.3%, and ridge and valley structures protrusions began to appear on the surface of RO membrane. This is somewhat similar to the RO membrane with the support layer of only one deposition of LGO or MGO interlayer, indicating that many large pores were reduced to the extent of the ultrafiltration membrane pore size.

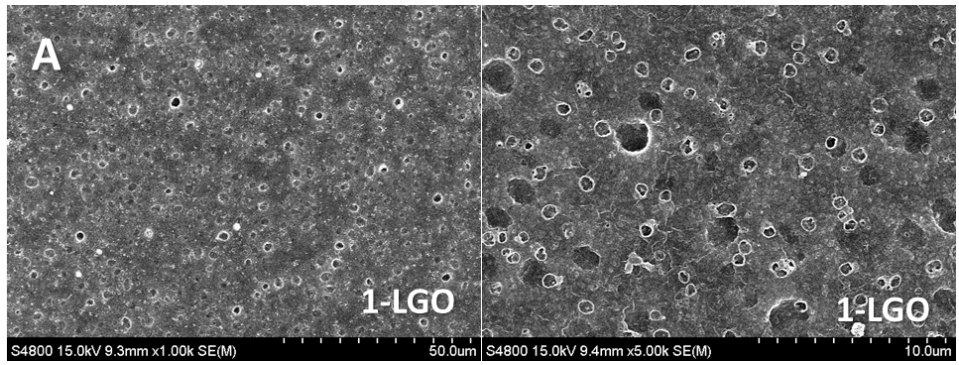
A
1-LGO
S4800 15.0kV 9.3mm x1.00k SE(M)
50.0um
1-LGO
S4800 15.0kV 9.4mm x5.00k SE(M)
10.0um

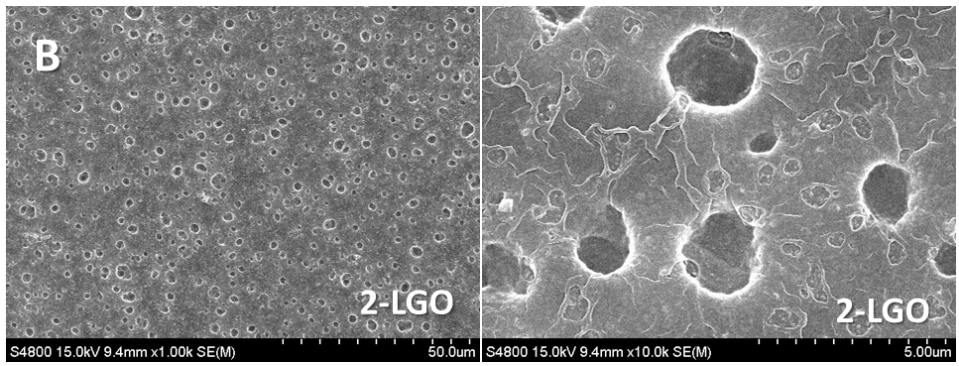
B
2-LGO
S4800 15.0kV 9.4mm x1.00k SE(M)
50.0um
2-LGO
S4800 15.0kV 9.4mm x10.0k SE(M)
5.00um

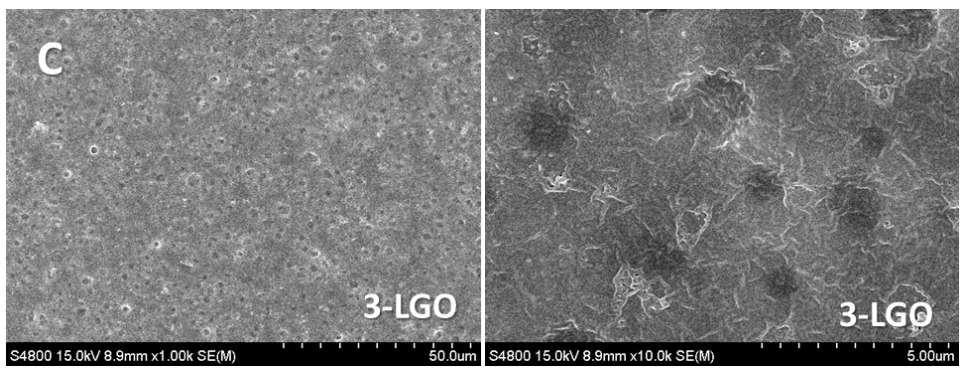
C
3-LGO
S4800 15.0kV 8.9mm x1.00k SE(M)
50.0um
3-LGO
S4800 15.0kV 8.9mm x10.0k SE(M)
5.00um

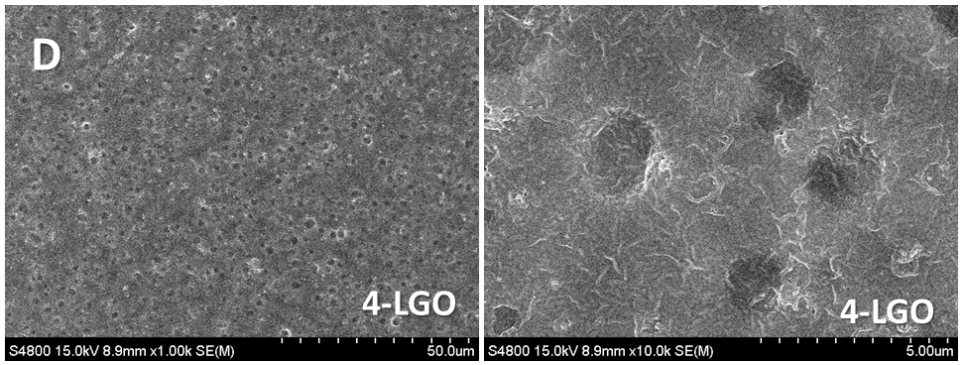

Figure 2-20. Low and high magnification Surface SEM images of RO membrane with 0.22um MF support membrane with(A) 1, (B) 2, (C) 3, and (D) 4 of LGO interlayers depositions

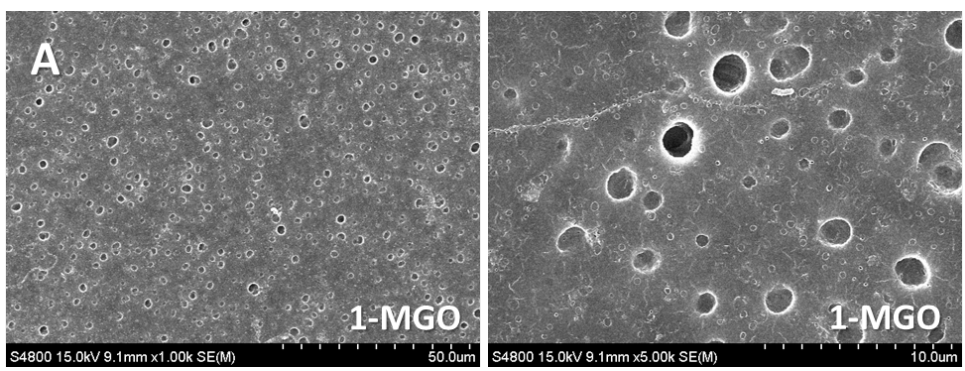

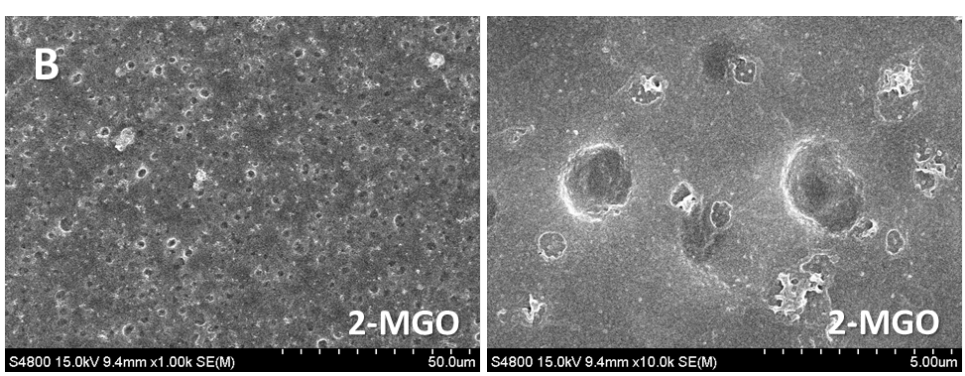

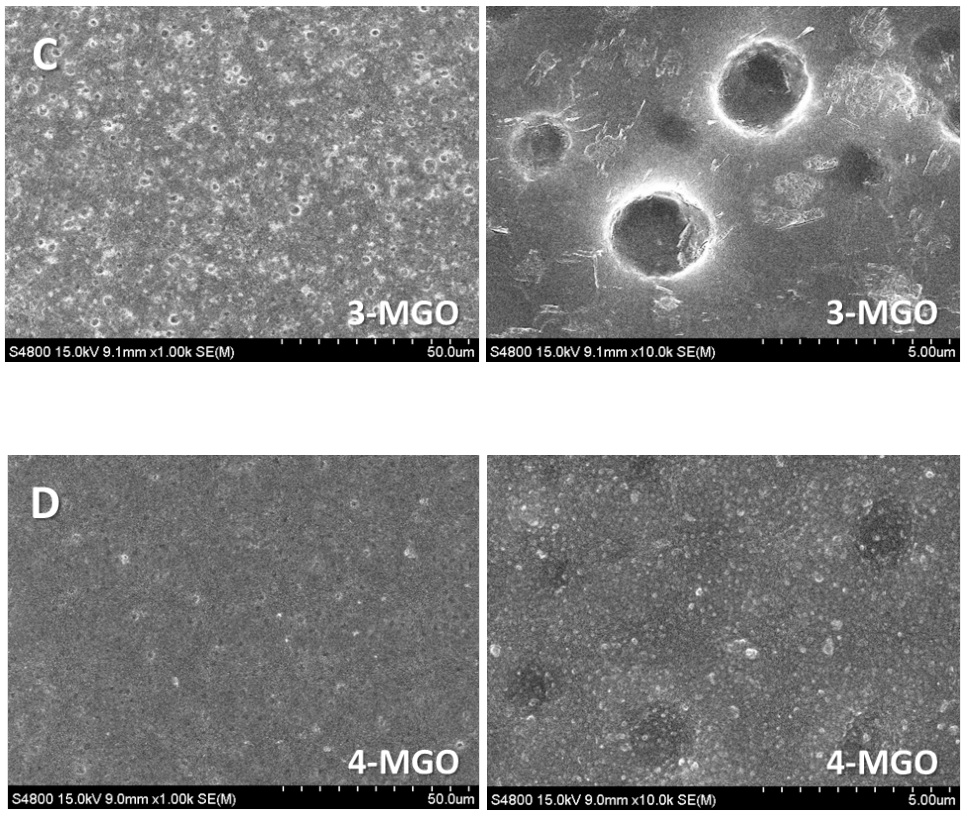

Figure 2-21. Low and high magnification Surface SEM images of RO membrane with 0.22um MF support membrane with(A) 1, (B) 2, (C) 3, and (D) 4 of MGO interlayers depositions

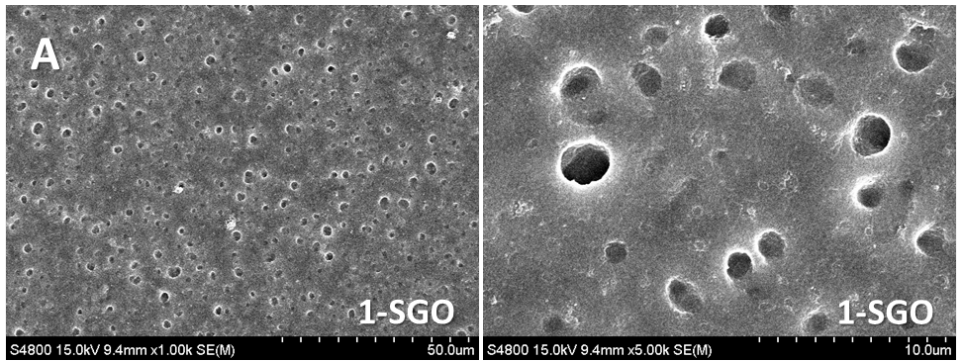
A
1-SGO
S4800 15.0kV 9.4mm x1.00k SE(M)
50.0um
1-SGO
S4800 15.0kV 9.4mm x5.00k SE(M)
10.0um

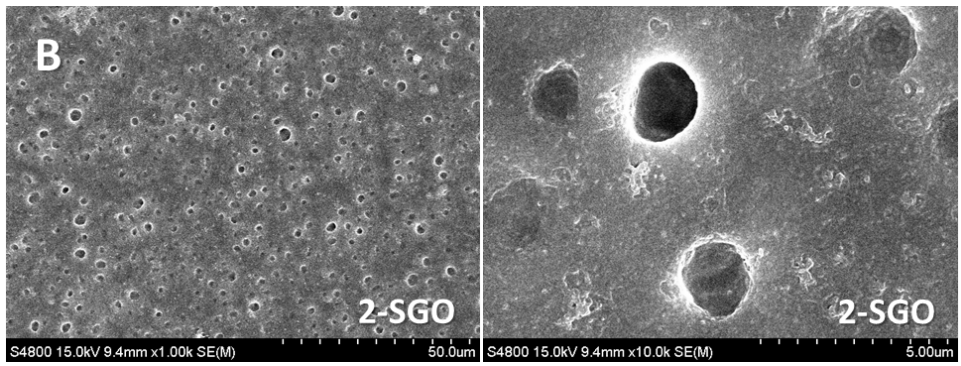
B
2-SGO
S4800 15.0kV 9.4mm x1.00k SE(M)
50.0um
2-SGO
S4800 15.0kV 9.4mm x10.0k SE(M)
5.00um

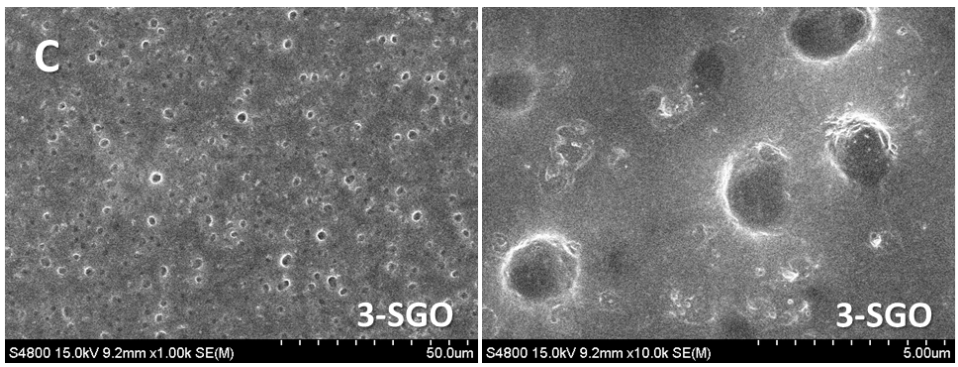
C
3-SGO
S4800 15.0kV 9.2mm x1.00k SE(M)
50.0um
3-SGO
S4800 15.0kV 9.2mm x10.0k SE(M)
5.00um

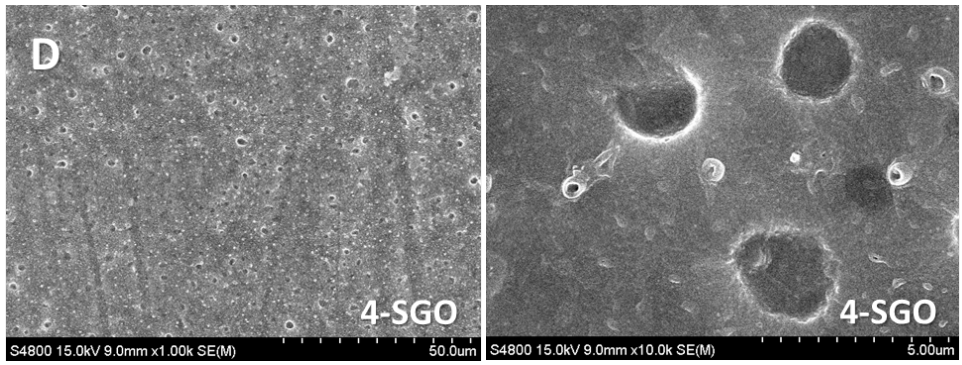

Figure 2-22. Low and high magnification Surface SEM images of RO membrane with 0.22um MF support membrane with(A) 1, (B) 2, (C) 3, and (D) 4 of SGO interlayers depositions

2.3.4 MF Membrane (0.1um) with SGO interlayer

Due to the relatively small size of SGO, it is hard to obtain a RO membrane with a high performance at a low deposition of SGO interlayers on a 0.22 um MF support membrane, a commercial MF membrane product labeled 0.1 microns was used for SGO interlayers as the macroporous support layer. The pore diameter of the membrane surface is distributed between hundred nm to 1um, much smaller than 0.22um MF but the same structure (figure 2-23).

After one of SGO nanosheet interlayer deposition, most of the pores on the surface of the microfiltration membrane have been covered (figure 2-24 A), and the large pores have also greatly reduced the pore size due to the trapping of the SGO nanosheets (figure 2-24 B). No obvious pores were visible on the surface of support after 2-SGO interlayers deposition. After the next three or four cycle depositions, it seems that only the thickness of the deposited SGO interlayer is increasing because the pores of the MF support gradually becomes blurred (figure 2-24 C, D).

The water flux of 0.1um MF is 2300LMH/bar. After 1-4 of SGO interlayers deposition, the water permeance of the support drops to 882, 301, 94, 58 LMH/bar respectively, which are all higher than the PSF ultrafiltration support of 40 LMH/bar (figure 2-25).

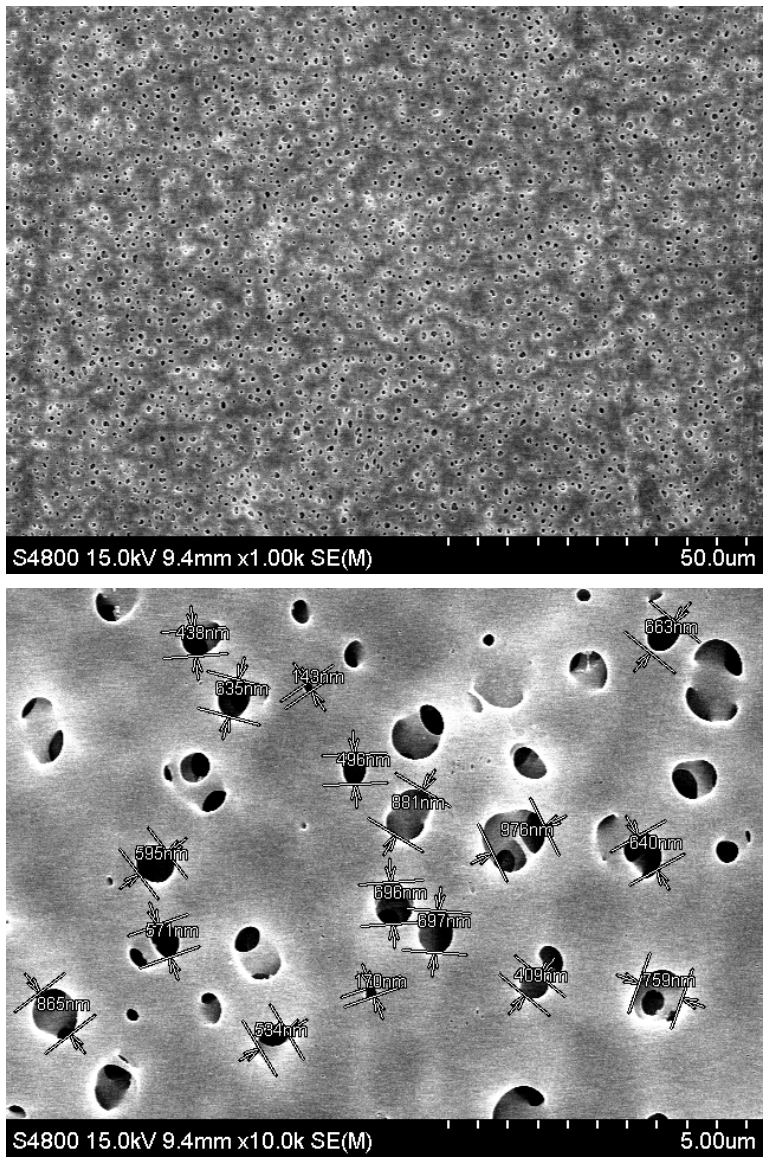

Figure 2-23. Low magnification and high magnification Surface SEM images of commercial microfiltration membrane (0.1um)

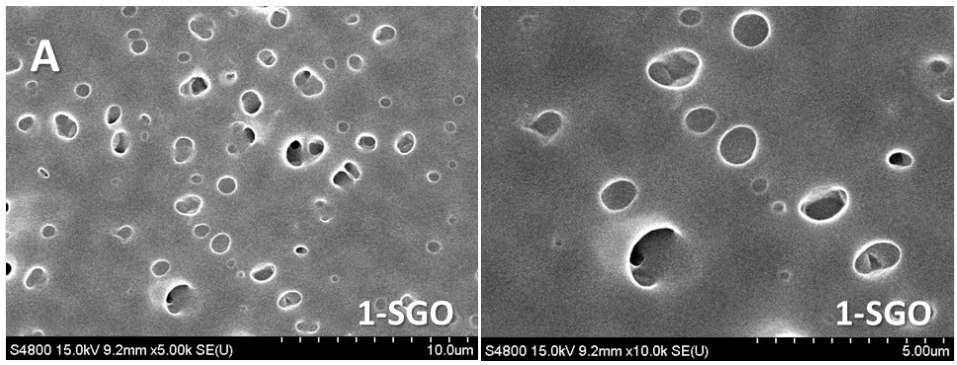
A
1-SGO
S4800 15.0kV 9.2mm x5.00k SE(U)
10.0um
1-SGO
S4800 15.0kV 9.2mm x10.0k SE(U)
5.00um

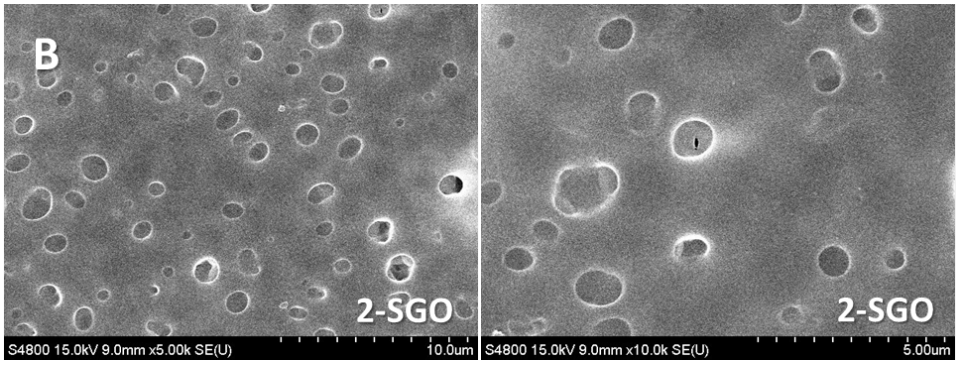
B
2-SGO
S4800 15.0kV 9.0mm x5.00k SE(U)
10.0um
2-SGO
S4800 15.0kV 9.0mm x10.0k SE(U)
5.00um

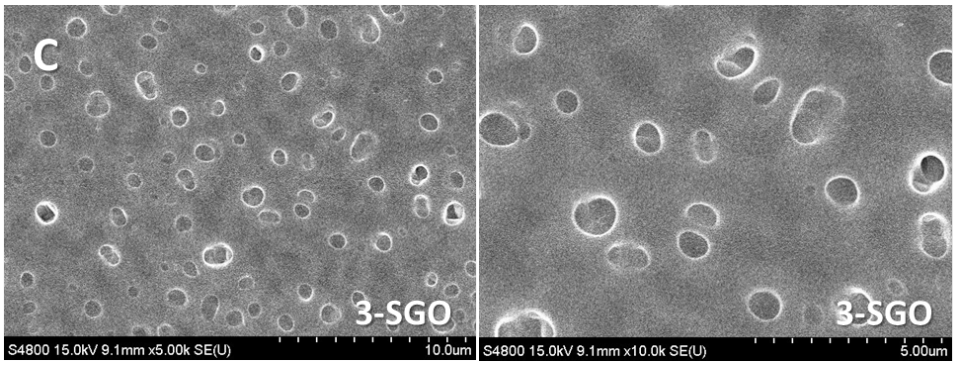
C
3-SGO
S4800 15.0kV 9.1mm x5.00k SE(U)
10.0um
3-SGO
S4800 15.0kV 9.1mm x10.0k SE(U)
5.00um

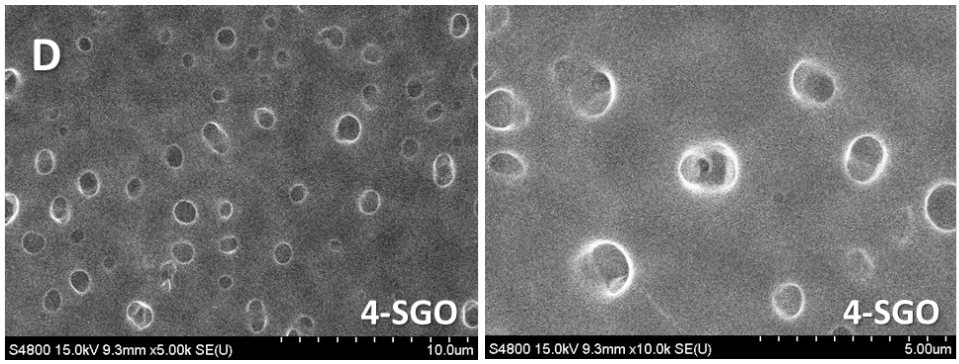

Figure 2-24. Low and high magnification Surface SEM images of (A) 1, (B) 2, (C) 3, and (D) 4 of SGO interlayers depositions on the surface of 0.1um MF membrane.

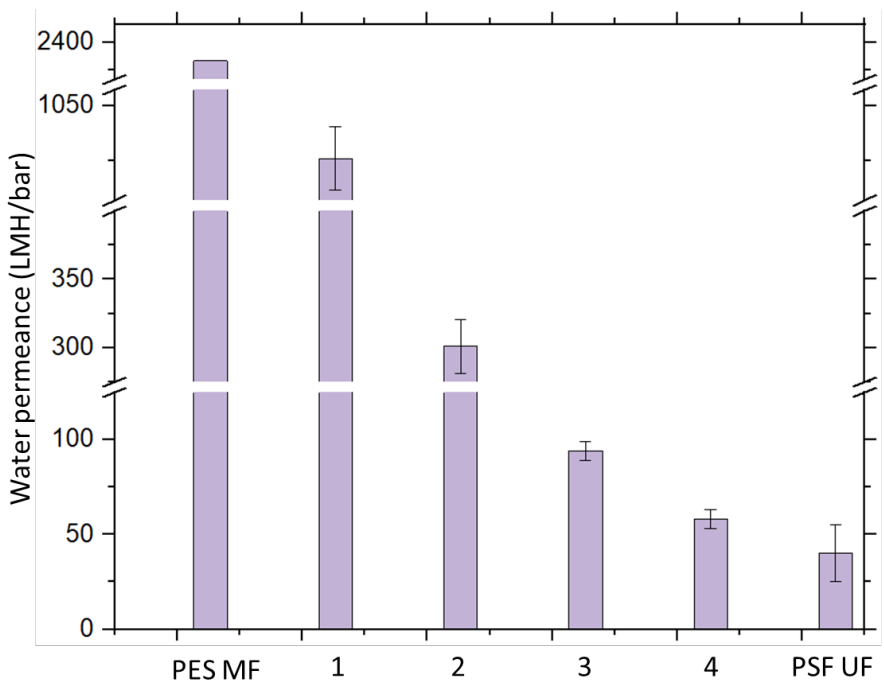

Figure 2-25. Water permeance of MF support membranes with 0-4 -SGO interlayers deposition and comparison with PSF UF support.

2.3.5 RO Membrane with 0.1um MF support

The RO membrane using SGO interlayer and 0.1um MF exhibited a excellent performance. Even if the rejection of RO membrane with one of SGO interlayer deposition has reached more than 90%, this indicates that SGO has a high coverage efficiency for the pore size which similar to its size, and the surface pore size can be reduced to the pore size range of the ultrafiltration membrane after only one cycle of deposition. As well as the RO membrane with MF support of 2-SGO interlayer deposition exhibited large water flux of 22 LMH and good rejection of 97.3% (figure 2-26). Subsequent SGO interlayer depositions only reduces the water permeance of the support layer, so the flux of their RO membrane is also slightly reduced.

However, the ridge and valley structure protrusions of the RO membrane with SGO interlayers are more than the RO membranes with LGO or MGO interlayers, which is attributed to the oxygen-containing functional groups of SGO are relatively less than LGO and MGO, and thus it is more difficult to control the diffusion of the MPD molecules (figure 2-27 and table 2-1).

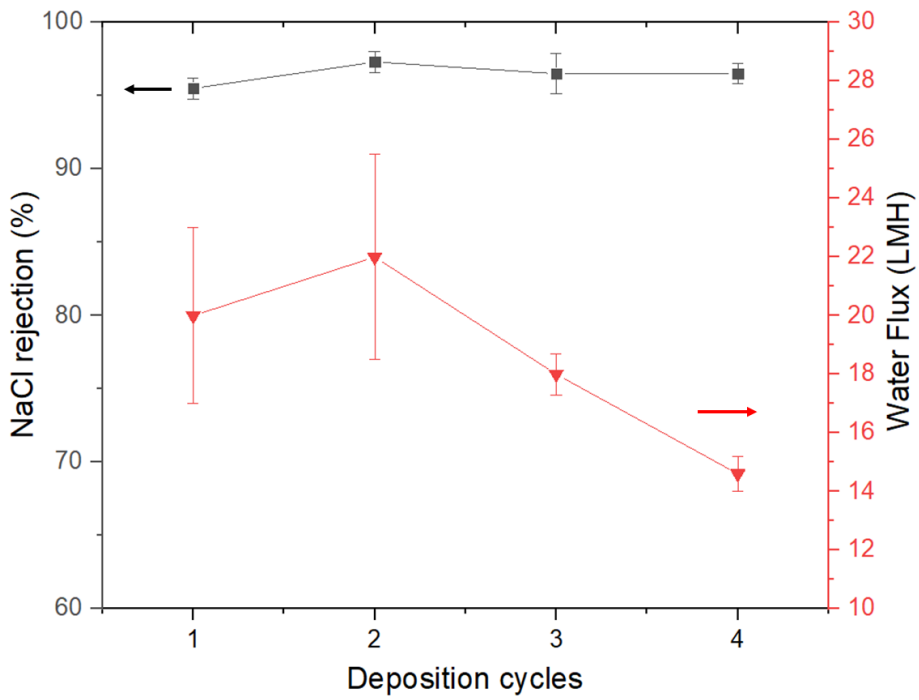

Figure 2-26. Performance of the RO membrane. (a) Water flux and NaCl rejection as a function of number of SGO interlayers depositions cycles on 0.1um MF support membrane. The performance of all membranes was tested with 2000 mg/L NaCl aqueous solution and 15.5 bar operating pressure.

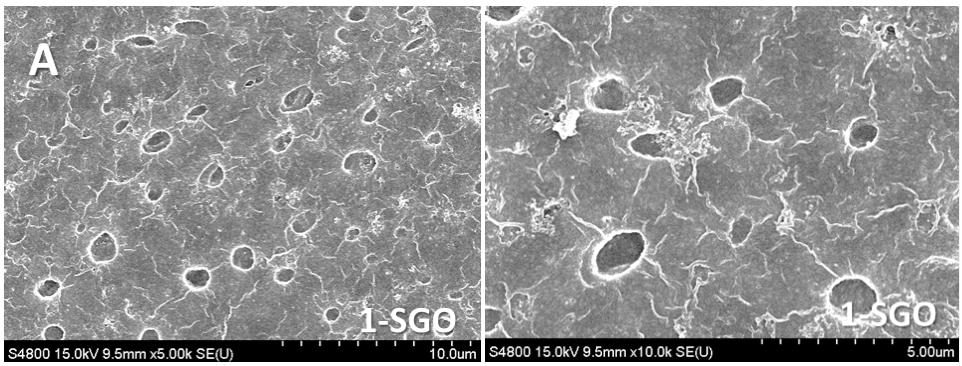
A
1-SGO
S4800 15.0kV 9.5mm x5.00k SE(U)
10.0um
1-SGO
S4800 15.0kV 9.5mm x10.0k SE(U)
5.00um

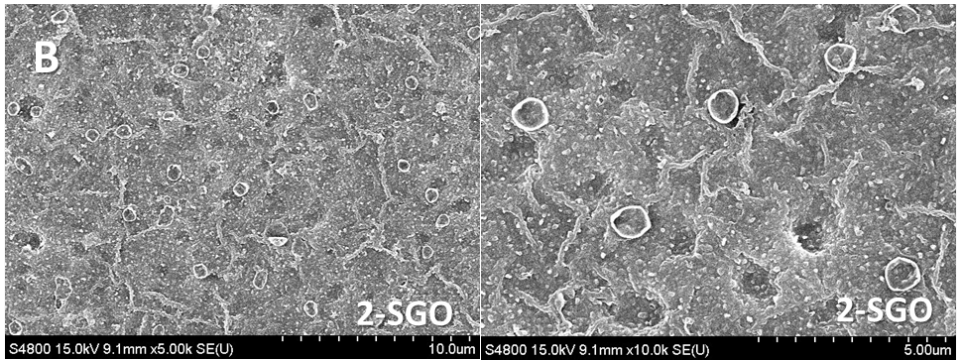
B
2-SGO
S4800 15.0kV 9.1mm x5.00k SE(U)
10.0um
2-SGO
S4800 15.0kV 9.1mm x10.0k SE(U)
5.00um

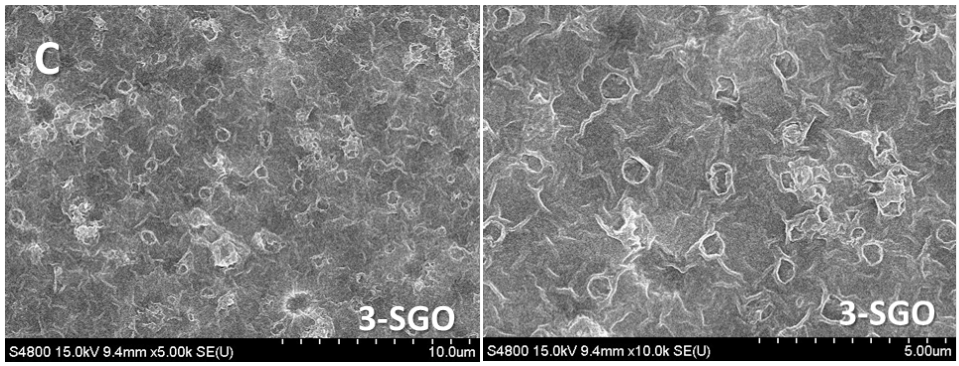
C
3-SGO
S4800 15.0kV 9.4mm x5.00k SE(U)
10.0um
3-SGO
S4800 15.0kV 9.4mm x10.0k SE(U)
5.00um

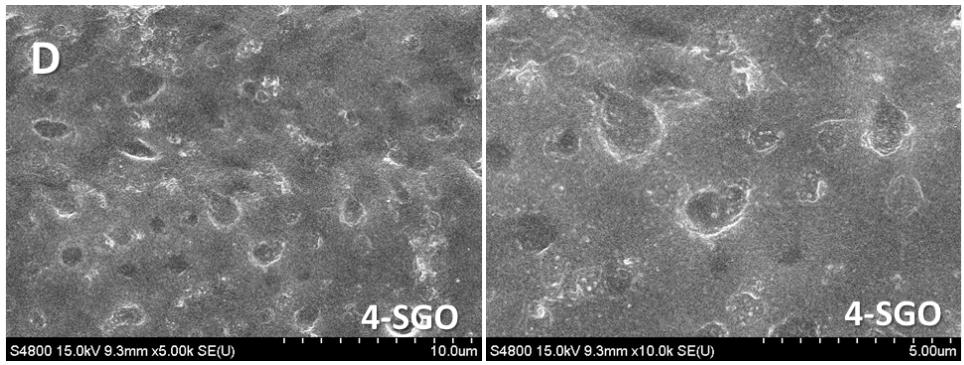

Figure 2-27. Low and high magnification Surface SEM images of RO membrane with 0.1um MF support membrane with(A) 1, (B) 2, (C) 3, and (D) 4 of SGO interlayers depositions

2.4. Conclusion

The performance comparison of RO membranes with MF support layer and 3 - LGO, 3-MGO, 2-SGO interlayers which are with optimal salt rejection, and for comparison with the traditional RO membrane structure which with an ultrafiltration support layer are shown in figure 2-28. a PSF membrane made by 14wt% PSF/NMP solution was employed to fabricate the PA/PSF traditional RO membrane by traditional interfacial polymerization. The prepared PA/PSF membrane had water flux of 14LMH and rejection of 96% was shown in figure 2-28. For LGO, MGO or SGO, the thickness difference of the PA layer synthesized on the surface can be ignored, therefor, the RO membrane with 2-SGO interlayer and 0.1um MF support with the highest rejection and flux at 15.5 bar, RO membrane with 3-MGO interlayer and 0.22um MF support has a similar flux as the conventional PA/PSF RO membrane, but a higher rejection. Through this study, we understand the performance mechanism of water treatment membranes when using GO nanosheets as interlayer on the macroporous support layer structure. The size of GO nanosheets is inversely proportional to the water flux (longer or shorter effective path), and more importantly, small-sized GO nanosheets have an MF support layer with a suitable pore size which could be matched with the size of GO nanosheets, to achieve optimized performance. The smaller the size of GO nanosheet is best matched to the MF support layer which with its similar size pore size.

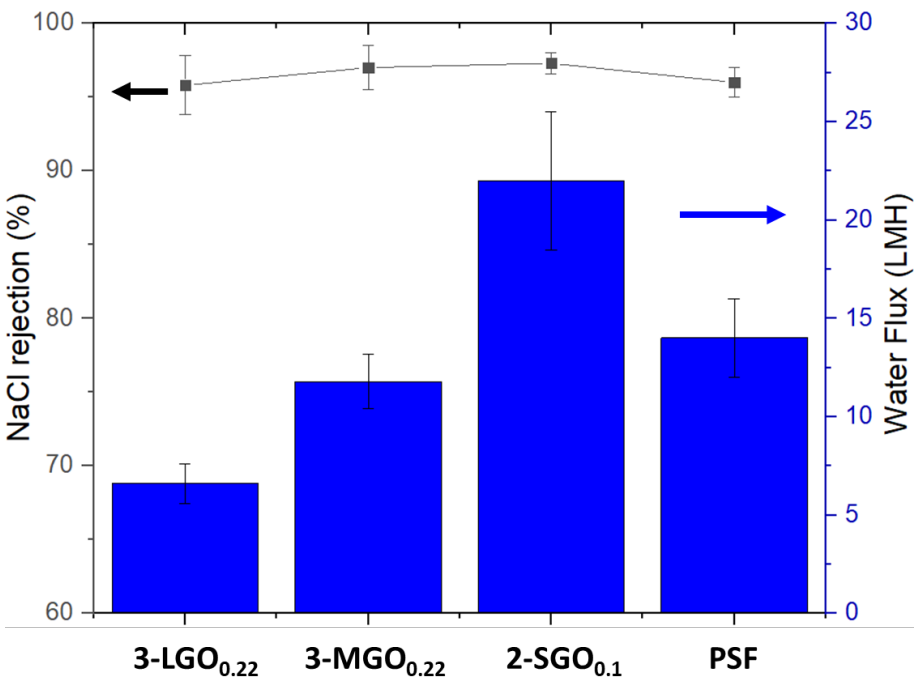

Figure 2-28. Performance comparison of RO membranes with 3-LGO, 3-MGO, 2-SGO interlayer and used MF support layer, and RO membranes with PSF ultrafiltration support layer

Chapter 3.
Reverse Osmosis Membrane with Carbon Nanotube Support Layer

3.1 Introduction

Traditional reverse osmosis (RO) membranes, which is a thin film composite (TFC) consisting of a highly cross-linked polyamide (PA) layer on the surface of a porous supporting layer, still have a low water flux due to the thickness and roughness of the PA layer, and the resistance of the support layer. Despite recent progresses, the water flux attainable at the desired rejection level is relatively low and a challenge is still out there for the development of a RO membrane that can deliver a high throughput.

Carbon nanotubes (CNTs), which have drawn much attention in recent decades as an additive, have been utilized in many studies. CNTs dispersed in the selective layer[37, 50-57] and/or support layers[35, 58-61] are mainly used to enhance the water permeability(CNT mixed membranes), exploiting the unique hydrophobic surface properties of carbon nanomaterials.[62, 63] However, the CNTs could not function well for high water permeability in the mixed matrices due to disordered orientation and a small amount of CNTs present.[64] In our previous research, we reported a millimeter-thick CNT membrane for the ultrafiltration that can provide a water permeability that is of the order of 10^4 L m^{-2} h^{-1} bar^{-1}. The developed membrane

consists only of vertically aligned carbon nanotube walls that provide 6 nm wide inner pores and 7 nm wide outer pores formed between the walls of the carbon nanotubes (outer-wall vertically aligned CNT membrane) [39] when the carbon nanotube forest is densified by a simple mechanical densification method[65]. The structural characteristics of the outer wall membranes, such as their pore dimensions, pore density, and tortuosity were varied with the mechanical densification. The experimental results revealed that the permeance increases rather than decreases as usually observed, as the pore size decreases.

We report in this work the synthesis of polyamide layer on top surface of the high flux outer-wall CNT membrane via interfacial polymerization of m-phenylenediamine (MPD) and trimesoylchloride (TMC). This densified vertically aligned carbon nanotube (outer-wall VACNTs) membrane essentially replaces the traditional polymer-based support membrane such as polysulfone membrane as show in Figure 3-1.

Due to the ultrahigh porosity and hydrophobic nature of the outer-wall VACNTs, the composite membrane of polyamide/outer-wall VACNTs (PA/outer-wall VACNTs) exhibits an outstanding performance for desalination with a permeating flux of 128.6 LMH and 98.3% rejection of NaCl ions at 15.5bar. The performance of the PA/outer-wall VACNTs, in particular in water permeability, is much higher than that for the conventional RO membranes with polysulfone support layer and

CNT mixed membranes(usually 0.4 – 3 LMH·bar^{-1})[36] and the permeability is the highest flux reported so far for the same rejection level.

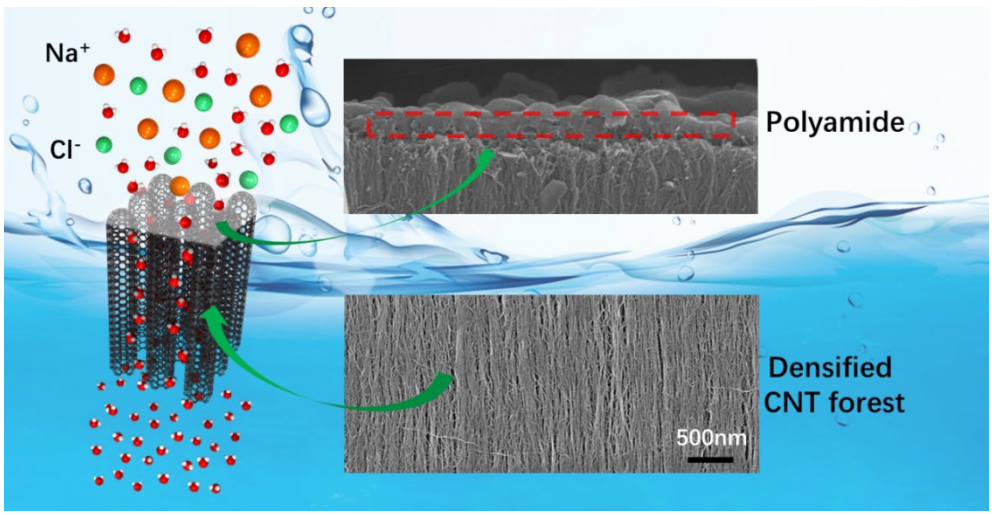

Figure 3-1. Reverse Osmosis Membrane with Carbon Nanotube Support Layer

3.2 Experimental Section

3.2.1 Materials:

M-phenylenediamine (MPD, MW:108.14) and trimesoyl chloride (TMC, MW:265.48) were purchased from Sigma-Aldrich and used as received. ISOL-C solvent was obtained from SK Global Chemical Co., Ltd. Deionized(DI) water was prepared in a Purelab option-Q purification system. Triethylamine (TEA, MW:101.19) and Dimethyl sulfoxide (DMSO, MW:78.14) were used as purchased from Junsei chemical Co., Ltd. Camphor sulfonic acid (CSA, MW:232.30) was purchased from Alfa Aesar.

3.2.2 Preparation of outer-wall VACNTs support membrane:

Carbon nanotube forest was densified to one tenth of the original area occupied by as-grown CNTs by mechanical densification as we reported earlier (Figure 3-2).[39, 66] The structural characteristics of the outer wall membranes, such as their pore dimensions, pore density, and CNT diameter were reported in our previous work. The CNT diameter and spacing (=pore dimensions of the outer wall membrane) and density (=pore density of the outer wall membrane) are summarized in Table 3-1. Pore diameter was estimated using the pore-flow solute model with dextran. Pore density was estimated through the area density estimation of outer-wall VACNTs.[39] The CNT inner and outer diameters were obtained from high-resolution tunneling electron microscopy (HR-TEM) measurements of 100 individual CNTs. The outer-wall VACNTs array was surrounded by gel-like highly viscous epoxy and cured for 24 hours at room temperature to grip the CNT array under high test pressure and to block the leaking of testing fluids from the sides of the CNT array. The resulting membrane was mounted on a PET film with a rectangular hole (1 cm x 1 cm) for further performance testing. (Figure 3-3)

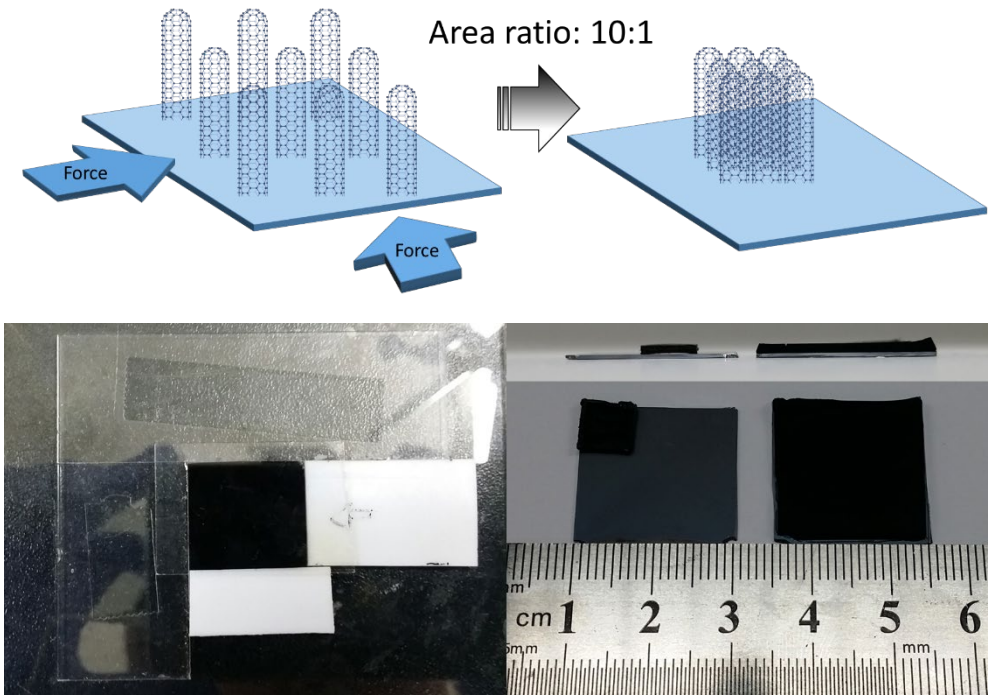

Figure 3-2. Schematics for mechanical densification of the CNT array. All sides of the CNT array are evenly pressed to reduce it to the desired area.

Table 3-1.

Details of as grown VA CNT array and outer-wall membrane. Note that outer-wall CNT membrane was used as support layer in this work.

Samples	Pore diameter (nm)	Pore density (10^{10} # cm^{-2})	CNT inner diameter (nm)	CNT outer diameter (nm)
As grown VA CNT array (before densification)	37.8±0.7	8.14±0.2	4.8	7.1
Outer-wall CNT membrane (after densification)	6.9±0.1	83.3±2.5		

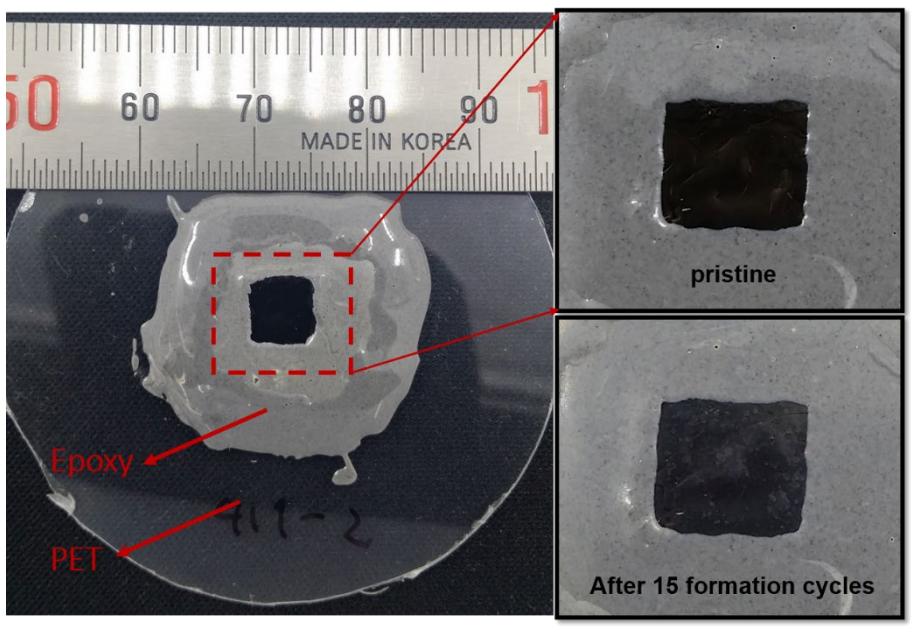

Figure 3-3. Photograph of a PET film supported outer-wall VACNTs membrane.

3.2.3 Fabrication of the polyamide/outer-wall VACNTs membrane:

Polyamide /densified VACNTs (PA/outer-wall VACNTs) membranes were prepared by creating polyamide (PA) selective layer on the outer-wall VACNTs support membrane via traditional interfacial polymerization (IP) reaction and repeated deposition.

The first cycle starts with immersing the outer-wall VACNTs membrane into MPD aqueous solution under vacuum (-1 bar). The outer-wall pores (interstitial space between the CNTs) of the CNTs were subsequently filled with MPD aqueous solution. Afterward, excess MPD aqueous solution was removed from the membrane top surface using rubber air blower. Then, the MPD saturated outer-wall VACNTs membrane was soaked in 0.15wt% TMC ISOL-C solution for 2minutes and subsequently rinsed with pure ISOL-C solvent, which completes the first PA deposition cycle. The subsequent deposition cycles consisted of immersing the membrane into MPD aqueous solution under ambient pressure for 2mins and subsequently rinsing it with DI water to eliminate the unreacted MPD. Accordingly, the membrane was dipped into TMC (0.15 wt%) ISOL-C solution for 2mins and then rinsed in pure ISOL-C solvent. A thin polyamide layer was deposited on the top surface of outer-wall VACNTs membrane by this repetitive deposition of MPD and TMC monomers. Figure 3-3 shows the top surface of outer-wall VACNTs membrane before and after 15 formation cycles of PA selective layer.

3.2.4 Modified MPD aqueous solution

The modified MPD aqueous solution was prepared according to Lee's method.[27] Briefly 2wt% triethylamine(TEA), 4wt% camphor sulfonic acid (CSA), and 1.5wt% dimethyl sulfoxide (DMSO) as additives were added to a 2wt% MPD aqueous solution. Then a homogenous modified MPD aqueous solution was obtained after 15mins of stirring at room temperature.

3.2.5 Characterization of PA/VACNTs membranes

Scanning electron microscopy (SEM) analysis was performed using a Hitachi S-4800 field-emission electron microscope at an acceleration voltage of 10-15KeV. Fourier transform infrared spectroscopy (FT-IR) spectra were measured by a FT-IR spectrometer (Thermo Scientific, Nicolet 6700).

3.2.6 Membrane Performance Tests:

Membrane performance was tested using a dead-end system with an effective square area of approximately 0.2 cm^2 and a 2000 mg/L NaCl aqueous solution as the feed. The operating pressure was 15.5 bar. Water flux (J) was determined from the aggregate sum of the gathered permeate (V) during a specified period of time (t), i.e., J ($Lm^{-2} h^{-1}$) = V/At, where A is the area of the top surface of outer-wall VACNTs. Salt concentrations of the permeate (C_p) and feed(C_f) were estimated with a conductivity meter (Seven Compact, conductivity S230), and salt rejection(R) was calculated by the the equation: R (%)= $(1-C_p/C_f) * 100$.

For each set of result, at least three independent samples were tested for reliability. Each sample was tested for at least 12 hours to ensure the stability of water flux and salt rejection.

3.3 Results and discussion

3.3.1 Standard PA/outer-wall VACNTs

Formation of the first PA layer on top surface of outer-wall VACNTs support membrane is schematically illustrated in Figure 3-4a. The first cycle starts with immersing the outer-wall VACNTs membrane into an MPD aqueous solution under vacuum (-1 bar) to fill the outer-wall pores (interstitial space between CNTs) of the CNTs with the MPD solution. Excessive surface MPD solution was removed from the top surface of outer-wall VACNTs by rubber air blower. Then, the MPD saturated outer-wall VACNTs membrane was soaked in 0.15 wt% TMC dissolved in isoparaffin solution (ISOL-C^{TM}, SK Global Chemical Co., Ltd, South Korea) for the traditional interfacial polymerization and subsequently rinsed with pure isoparaffin solution, which completes the first PA formation cycle. Subsequent PA formation cycle involved exposing the PA layer to MPD solution followed by exposure to TMC solution. The concentrations were those commonly used for MPD and TMC which are 3 wt% and 0.15 wt% respectively.[31]

Details about the membrane fabrication are given in the materials and methods section.

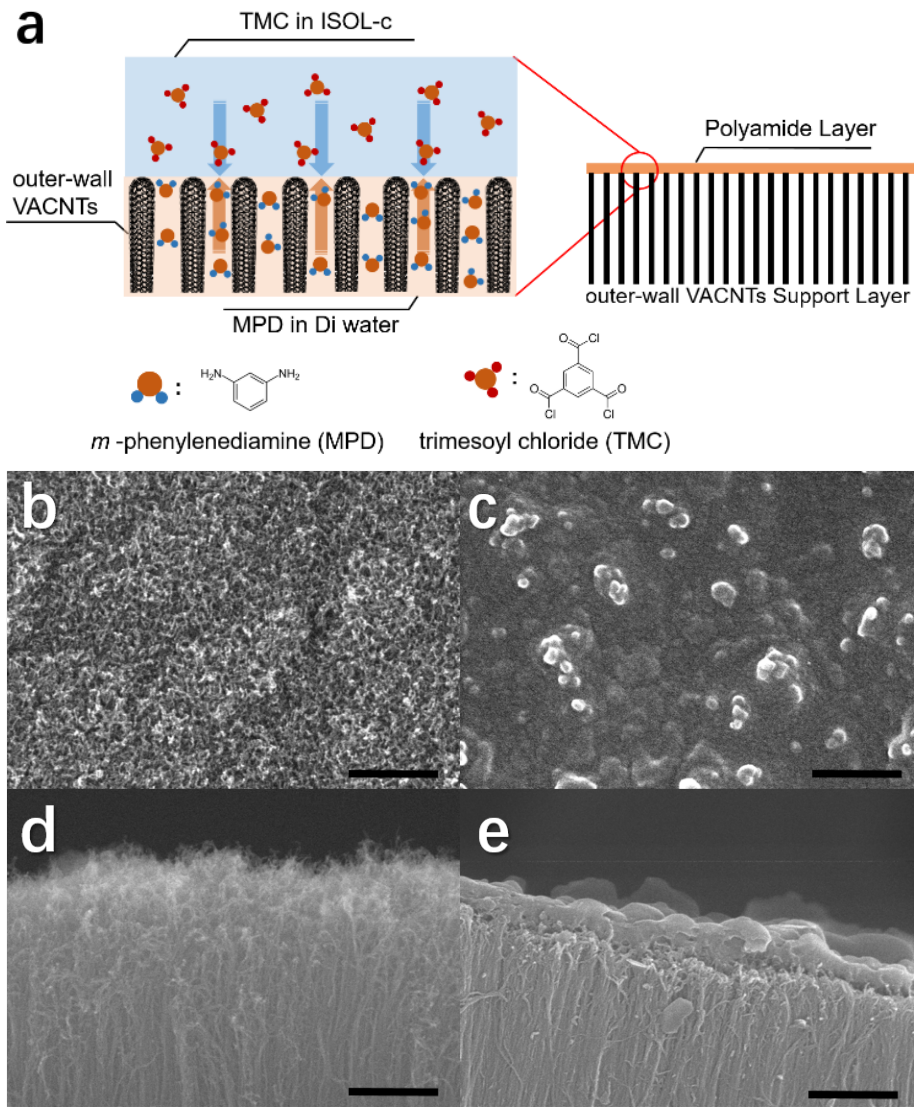

Figure 3-4. Outer-wall VACNTs and PA/outer-wall VACNTs. (a) Schematic of interfacial polymerization process for preparing PA selective layer on the top surface of outer-wall VACNTs support membrane. (b, d) Top and cross sectional SEM images of pristine outer-wall VACNTs, and (c, e) PA/outer-wall VACNTs membrane after 17 formation cycles. All scale bars are 500 nm.

Morphology of the PA layer formed on the outer-wall VACNTs support membrane was observed by scanning electron microscopy (SEM). Figures 3-4b and 3-4d show that the pristine outer-wall VACNTs membrane surface is rough and porous due to the difference in CNT lengths or heights. After the first formation cycle, a very thin fully-aromatic interfacial polymerized PA layer formed and clung to the surface of VACNTs. However, there are many voids and trenches in the PA layer due to the differences in pore size and CNT heights (Figure 3-5). When this PA/outer-wall VACNTs membrane was immersed into MPD solution again, the exposed surface of VACNTs will be filled with MPD solution by capillary force, and a new PA layer will form on top of the voids and trenches by subsequent interfacial polymerization reaction in TMC solution. After many formation cycles, a smooth planar PA membrane finally forms as shown in Figure 3-4c and 3-4e. The morphology of the membrane surface is obviously smoothened by filling the trenches and voids with repeated depositions.

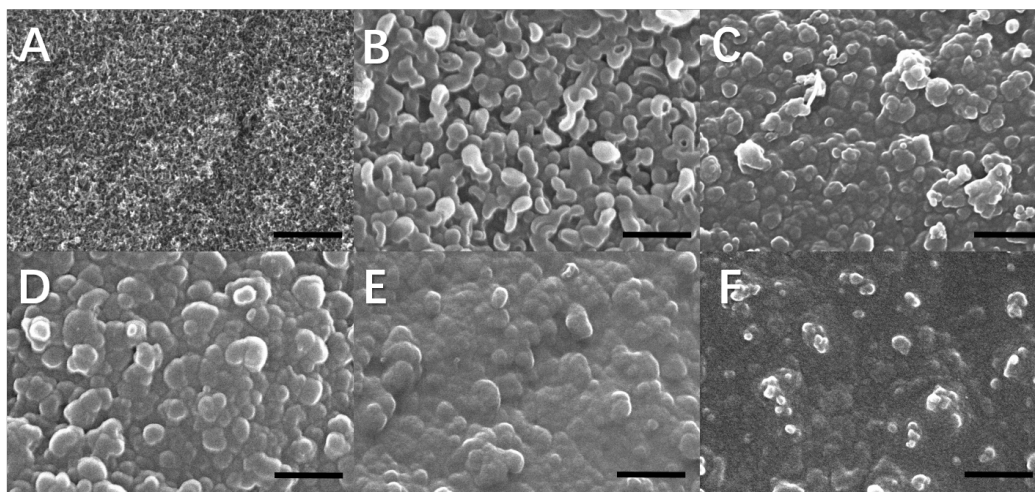

Figure 3-5. Surface SEM images of (A) the pristine outer-wall VACNTs and (B - F) 1, 5, 9, 13, 17 cycles standard PA layer deposited PA/outer-wall VACNTs respectively. All scale bar is 500 nm.

To evaluate the effect of repeated formation of PA layer on the performance of PA/outer-wall VACNTs membrane, the water flux and the corresponding salt (NaCl) rejection by PA/outer-wall VACNTs membrane were measured using a dead-end membrane filtration system with a 2000 ppm NaCl feed (Figure 3-6). The results are given as a function of the number of the formation cycles in Figure 3-7a.

The figure shows that the water flux decreases from 875.8±150.3 to 58.9±6.2 LMH as the number of the PA formation cycle increases from 1 to 17. The sharp decrease in the water flux is possibly caused by the increase in the thickness of the PA layer. The rejection increases slightly from 94.9% to 98.8% when the number of the PA formation cycle exceeds 9. After 1 cycle, the rejection is only 16.7%, which is similar to the case of the pristine outer-wall VACNTs membrane. This low rate can be attributed to the presence of many voids and trenches present in the surface where the PA layer is not formed after the formation of the first PA layer. Another possibility is that the many defects would form in the very thin PA layer formed at the beginning due to the low density of crosslinking in polyamide. As the thickness of the PA layer increases, the density of the PA layer increases and the defects are reduced.

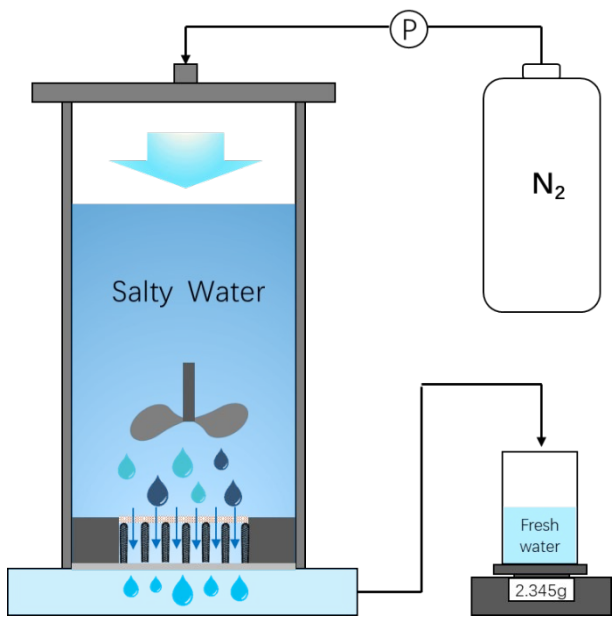

Figure 3-6. Schematic of the dead-end membrane filtration system. Water flux and rejection tests were performed using N2 gas at 15.5 bar. The permeate was collected and weighed. The water flux was calculated from the permeate volume (mL), time and total membrane area.

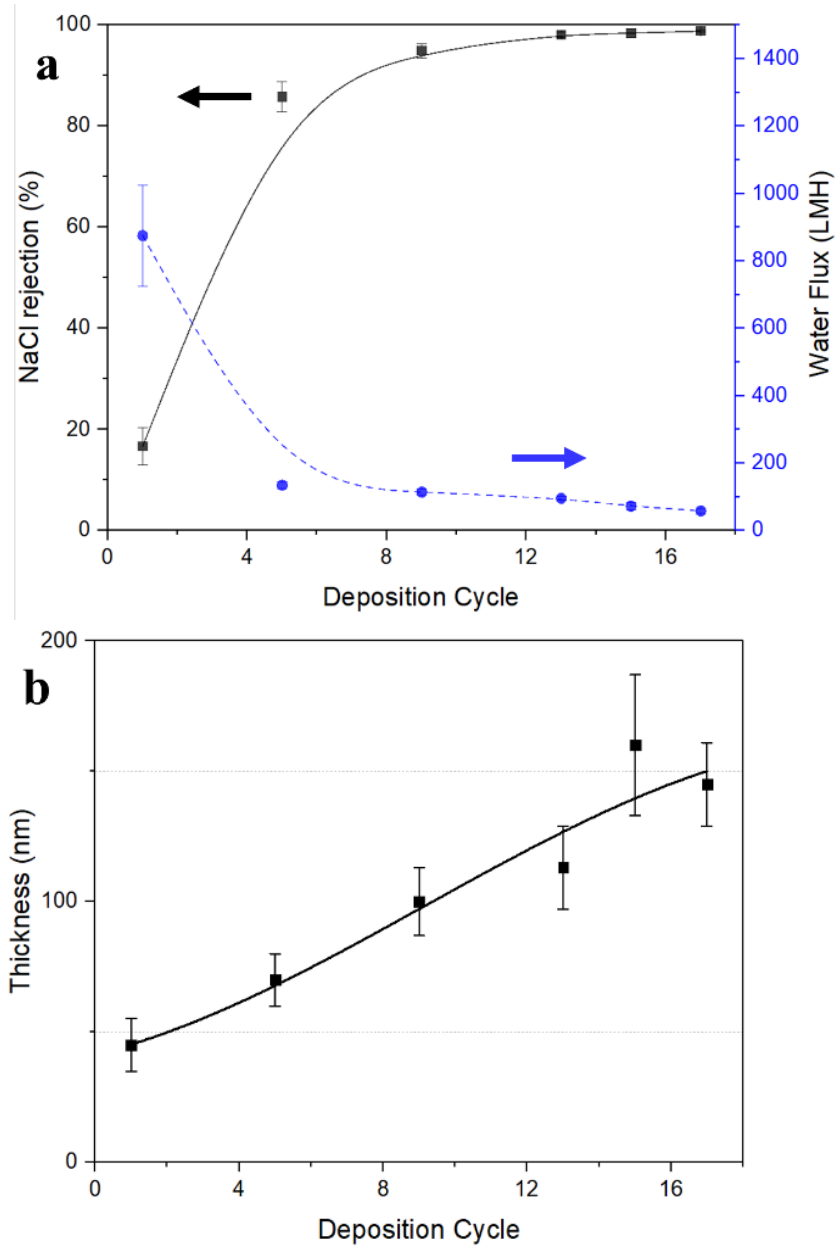

Figure 3-7. Performance of the PA/outer-wall membrane. (a) Water flux and NaCl rejection as a function of number of PA formation cycle on outer-wall VACNTs support membrane. The performance of all membranes was tested with 2000 mg/L NaCl aqueous solution and 15.5 bar operating pressure. (b) Thickness of PA layer

The most widely developed polyamide/polysulfone RO membrane has a rejection rate of around 98.4% and the corresponding water permeability is 0.4 - 3.2 LMH·bar^{-1}.[36] At the same rejection rate, the water permeability attained by PA/outer-wall VACNTs membrane is 4.7± 0.7 LMH·bar^{-1}, as shown in Figure 3-7a, which shows a significant improvement in the water permeability.

Due to the fast and relatively uncontrolled interfacial polymerization reaction employed to synthesize the active layer of the conventional polyamide/polysulfone RO membranes, the conventional RO membranes have typically crumpled ridge and valley structures. The crumpled structure makes the accurate measurement of thickness hard. Although the absolute thickness could not be obtained, it was still possible to compare the relative thickness of the PA films using SEM images. Figure 3-7b shows the increase in the PA thickness as the number of PA formation cycle is increased. The thickness increases from 45±5 nm to 145±16 nm as the cycle number increases from 1 to 17. The thickness was estimated from cross-sectional SEM images (Figure 3-8 a-e).

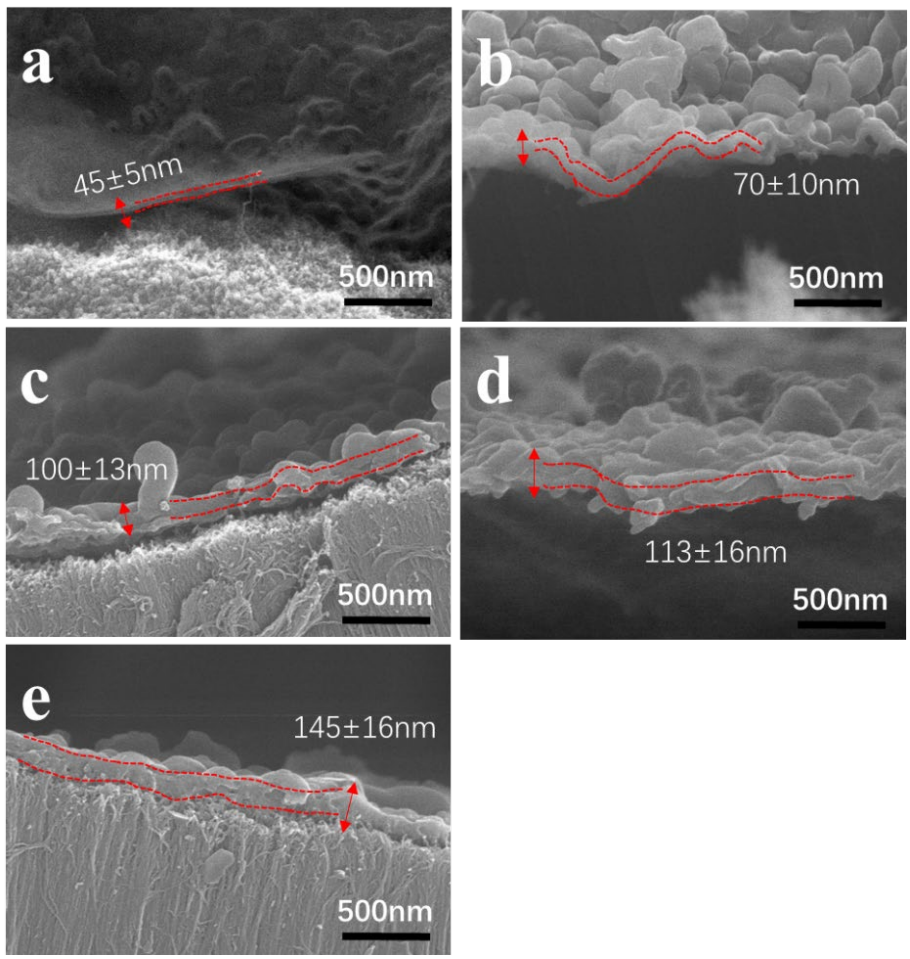

Figure 3-8. Cross-section SEM images of 1, 5, 9, 13, 17 cycles (a-e) standard PA layer deposited PA/outer-wall VACNTs respectively

The much higher water flux attained with the PA/outer-wall VACNTs membrane, compared to the traditional PA/polysulfone membrane, could be attributed to several factors. The polyamide layer formed on top of the outer-wall VACNTs is smoother without ridges and valleys, compared to the traditional polyamide/polysulfone membrane. Furthermore, the water molecules can move into CNT wall channels immediately after they pass through the PA layer owing to the ultra-high pore density of outer-wall VACNTs (Figure 3-9). Therefore, the effective path for the water molecules to pass through the PA layer and get into the water transfer channel of the supporting layer of PA/outer-wall VACNTs is relatively smaller than that of the traditional polyamide/polysulfone, in which the water molecules have to go a long way along the surface of supporting layer to find an entrance of pore. As reported by Ramon et al.'s applied numerical model [17] and X.Li et al.'s studies[67], a support layer having smaller pores and higher surface porosity would form a more permeable TFC membrane.

Another reason is that the atomically smooth and hydrophobic CNT walls lead to a frictionless water flow. A high water permeability results due to the weak interfacial force between water molecules and atomically smooth, and hydrophobic carbon walls.[39] And the densified vertically aligned CNTs array (Figure 3-10) provides much more pores available for water flow and more straight pores that lead to a shorter path to transport water, thereby resulting in a faster water flow in the supporting layer.

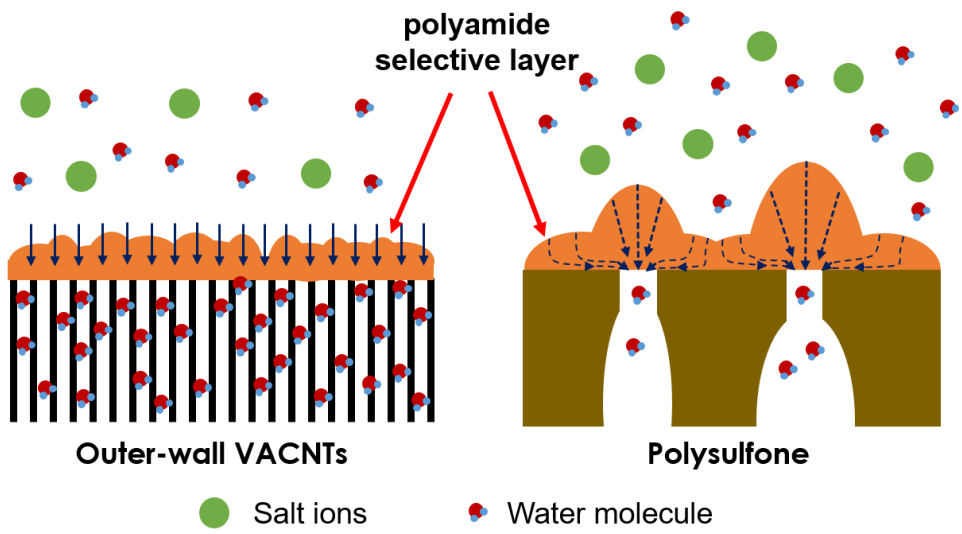

Figure 1-9. Comparison of water molecule transport. Conceptual illustration of water molecule transport in polyamide/outer-wall VACNTs membrane and in traditional polyamide/polysulfone membrane.

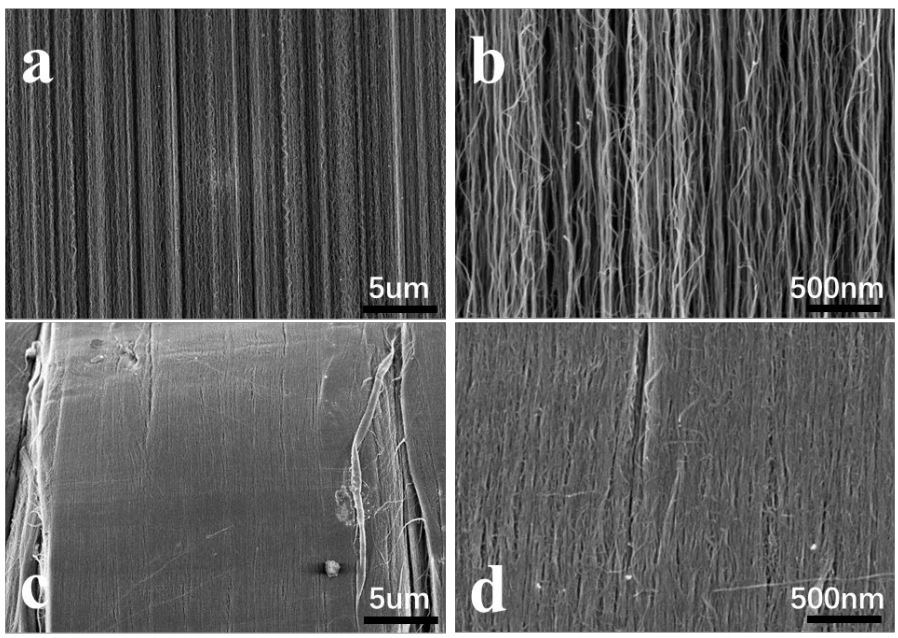

Figure 3-10. Cross-section SEM images of vertically aligned carbon nanotube forest before (a, b) and after (c, d) mechanical densification

The performance of standard PA/outer-wall VACNTs composite membrane was measured in a range of temperature from 5 to 45°C to observe the effect of temperature change on the membrane water flux. Interestingly, it was found that temperature changes have some significant effects on the water flux of the membrane as shown in Figure 3-11. When the temperature of the feed water is changed, its viscosity is also changed. The viscosity change of the feed water greatly affects the membrane flux only when water passes through PA layer because the water flow is viscous, which results in a flux reduction. When water passes through the outer-wall VA CNT support layer, the effect of the viscosity change is very limited because the flow is now slip flow without any friction between CNT walls. Another reason for the result is that with the temperature increase, the concentration polarization near the surface of PA layer decreases, eventually leading to an increase in the water permeability coefficient.[68] When the feed water temperature reaches 45°C, the water flux decreases slightly. The possible explanations are that the increasing entropy of water molecules with increasing temperature might disrupt the water transport through the outer-wall VACNTs layer.[69]

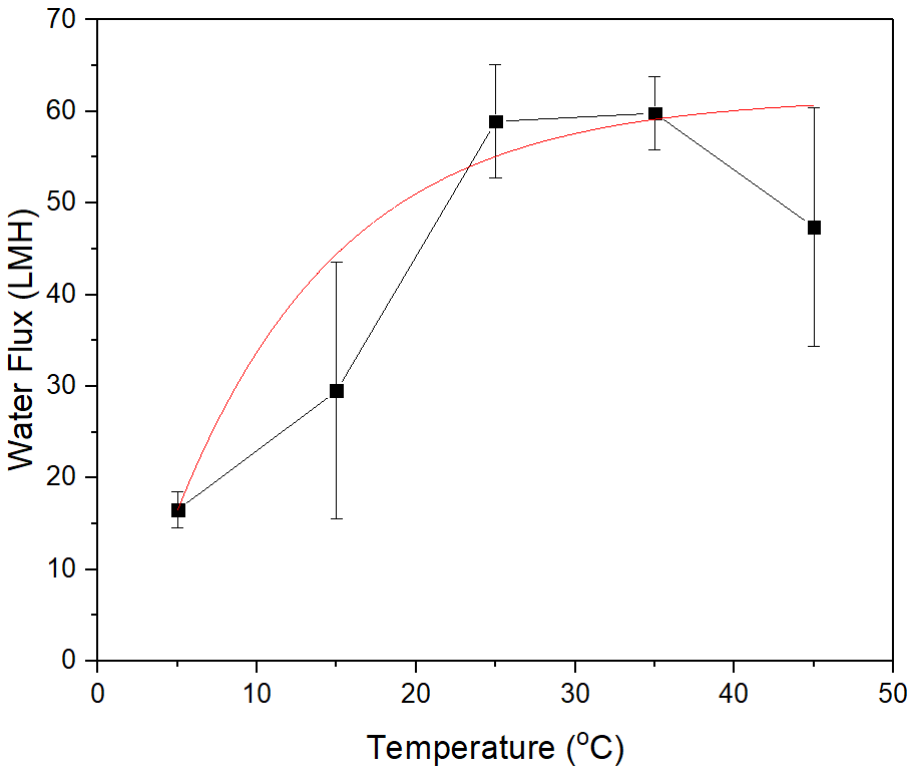

Figure 3-11. Water flux properties of the PA/outer-wall membrane with 17 times of PA formation cycle on various temperatures. The black line is the experimental data, and the red line is the asymptotic exponential trend line calculated from the data. The performance of all membranes was tested with 2000 mg/L NaCl aqueous solution and 15.5 bar operating pressure.

3.3.2. Modified PA/outer-wall VACNTs

The water flux shown in Figure 3-7, in general, decreases with increasing thickness of the PA layer, which is consistent with the literature results.[19, 70, 71] An effective way of increasing the flux, therefore, is to reduce the thickness of the PA layer. It is known that an MPD solution with appropriate amounts of additives decreases the interfacial tension and facilitates the mass transfer rate of MPD aqueous solution to TMC organic solution (the mass transfer rate between diamine molecules (MPD) and acyl chloride molecules (TMC))[72, 73], thereby decreasing the thickness. Three additives were utilized. Adding triethylamine (TEA) to the aqueous amine solution accelerates the MPD–TMC reaction by removing the hydrogen halides generated during amide bond formation. Addition of camphor sulfonic acid (CSA) can improve absorption of the amine solution and increase membrane hydrophilicity due to the increased –COOH groups, and its relatively strong acid would act as pH regulator. Adding dimethyl sulfoxide (DMSO) increases the miscibility of water-organic, and causes de-protonation of amines or hydrolysis of acid chlorides, thereby reducing their reactivity and extending crosslinking, leading to enhanced MPD diffusivity and a thinner polyamide film[74].

To show that there are no differences between the modified PA and the standard PA without additives in composition and structure, Fourier transform infrared (FTIR) spectroscopy was utilized. Both PA layers exhibited the same characteristic

peaks at 1660 cm^{-1} (amide I, C=O stretching), 1610 cm^{-1} (hydrogen bonded C=O), and 1540 cm^{-1} (amide II, N−H in-plane bending) (Figure 3-12).[72, 73, 75]

As shown in Figure 3-13a, the thickness of the modified PA/outer-wall membrane increases with increasing deposition cycles as in the standard PA/outer-wall membrane but it increases gradually, leading to a thinner layer for the same number of the deposition. The morphology of the PA surface (Figure 3-14) is similar to that of the standard PA/outer-wall membrane (Figure 3-5). Because of the thinner PA layer that resulted, the flux for the modified PA/outer-wall membrane is higher compared to the standard PA/outer-wall membrane for the same deposition cycle, as shown in Figure. 3-13b.

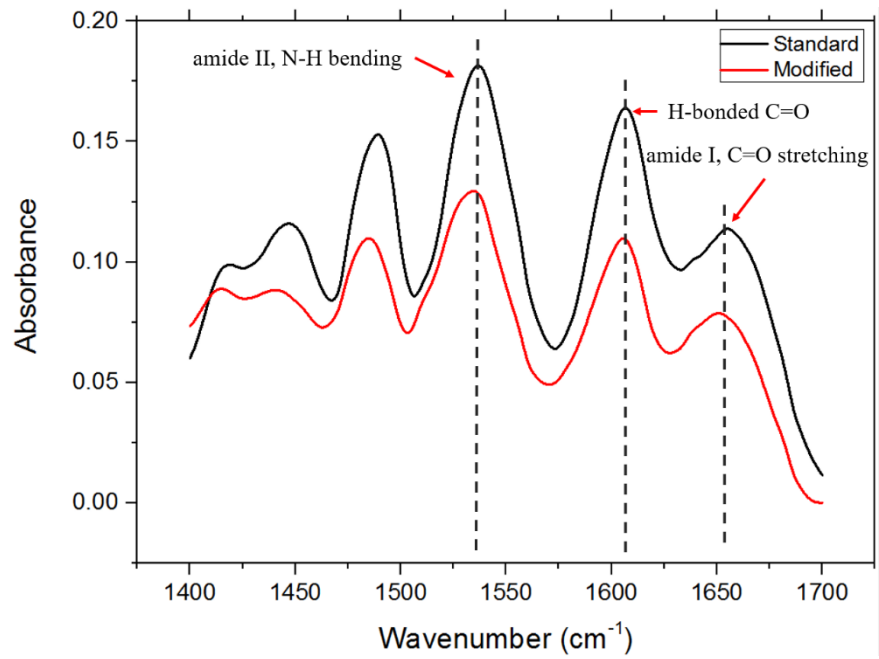

Figure 3-12. FT-IR spectra of the standard and modified PA layer on outer-wall VACNTs membrane. Vertical lines represent the positions of the characteristic amide peaks (1,660 cm-1 (amide I, C=O stretching), 1,610 cm-1 (H-bonded C=O), and 1,540 cm-1 (amide II, N-H bending).

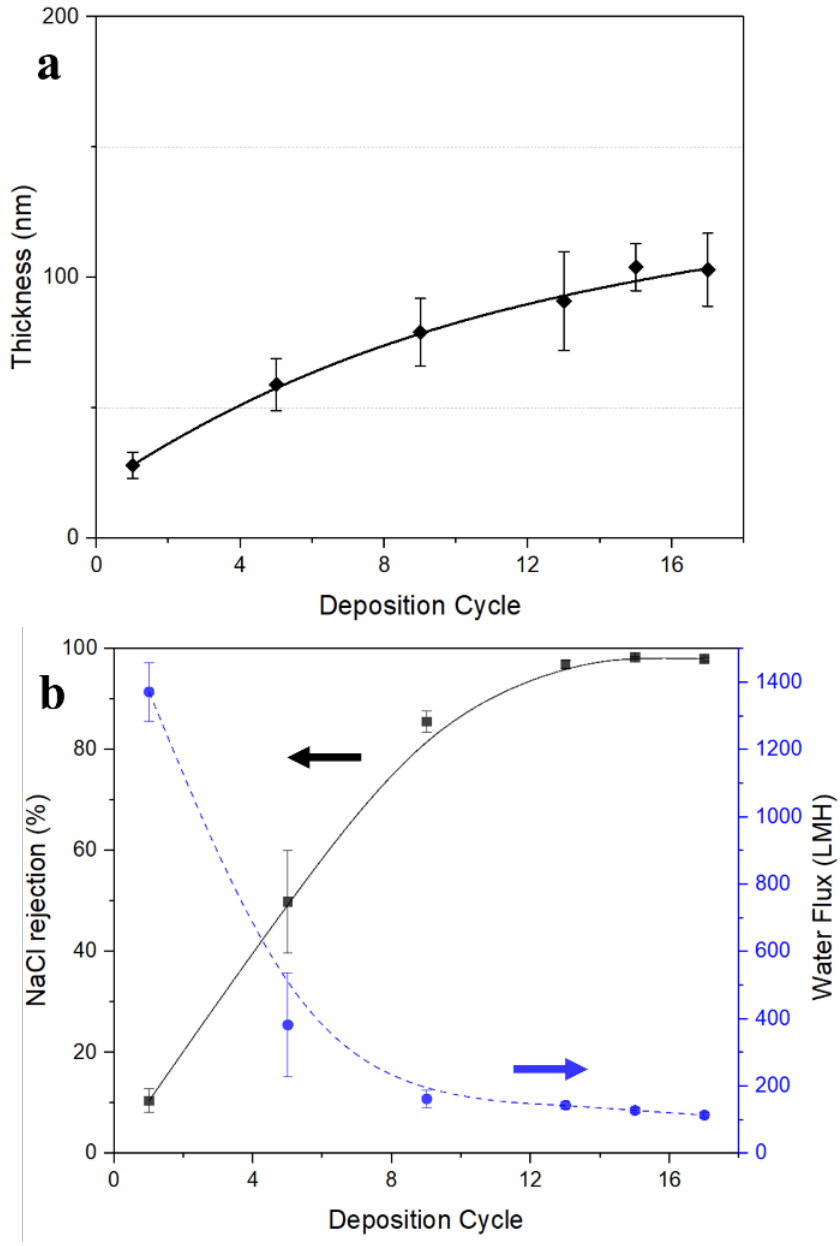

Figure 3-13. Performance of the modified PA/outer-wall membrane. (a) Thickness of modified PA layer on outer-wall VACNTs membrane as a function of the deposition cycle number. (b) Water flux and NaCl rejection of the modified PA/outer-wall VACNTs membrane as a function of the deposition cycle numbers.

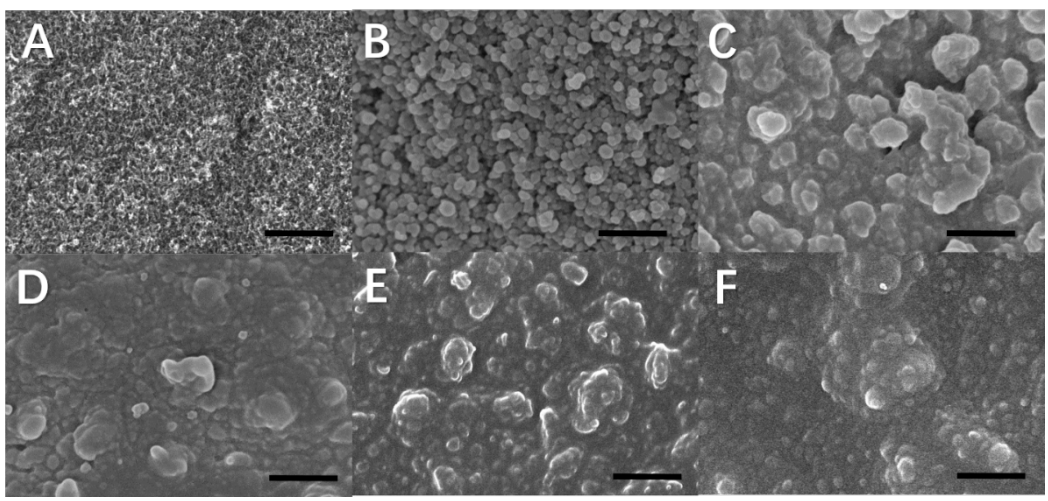

Figure 3-14. Surface SEM images of (A) the pristine outer-wall VACNTs and (B - F) 1, 5, 9, 13, 17 cycles modified PA layer deposited PA/outer-wall VACNTs respectively. All scale bar is 500 nm.

Figure 3-15 shows the best result obtained with the modified PA/outer-wall VACNTs membrane, noted by red star, along with other literature results. The red star represents the modified PA/outer-wall VACNTs membrane obtained after 15 formation cycles. The water flux was 128.6 LMH at 98.3% rejection (Figure 3-13b), which is much higher than the best water flux obtained with the standard PA/outer-wall VACNTs membrane (72.8 LMH at 98.4% rejection). The increase in the flux is largely due to a decrease in the PA layer thickness. As shown in Figure 3-13a, the PA layer thickness increased from 28±5 nm to 103±14 nm as the number of formation cycles was increased from 1 to 17. This thickness after 17 cycles (103 nm) is much smaller than the thickness that resulted by the standard PA formation procedure after 17 cycles (145 nm). The thickness was estimated from cross-sectional SEM images (Figure 3-16 a-e).

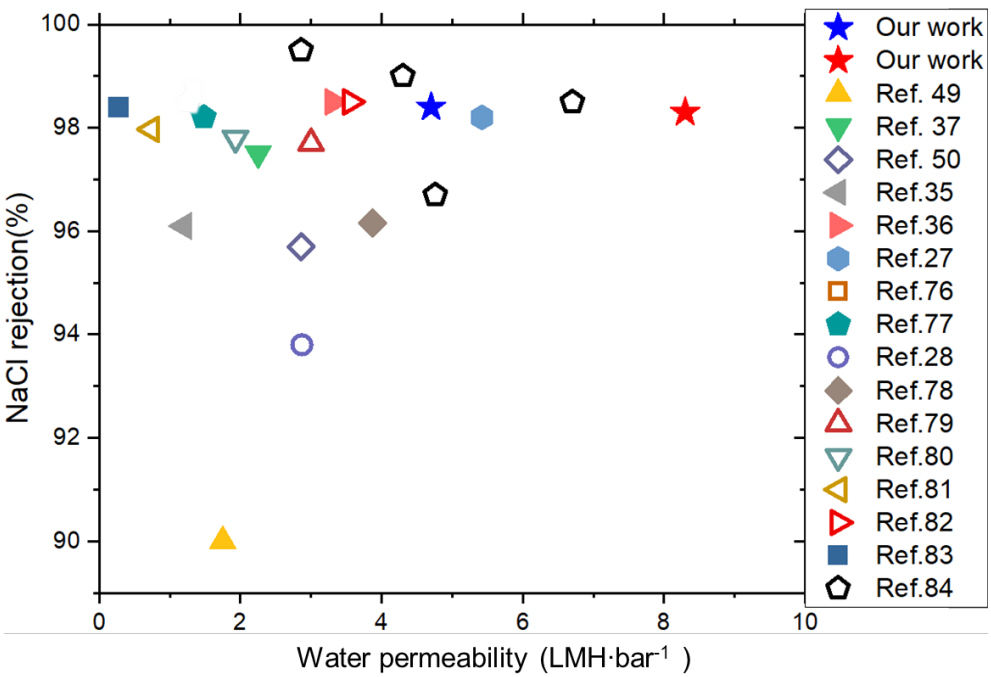

Figure 3-12. Water permeability and NaCl rejection plot. Comparison of the results from this work and other literature for desalination membranes.

Table 3-2. Comparison of performance of our works with others.

Membrane	*Unit water flux [LMH/bar]*	*Rejection [%]*	*Pressure (bar)*	*References*
PA/VACNTs	4.7	98.4	15.5	Our work
m-PA/VACNTs	8.3	98.3	15.5	Our work
CNT mixed memb.	2.25	97.5	15.5	5
CNT mixed memb.	1.75	90	16	4
CNT mixed memb.	3.87	96.16	15	42
CNT/Polysulfone	3.03	97.7	15.5	43
GO mixed memb.	5.42	98.2	15.5	25
CNT mixed memb.	1.93	97.8	15	44
CNT mixed memb.	2.86	95.7	15.5	6
CNT/PES	1.20	96.1	20	17
CNT-TNT Comp	0.74	97.97	15	45
CNT mixed memb.	3.41	98.5	15.5	23
GO mixed memb.	3.56	98.5	10	46
LBL Polyamide	1.34	98.7	15.5	39
LBL Polyamide	1.48	98.2	15.5	40
GO mixed memb.	2.87	93.8	20.7	41

Dow BW30LE	*4.3*	*99*	*10.34*	*47*
GE Osmonics SE	1.27	98.5	29.3	47
Koch TFC-ULP	6.7	98.5	6.9	47
Beidouxing RO	4.76	96.7	10.5	47
LG NanoH2O	2.86	99.5	15.5	47
LG SW400	0.27	98.4	15.5	48, Test in This work

Please note that for fairly comparison with other membranes, unit water flux (LMH bar-1) is used in this table and figure 3-15.

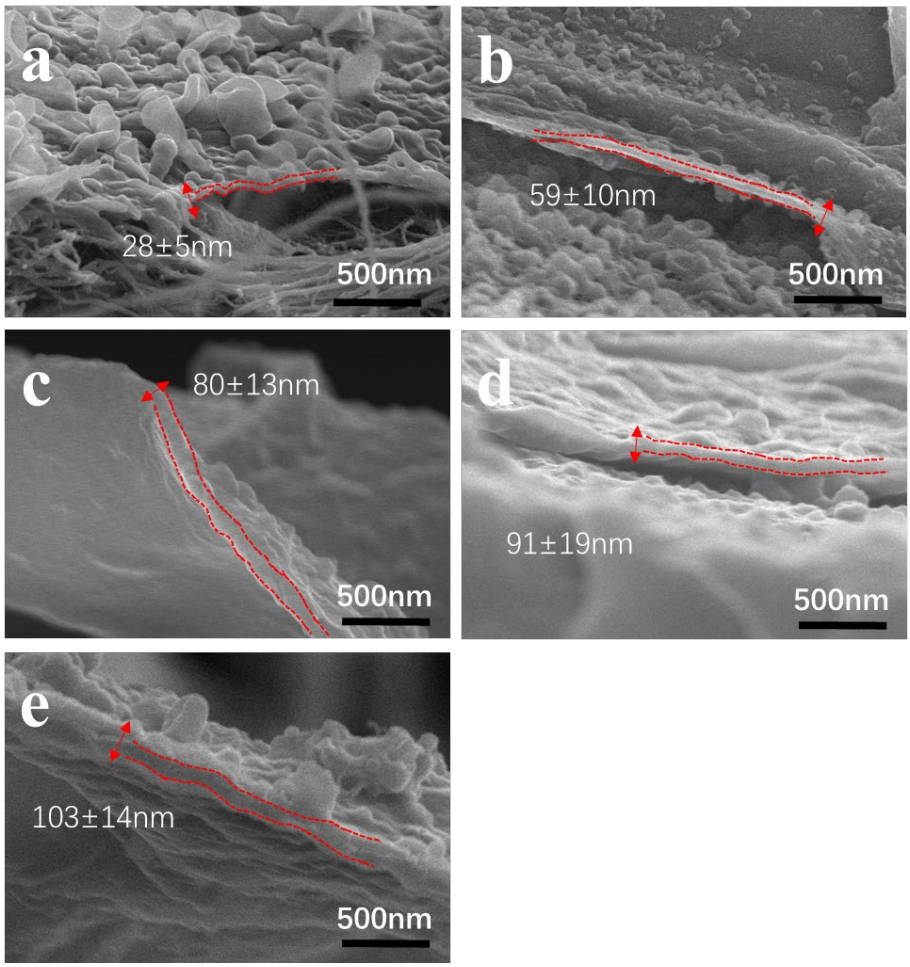

Figure 3-16. Cross-section SEM images of 1, 5, 9, 13, 17 cycles (a-e) Modified PA layer deposited PA/outer-wall VACNTs respectively.

The long-term stability of the modified PA/outer-wall VACNTs membrane with 15 formation cycles is presented in Figure 3-17. A little reduction in permeability occurs in the first 4 hours but the NaCl rejection rate rather increases slightly. The permeability and NaCl rejection rate remained steady at around 130 LMH and 98% rejection rate after 4 hours. A possible explanation for the change in the first 4 hours is that a high hydraulic pressure applied to the membrane might bring some changes in pore structure of the outer wall VACNT membrane such as pore size and pore tortuosity. The flux reduction caused by the high pressure have been already reported in previous studies for the conventional polymer membranes.[76] The high pressure is applied to CNT axis in the case of PA/outer wall CNT membrane. CNTs have excellent mechanical strength along its axis. Therefore, the changes in the pore structure caused by the high pressure did not have a great effect on the permeability and the rejection rate.

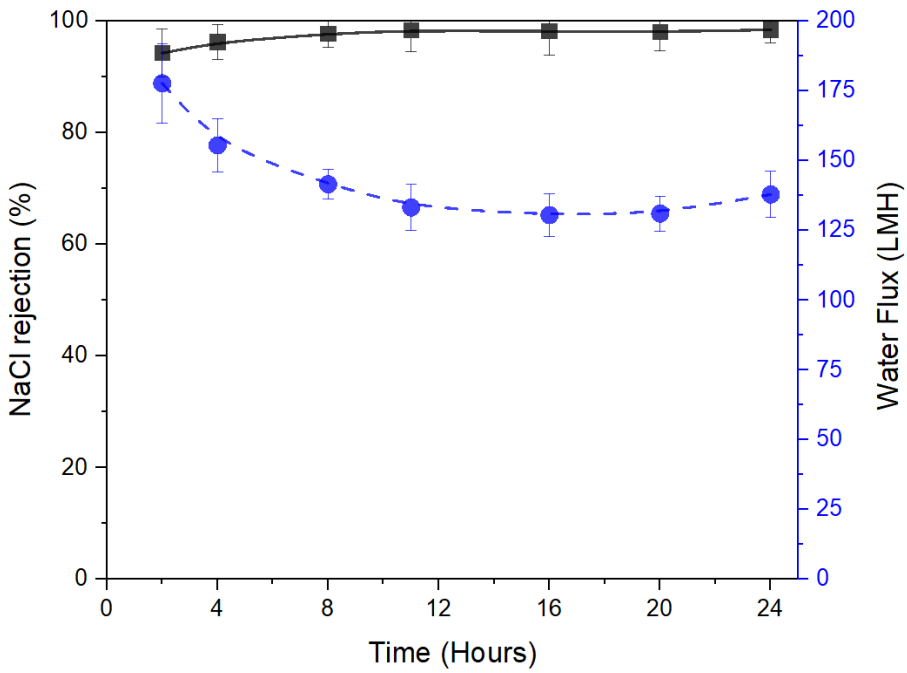

Figure 3-17. long-term filtration process of PA/outer-wall VACNTs membrane with 15 formation cycles for NaCl rejection and flux performance at room temperature.

3.4 Conclusion

We have presented a new type of RO membrane which employs densified vertically-aligned CNTs as a support layer that has completely different structure from the traditional polymer support layer. This membrane provides a water flux of 128.6 LMH and 98.3% rejection at 15.5bar for brackish water, far surpassing the performance of other similar studies and some commercial reverse osmosis membranes (Figure 3-15 and Table 3-2).[27, 28, 35-37, 50, 51, 77-85] Most researchers have focused on the modification of polyamide active layer and the development of synthesis methods in order to improve the perfomance of reverse osmosis membranes. This study provides a new approach for the development of RO membranes with a high water permeability. The approach with a uniquelly structured support layer can be a solution to overcome the current drawbacks of the traditional RO membranes.

Chapter 4.

Summary

From household water purifiers to industrial ultrapure water manufacturing and sea water desalination projects, the utilization and market share of reverse osmosis membrane are growing rapidly. Although the technology upgrade is still going on, the recent research and development of RO membranes are mainly focus on the improvement of salt rejection and anti-pollution performance, for example, LG Chem's SWRO series has increased the salt rejection to a high level of 99.89%, and the RO membrane products of Dupont and NanoH2O have significantly improved their anti-pollution performance. However, the improvement of the water permeability of the RO membrane has not progressed for many years, and the research and development of upgrading the water permeability seems to have entered the bottleneck. the maximum water permeability for RO membrane products for brackish water is 5LMH/bar, and for sea water desalination is only 3LMH/bar for many years. Z. Yang, et al. established a upper bound behavior relationship between the water permeance and the water/NaCl selectivity for TFC membranes as shown in figure 4-1[86, 87].

Even though the separation performances of a few commercial RO is reasonably close to the upper bound line, the data points for many RO and NF membranes fall far below this line. There is still room for improvement in water permeability for the RO or NF membrane with the conventional structure such as the polymer support

layer and the PA active layer. The traditional wisdom believes that the support layer of a TFC membrane has little effect on its overall transport properties since the transport resistance to both water and solutes should be dominated by that of the polyamide layer according to the resistance-in-series model. Nevertheless, recent studies show increasing evidence that membrane support layer can play a critical role in the separation properties of TFC membranes. therefor, the upgrade of the traditional polymer support layer could be one important aspect for improving the membranes' performeance.

In recent years, there are many ideal candidates of nanomaterials that are active in various research fields, such as carbon nanotubes and graphene. For traditional RO membrane structures, the development of support layers with higher pore density and hydrophilic pore surface with emerging nanomaterials and nanotechnology is an important research direction. Alternatively, beyond the limitations of the traditional RO membrane structure for decades, it is promising to use carbon nanomaterials to develop revolutionary single-pass reverse osmosis structures with non-multilayer structures.In our study of the reverse osmosis membrane support layer, we first grafted a interlayer of graphene oxide on the macroporous microfiltration membrane, through this interlayer to control the synthesis of the PA layer on the surface of support layer, and through the size of GO nanosheets to optimize and increase water flux of RO membrane or the support layer. It was found that the support layer or RO membrane, which with the smaller GO nanosheets interlayer, the larger the water

flux due to the more water transfer channels formed by longer edge length. And the best performance of the RO membrane can be obtained by the MF support layer which with a diameter similar to that of GO nanosheets. Secondly, we used a vertically-aligned carbon nanotube with an extremely high pore density as the support layer and synthesized the PA layer in situ on the surface of VACNTs. The RO membrane of the PA/VACNTs structure is much higher than other research results and commercial RO membranes as shown in figure 4-2. According to our research results, the research direction of improving the support layer to improve the performance of RO membrane is correct.

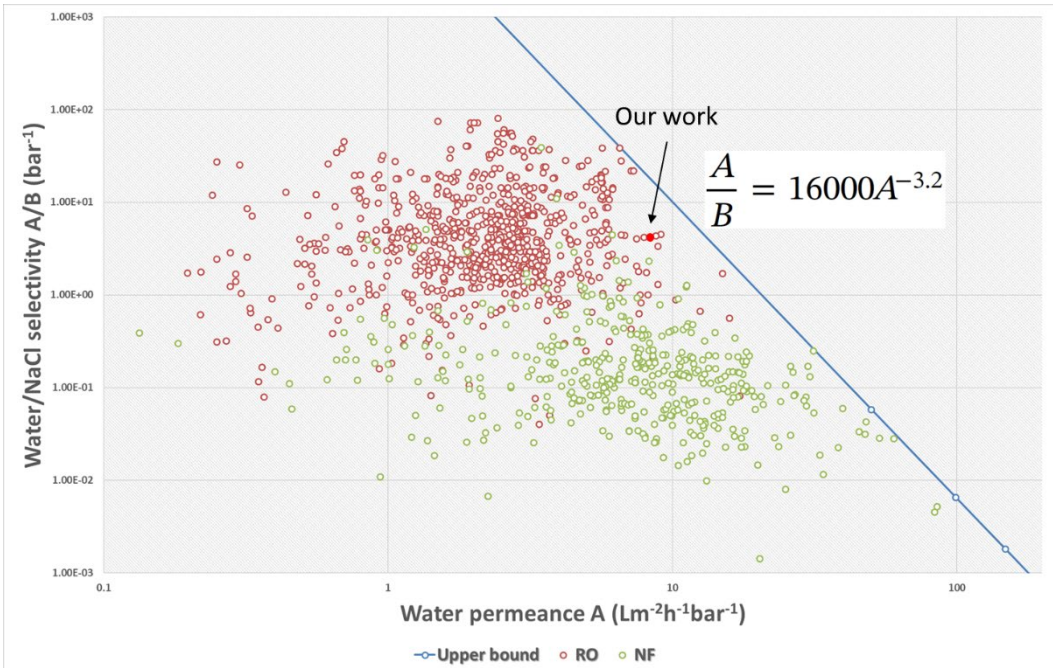

Figure 4-1. Water permeance and selectivity of commercial or laboratory-scale synthetic seawater RO, brackish water RO and NF membranes in the water permeance and selectivity diagram. The blue line is the upper bound of water/NaCl selectivity A/B and water permeance. A and B are the water permeability coefficient A (also known as the water permeance) and solute permeability coefficient respectively.

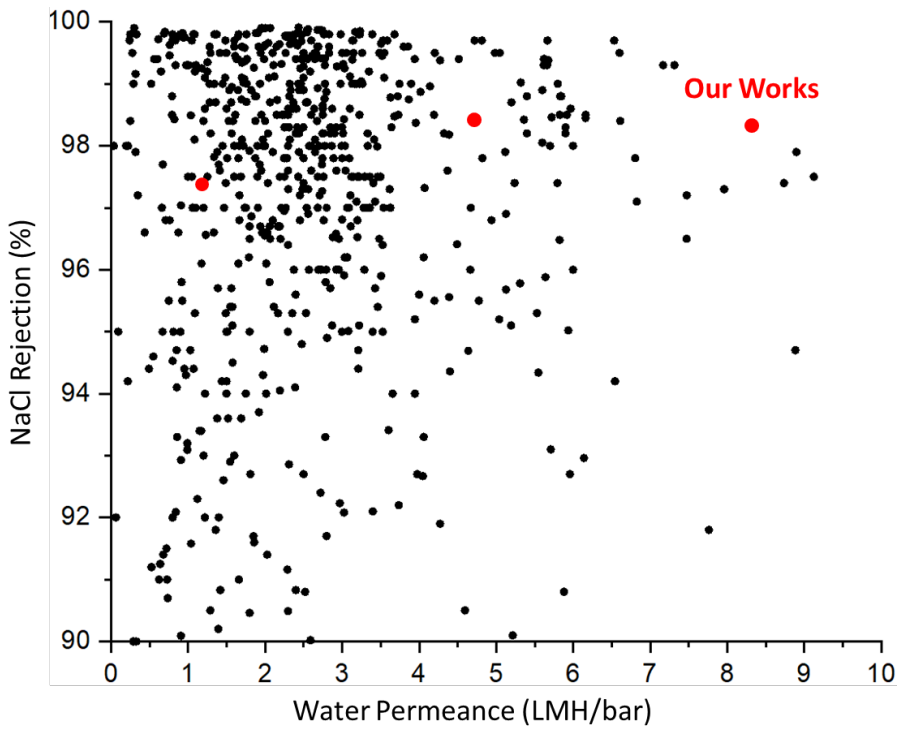

Figure 4-2. Water permeance and selectivity of commercial or laboratory-scale synthetic seawater ROand brackish water RO in the water permeance and Nacl rejection diagram. The result of our works shows the best performance at at the same salt rejection.

Bibliography

1. Schneider, S.H. and F.K. Hare, *Encyclopedia of climate and weather*. Vol. 678. 1996: Oxford university press New York.
2. Cook, B.I., et al., *Global warming and 21st century drying.* Climate Dynamics, 2014. **43**(9): p. 2607-2627.
3. Gosling, S.N. and N.W. Arnell, *A global assessment of the impact of climate change on water scarcity.* Climatic Change, 2016. **134**(3): p. 371-385.
4. Rodell, M., et al., *Emerging trends in global freshwater availability.* Nature, 2018. **557**(7707): p. 651-659.
5. Mekonnen, M.M. and A.Y. Hoekstra, *Four billion people facing severe water scarcity.* Science Advances, 2016. **2**(2): p. e1500323.
6. Maddocks, A., R.S. Young, and P. Reig, *Ranking the world's most water-stressed countries in 2040.* World Resources Institute. Available at: http://www. wri. org/blog/2015/08/ranking-world% E2, 2015. **80**.
7. Baker, R.W., *Membrane technology and applications*. 2012: John Wiley & Sons.
8. Warsinger, D.M., et al., *Energy efficiency of batch and semi-batch (CCRO) reverse osmosis desalination.* Water Research, 2016. **106**: p. 272-282.
9. Crittenden, J.C., et al., *MWH's water treatment: principles and design*. 2012: John Wiley & Sons.
10. Greenlee, L.F., et al., *Reverse osmosis desalination: Water sources, technology, and today's challenges.* Water Research, 2009. **43**(9): p. 2317-2348.
11. Anis, S.F., R. Hashaikeh, and N. Hilal, *Reverse osmosis pretreatment technologies and future trends: A comprehensive review.* Desalination, 2019. **452**: p. 159-195.
12. Banat, F. *Economic and technical assessment of desalination technologies*. in *IWA Conference-New Technologies for Water and Wastewater Treatment in the 21st Century, Geneva, Switzerland, June*. 2007.
13. Ghosh, A.K. and E.M.V. Hoek, *Impacts of support membrane structure and chemistry on polyamide–polysulfone interfacial composite membranes.* Journal of Membrane Science, 2009. **336**(1): p. 140-148.
14. Huang, L. and J.R. McCutcheon, *Impact of support layer pore size on performance of thin film composite membranes for forward osmosis.* Journal of Membrane Science, 2015. **483**: p. 25-33.
15. Misdan, N., et al., *Formation of thin film composite nanofiltration*

membrane: Effect of polysulfone substrate characteristics. Desalination, 2013. **329**: p. 9-18.

16. Lonsdale, H., et al., *Transport in composite reverse osmosis membranes*, in *Membrane Processes in Industry and Biomedicine*. 1971, Springer. p. 101-122.
17. Ramon, G.Z., M.C.Y. Wong, and E.M.V. Hoek, *Transport through composite membrane, part 1: Is there an optimal support membrane?* Journal of Membrane Science, 2012. **415-416**: p. 298-305.
18. Karan, S., Z. Jiang, and A.G. Livingston, *Sub–10 nm polyamide nanofilms with ultrafast solvent transport for molecular separation.* Science, 2015. **348**(6241): p. 1347-1351.
19. Jiang, Z., S. Karan, and A.G. Livingston, *Water transport through ultrathin polyamide nanofilms used for reverse osmosis.* Advanced Materials, 2018. **30**(15): p. 1705973.
20. Lee, C., et al., *Measurement of the Elastic Properties and Intrinsic Strength of Monolayer Graphene.* Science, 2008. **321**(5887): p. 385-388.
21. Bonaccorso, F., et al., *Graphene, related two-dimensional crystals, and hybrid systems for energy conversion and storage.* Science, 2015. **347**(6217): p. 1246501.
22. Balandin, A.A., et al., *Superior Thermal Conductivity of Single-Layer Graphene.* Nano Letters, 2008. **8**(3): p. 902-907.
23. Geim, A.K. and K.S. Novoselov, *The rise of graphene.* Nature Materials, 2007. **6**: p. 183.
24. Yang, Y.H. and W.Z. Li, *Radial elasticity of single-walled carbon nanotube measured by atomic force microscopy.* Applied Physics Letters, 2011. **98**(4): p. 041901.
25. Ganesh, B.M., A.M. Isloor, and A.F. Ismail, *Enhanced hydrophilicity and salt rejection study of graphene oxide-polysulfone mixed matrix membrane.* Desalination, 2013. **313**: p. 199-207.
26. Zinadini, S., et al., *Preparation of a novel antifouling mixed matrix PES membrane by embedding graphene oxide nanoplates.* Journal of Membrane Science, 2014. **453**: p. 292-301.
27. Lee, J., et al., *A facile route to enhance the water flux of a thin-film composite reverse osmosis membrane: incorporating thickness-controlled graphene oxide into a highly porous support layer.* Journal of Materials Chemistry A, 2015. **3**(44): p. 22053-22060.
28. Yin, J., G. Zhu, and B. Deng, *Graphene oxide (GO) enhanced polyamide (PA) thin-film nanocomposite (TFN) membrane for water purification.*

Desalination, 2016. **379**: p. 93-101.
29. Bano, S., et al., *Graphene oxide modified polyamide nanofiltration membrane with improved flux and antifouling properties.* Journal of Materials Chemistry A, 2015. **3**(5): p. 2065-2071.
30. Chae, H.-R., et al., *Synergetic effect of graphene oxide nanosheets embedded in the active and support layers on the performance of thin-film composite membranes.* Journal of Membrane Science, 2017. **525**: p. 99-106.
31. Chae, H.-R., et al., *Graphene oxide-embedded thin-film composite reverse osmosis membrane with high flux, anti-biofouling, and chlorine resistance.* Journal of Membrane Science, 2015. **483**: p. 128-135.
32. Rao, G.P., C. Lu, and F. Su, *Sorption of divalent metal ions from aqueous solution by carbon nanotubes: A review.* Separation and Purification Technology, 2007. **58**(1): p. 224-231.
33. Upadhyayula, V.K.K., et al., *Application of carbon nanotube technology for removal of contaminants in drinking water: A review.* Science of The Total Environment, 2009. **408**(1): p. 1-13.
34. Sarkar, B., et al., *Designer carbon nanotubes for contaminant removal in water and wastewater: A critical review.* Science of The Total Environment, 2018. **612**: p. 561-581.
35. Son, M., et al., *Efficacy of carbon nanotube positioning in the polyethersulfone support layer on the performance of thin-film composite membrane for desalination.* Chemical Engineering Journal, 2015. **266**: p. 376-384.
36. Dae, L.H., et al., *Experimental Evidence of Rapid Water Transport through Carbon Nanotubes Embedded in Polymeric Desalination Membranes.* Small, 2014. **10**(13): p. 2653-2660.
37. Kim, H.J., et al., *High-Performance Reverse Osmosis CNT/Polyamide Nanocomposite Membrane by Controlled Interfacial Interactions.* ACS Applied Materials & Interfaces, 2014. **6**(4): p. 2819-2829.
38. Das, R., et al., *Carbon nanotube membranes for water purification: A bright future in water desalination.* Desalination, 2014. **336**: p. 97-109.
39. Lee, B., et al., *A carbon nanotube wall membrane for water treatment.* Nature Communications, 2015. **6**: p. 7109.
40. Shannon, M.A., et al., *Science and technology for water purification in the coming decades.* Nature, 2008. **452**: p. 301.
41. Elimelech, M. and W.A. Phillip, *The Future of Seawater Desalination: Energy, Technology, and the Environment.* Science, 2011. **333**(6043): p.

712-717.
42. Hu, M. and B. Mi, *Enabling Graphene Oxide Nanosheets as Water Separation Membranes.* Environmental Science & Technology, 2013. **47**(8): p. 3715-3723.
43. Xu, Y., et al., *Solution Processable Holey Graphene Oxide and Its Derived Macrostructures for High-Performance Supercapacitors.* Nano Letters, 2015. **15**(7): p. 4605-4610.
44. Johra, F.T., J.-W. Lee, and W.-G. Jung, *Facile and safe graphene preparation on solution based platform.* Journal of Industrial and Engineering Chemistry, 2014. **20**(5): p. 2883-2887.
45. Yoo, M.J. and H.B. Park, *Effect of hydrogen peroxide on properties of graphene oxide in Hummers method.* Carbon, 2019. **141**: p. 515-522.
46. Zhao, X., et al., *Alternate Multilayer Films of Poly(vinyl alcohol) and Exfoliated Graphene Oxide Fabricated via a Facial Layer-by-Layer Assembly.* Macromolecules, 2010. **43**(22): p. 9411-9416.
47. Morelos-Gomez, A., et al., *Effective NaCl and dye rejection of hybrid graphene oxide/graphene layered membranes.* Nature Nanotechnology, 2017. **12**: p. 1083.
48. Hung, W.-S., et al., *Cross-Linking with Diamine Monomers To Prepare Composite Graphene Oxide-Framework Membranes with Varying d-Spacing.* Chemistry of Materials, 2014. **26**(9): p. 2983-2990.
49. Shi, J., et al., *Confined interfacial polymerization of polyamide-graphene oxide composite membranes for water desalination.* Desalination, 2018. **441**: p. 77-86.
50. Zhao, H., et al., *Improving the performance of polyamide reverse osmosis membrane by incorporation of modified multi-walled carbon nanotubes.* Journal of Membrane Science, 2014. **450**: p. 249-256.
51. Kim, H.J., et al., *High-performance reverse osmosis nanocomposite membranes containing the mixture of carbon nanotubes and graphene oxides.* Journal of Materials Chemistry A, 2015. **3**(13): p. 6798-6809.
52. Chan, W.-F., et al., *Zwitterion Functionalized Carbon Nanotube/Polyamide Nanocomposite Membranes for Water Desalination.* ACS Nano, 2013. **7**(6): p. 5308-5319.
53. Tiraferri, A., C.D. Vecitis, and M. Elimelech, *Covalent Binding of Single-Walled Carbon Nanotubes to Polyamide Membranes for Antimicrobial Surface Properties.* ACS Applied Materials & Interfaces, 2011. **3**(8): p. 2869-2877.
54. Shen, J.n., et al., *Preparation and characterization of thin-film*

nanocomposite membranes embedded with poly(methyl methacrylate) hydrophobic modified multiwalled carbon nanotubes by interfacial polymerization. Journal of Membrane Science, 2013. **442**: p. 18-26.
55. Inukai, S., et al., *High-performance multi-functional reverse osmosis membranes obtained by carbon nanotube·polyamide nanocomposite.* Scientific Reports, 2015. **5**: p. 13562.
56. Roy, S., et al., *Facile fabrication of superior nanofiltration membranes from interfacially polymerized CNT-polymer composites.* Journal of Membrane Science, 2011. **375**(1): p. 81-87.
57. Shawky, H.A., et al., *Synthesis and characterization of a carbon nanotube/polymer nanocomposite membrane for water treatment.* Desalination, 2011. **272**(1): p. 46-50.
58. Vatanpour, V., et al., *Fabrication and characterization of novel antifouling nanofiltration membrane prepared from oxidized multiwalled carbon nanotube/polyethersulfone nanocomposite.* Journal of Membrane Science, 2011. **375**(1): p. 284-294.
59. Qiu, S., et al., *Preparation and properties of functionalized carbon nanotube/PSF blend ultrafiltration membranes.* Journal of Membrane Science, 2009. **342**(1): p. 165-172.
60. Wu, H., B. Tang, and P. Wu, *Novel ultrafiltration membranes prepared from a multi-walled carbon nanotubes/polymer composite.* Journal of Membrane Science, 2010. **362**(1): p. 374-383.
61. Maphutha, S., et al., *A carbon nanotube-infused polysulfone membrane with polyvinyl alcohol layer for treating oil-containing waste water.* Scientific Reports, 2013. **3**: p. 1509.
62. Sparreboom, W., A. van den Berg, and J.C.T. Eijkel, *Principles and applications of nanofluidic transport.* Nature Nanotechnology, 2009. **4**: p. 713.
63. Holt, J.K., et al., *Fast Mass Transport Through Sub-2-Nanometer Carbon Nanotubes.* Science, 2006. **312**(5776): p. 1034-1037.
64. Sahoo, N.G., et al., *Polymer nanocomposites based on functionalized carbon nanotubes.* Progress in Polymer Science, 2010. **35**(7): p. 837-867.
65. Wardle, B.L., et al., *Fabrication and Characterization of Ultrahigh-Volume- Fraction Aligned Carbon Nanotube–Polymer Composites.* Advanced Materials, 2008. **20**(14): p. 2707-2714.
66. L., W.B., et al., *Fabrication and Characterization of Ultrahigh-Volume-Fraction Aligned Carbon Nanotube–Polymer Composites.* Advanced Materials, 2008. **20**(14): p. 2707-2714.

67. Li, X., et al., *Effects of the support on the characteristics and permselectivity of thin film composite membranes.* Journal of Membrane Science, 2019. **580**: p. 12-23.
68. Jin, X., et al., *Effects of feed water temperature on separation performance and organic fouling of brackish water RO membranes.* Desalination, 2009. **239**(1): p. 346-359.
69. Baek, Y., et al., *High performance and antifouling vertically aligned carbon nanotube membrane for water purification.* Journal of Membrane Science, 2014. **460**: p. 171-177.
70. Freger, V., *Nanoscale Heterogeneity of Polyamide Membranes Formed by Interfacial Polymerization.* Langmuir, 2003. **19**(11): p. 4791-4797.
71. Dražević, E., K. Košutić, and V. Freger, *Permeability and selectivity of reverse osmosis membranes: Correlation to swelling revisited.* Water Research, 2014. **49**: p. 444-452.
72. Kim, S.H., S.-Y. Kwak, and T. Suzuki, *Positron Annihilation Spectroscopic Evidence to Demonstrate the Flux-Enhancement Mechanism in Morphology-Controlled Thin-Film-Composite (TFC) Membrane.* Environmental Science & Technology, 2005. **39**(6): p. 1764-1770.
73. Kim, I.-C., et al., *Preparation of high flux thin film composite polyamide membrane: The effect of alkyl phosphate additives during interfacial polymerization.* Desalination, 2013. **308**: p. 111-114.
74. Ghosh, A.K., et al., *Impacts of reaction and curing conditions on polyamide composite reverse osmosis membrane properties.* Journal of Membrane Science, 2008. **311**(1): p. 34-45.
75. Choi, W., et al., *Layer-by-Layer Assembly of Graphene Oxide Nanosheets on Polyamide Membranes for Durable Reverse-Osmosis Applications.* ACS Applied Materials & Interfaces, 2013. **5**(23): p. 12510-12519.
76. Persson, K.M., V. Gekas, and G. Trägårdh, *Study of membrane compaction and its influence on ultrafiltration water permeability.* Journal of Membrane Science, 1995. **100**(2): p. 155-162.
77. Joung-Eun, G., et al., *Molecular Layer-by-Layer Assembled Thin-Film Composite Membranes for Water Desalination.* Advanced Materials, 2013. **25**(34): p. 4778-4782.
78. Choi, W., et al., *Tailor-Made Polyamide Membranes for Water Desalination.* ACS Nano, 2015. **9**(1): p. 345-355.
79. Vatanpour, V., et al., *A thin film nanocomposite reverse osmosis membrane containing amine-functionalized carbon nanotubes.* Separation and Purification Technology, 2017. **184**: p. 135-143.

80. Lee, T.H., et al., *Highly porous carbon nanotube/polysulfone nanocomposite supports for high-flux polyamide reverse osmosis membranes.* Journal of Membrane Science, 2017. **539**: p. 441-450.
81. Farahbakhsh, J., M. Delnavaz, and V. Vatanpour, *Investigation of raw and oxidized multiwalled carbon nanotubes in fabrication of reverse osmosis polyamide membranes for improvement in desalination and antifouling properties.* Desalination, 2017. **410**: p. 1-9.
82. Wan Azelee, I., et al., *Enhanced desalination of polyamide thin film nanocomposite incorporated with acid treated multiwalled carbon nanotube-titania nanotube hybrid.* Desalination, 2017. **409**: p. 163-170.
83. Kim, S., et al., *Non-swelling graphene oxide-polymer nanocomposite membrane for reverse osmosis desalination.* Journal of Membrane Science, 2018. **562**: p. 47-55.
84. Asadollahi, M., D. Bastani, and S.A. Musavi, *Enhancement of surface properties and performance of reverse osmosis membranes after surface modification: A review.* Desalination, 2017. **420**: p. 330-383.
85. Chem, L., *LG SW 400.* 2017.
86. Yang, Z., H. Guo, and C.Y. Tang, *The upper bound of thin-film composite (TFC) polyamide membranes for desalination.* Journal of Membrane Science, 2019. **590**: p. 117297.
87. Geise, G.M., et al., *Water permeability and water/salt selectivity tradeoff in polymers for desalination.* Journal of Membrane Science, 2011. **369**(1): p. 130-138.

초록

나노카본 소재를 활용한 역삼투막

이 곤 주

기계항공공학과

서울대학교

담수 자원은 인류가 생존하는 데 필수적인 자원이자 전세계 경제가 발전하는 데의 중요한 기둥이다. 그러나 인구가 증가하고 경제가 발전하며 기후 변화가 심해지면서 청결한 수자원이 부족하다는 위기가 세계적인 문제로 떠올리고 있다.

최근 몇 년간에 역삼투 (RO) 는 중요한 수처리 기술로 발전하면서 비전통적인 수원을 정화함으로써 청결한 담수의 공급을 증가할 수 있다는 길이 열리게 되었다. 지난 몇 십년 동안 역삼투 막의 유수량과 용질거절율이 계속 높아지기는 했지만 많은 에너지가 소모된다거나 오염되기 쉽다거나 하는 단점이 여전히 해결되지 못한 상태이다. 따라서 투수율을 높이고 에너지 소모를 줄이고 막의 구조와 안정성을 개선하여 오염 방지 능력을 제고한다는 등 면에서 더욱 많이 발전과 업그레이드가 필요하다고 생각한다. 본 연구는 지지층의 구조와 막 표면의 화학적인 성질을 개선하고 최적화함으로써 지지층이 폴리아미드 (PA) 활성층의

선택성과 투수량에 얼마나 많은 영향을 미치는지에 대해 연구하는 것을 목적으로 하였다.

(1) 지지층 표면의 화학적 성질과 기공크기, 다공성은 계면중합을 통해 형성된 활성층의 두께와 거칠기, 다리걸침구조에 영향을 미칠 수 있고 더 나아가 역삼투 막의 투수율과 제거율, 오염방지능성 등 막의 전체 성능에 영향을 미친다는 것은 주지의 사실이다. 높은 다공성을 가지는 지지층이 투수율을 높일 수 있지만 제거율은 떨어진다. 또한 좋은 친수성을 가지는 지지층은 투수율을 떨어트릴 수도 있다. 본 연구는 큰 구멍을 가지는 지지층 표면에 산화그래핀 레이어를 연결함으로써 수상 중의 MPD 분자가 유기상으로 확산하는 것을 제어하고 지지층의 표면 친수성을 개선하여 비교적 매끄러운 PA 층과 높은 투수율을 가지는 RO 막을 형성하도록 하였다. 그 결과로, GO 가 작을수록 RO 막의 투수율이 높다는 것을 확인하였다. 또한 작은 GO 를 사용하는 경우, 산화그래핀의 크기와 비슷한 구멍을 가지는 마이크로 필터 지지층을 이용해야만 가장 높은 제거율과 투수율을 확보할 수 있다는 것도 발견하였다.

(2) 매우 높은 투수율을 가지는 수직 정렬된 탄소 나노튜브 멤브레인 (VACNT) 은 매우 높은 다공성과 소수성을 가지기 때문에 새로운 RO 막의 지지층으로 사용될 수 있을 것이다. 역삼투 막을 합성할 때, 우리는 VACNT 를 지지층으로 사용하여 계면종합을 통해 폴리아미드 (PA) 활성층을 VACNT 지지층 위에 제자리 합성하도록

하였다. 이러한 RO 막이 15.5bar 에서는 128.6LMH 의 투수량과 98.3%의 제거율을 가지는 실험 결과를 확인하였다.

주요어: 산화 그래핀, 미세 여과 지지층, 중간층, 수직 정렬된 탄소 나노 튜브, 담수화, 역삼투막, 폴리아미드, 계면 중합, CNT 지지층

학 번: 2011-22879